

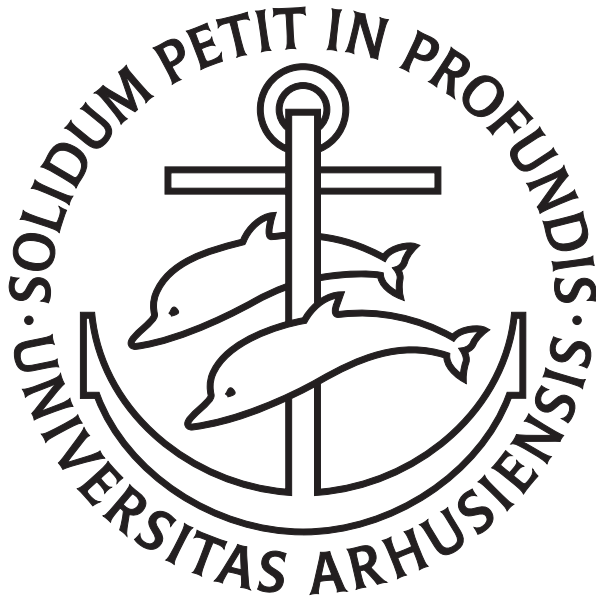
---

# Three-Body Recombination in Cold Atomic Gases

---

Peder Klokmose Sørensen

Department of Physics and Astronomy  
Aarhus University, Denmark



Dissertation for the degree of  
Doctor of Philosophy

July 2013

Copyright © 2013 Peder Klokmose Sørensen  
Department of Physics and Astronomy  
Aarhus University  
Ny Munkegade, building 1520  
DK-8000 Aarhus C  
Denmark  
1st edition, July 2013.

Typesetting done using L<sup>A</sup>T<sub>E</sub>X, BibTeX and the memoir class.

Figures made with gnuplot 4.6 and TikZ/PGF.

Printed by SUN-Tryk, Aarhus University.



This thesis is licensed under a  
[Creative Commons Attribution-Non Commercial-No Derivs 3.0 Unported License](https://creativecommons.org/licenses/by-nc-nd/3.0/).

This dissertation has been submitted to the Faculty of Science and Technology at Aarhus University, Denmark, in fulfillment of the requirements for the PhD degree in physics. The work presented has been performed under the supervision of Dmitri V. Fedorov and Aksel S. Jensen in the period of August 2009 to July 2013.

E13:

```
Fbzz snapl naq vagryyvtrag pvgngvba ol n snzbhf crefba.  
gur_snbhf_crefba (n_lrne)
```



# Contents

<b>Resume / Resumé</b>	<b>v</b>
English	v
Dansk	v
<b>Acknowledgements</b>	<b>vii</b>
<b>List of publications</b>	<b>ix</b>
<b>1 Introduction</b>	<b>1</b>
1.1 Few-body physics and the Efimov effect	1
1.2 Cold atoms and recombination	1
1.3 The Efimov effect as indirect observation	2
1.4 Feshbach resonances	3
1.5 Methods of describing three-body physics	4
1.6 Three-body parameter	5
1.7 Thesis outline	5
<b>2 Theory and Methods</b>	<b>7</b>
2.1 Two-body physics	7
2.1.1 Two-body scattering	7
2.1.2 Effective range expansion	10
2.1.3 The zero-range model	11
2.1.4 Feshbach resonances	11
2.1.5 The two-channel model	13
2.2 Three-body physics	16
2.2.1 Hyper-spherical coordinates	17
2.2.2 The zero-range model, hyper-spherical edition	20
2.2.3 Efimov and Thomas effects	24
2.2.4 The two-channel model, hyper-spherical edition	26
2.2.5 Effective range expansion, hyper-spherical edition	28

2.3	Three-body recombination rate . . . . .	30
2.3.1	Hidden crossing theory . . . . .	31
<b>3</b>	<b>Finite range effects</b>	<b>37</b>
3.1	Model Comparison . . . . .	38
3.2	Bound trimers . . . . .	40
3.2.1	Threshold for trimer creation . . . . .	41
3.3	Finite-range effects in the recombination rate . . . . .	44
3.4	Comparison to experiment . . . . .	45
3.5	Conclusions . . . . .	48
<b>4</b>	<b>Universal Three-Body Parameter</b>	<b>51</b>
4.1	Trimer threshold value revisited . . . . .	52
4.2	Two-body potentials . . . . .	54
4.2.1	Relating two- and three-body cut-offs . . . . .	56
4.2.2	Relating $a^{(-)}$ to $r_{\text{vdW}}$ . . . . .	57
4.3	Number of dimer bound states . . . . .	59
4.4	Conclusions . . . . .	61
<b>5</b>	<b>Recombination for negative scattering lengths</b>	<b>63</b>
5.1	The optical model . . . . .	64
5.2	The recombination coefficient . . . . .	65
5.2.1	Temperature effects . . . . .	67
5.3	Comparison to experimental data . . . . .	69
5.4	Conclusions . . . . .	70
<b>6</b>	<b>Mass-imbalanced systems</b>	<b>71</b>
6.1	The mass-imbalanced eigenvalue equation . . . . .	71
6.1.1	Properties of the mass-imbalanced potentials . . . . .	72
6.2	Results . . . . .	75
6.3	Conclusions . . . . .	76
<b>7</b>	<b>Summary and Outlook</b>	<b>79</b>
<b>A</b>	<b>Efficiently solving the eigenvalue equations</b>	<b>83</b>
<b>B</b>	<b>Low-energy limit of recombination probability</b>	<b>85</b>
	<b>Bibliography</b>	<b>89</b>

# Resume / Resumé

## English

Systems of three particles show a surprising feature in their bound state spectrum: a series of geometrically scaled states, known as Efimov states. These states have not yet been observed directly, but many recent experiments show indirect evidence of their existence via the so-called recombination process. The theories that predict the Efimov states also predicts either resonant enhancement of the recombination process or suppression by destructive interference, depending on the sign of the interaction between the particles. The theories predict universal features for the Efimov states, for instance that the geometric scaling factor is 22.7, meaning that one state is 22.7 times larger than its lower lying neighbour state. This thesis seeks to investigate non-universal effects by incorporating additional information about the physical interactions into the universal theories.

## Dansk

Systemer af tre partikler viser en overraskende effekt i spektret for bundne tilstande: en række geometrisk skalerede tilstande, kaldet Efimov tilstande. Disse tilstande er endnu ikke blevet observeret direkte, men mange nyere eksperimenter viser indirekte evidens for deres eksistens gennem den såkaldte rekombinationsproces. Teorierne der forudsiger Efimov tilstandene, forudsiger også enten resonant forstærkning af rekombinationsprocessen eller undertrykkelse pga. destruktiv interferens, afhængig af fortegnet på vekselvirkningen mellem partiklerne. Teorierne forudsiger en række universelle kendetegn, for eksempel at den geometriske skalafaktor har værdien 22.7, hvilket betyder at en given tilstand er 22.7 gange større end dens lavest liggende naboltilstand. Denne afhandling undersøger ikke-universelle effekter ved at inkorporere yderligere information om de fysiske vekselvirkninger.



# Acknowledgements

*"I would like to thank the Academy.... Wait.... What...?  
Oh... wrong speech. Let me start over."*

---

I would first and foremost like to thank my supervisors Dmitri Fedorov and Aksel Jensen for all the help, support, guidance and advice they have provided me with during the past four years. Their insight in everything from the physical understanding of interesting problems to practical computer implementations over written and verbal presentations to publishing in the academic community and a multitude of order major and minor things, has proven invaluable to my studies as a PhD student at Aarhus University.

I also very much enjoyed working with Nikolaj Zinner with whom I had the privilege of sharing an office for some time. This has resulted in some great papers that would probably not have come about without his contributions.

The rest of the sub-atomics group: Karsten Riisager, Hans Fynbo, Kasper Lind, Gunvor Koldste, Oleksandr Marchukov, Artem Volosniev and Jakob Pedersen also deserve honourable mention. Many a lunch break has been filled out by interesting discussion topics covering most aspects of life both inside and outside the yellow walls.

A special thank you goes to Artem Volosniev for reading through the manuscript of this thesis and pointing out all the weird things, minor mistakes and genuine errors all over the place.

Finally a thank you to my girlfriend Frederikke who has also read through the manuscript but more importantly helped me keep my spirits high when it all seemed pointless.



# List of publications

- [Sørensen 2011] P.K. Sørensen, D.V. Fedorov and A.S. Jensen. *Three-Body System with Two-Channel Zero-Range Interaction Model of Feshbach Resonance*. Few-Body Systems, vol. 50, no. 1-4, [pages 417–421](#), 2011. Refereed proceedings for the 21st European Conference on Few-Body Problems in Physics, Salamanca, Spain, 30 August–3 September 2010.
- [Sørensen 2012] P. K. Sørensen, D. V. Fedorov, A. S. Jensen and N. T. Zinner. *Efimov physics and the three-body parameter within a two-channel framework*. Phys. Rev. A, vol. 86, [page 052516](#), Nov 2012.
- [Sørensen 2013a] P. K. Sørensen, D. V. Fedorov and A. S. Jensen. *Three-Body Recombination Rates Near a Feshbach Resonance within a Two-Channel Contact Interaction Model*. Few-Body Systems, vol. 54, no. 5-6, [pages 579–590](#), 2013.
- [Sørensen 2013b] P. K. Sørensen, D. V. Fedorov and A. S. Jensen. *Three-Body Recombination with Two-Channel Contact Interactions*. Few-Body Systems, vol. 54, no. 5-6, [pages 591–595](#), 2013. Refereed proceedings for the Sixth Workshop on the Critical Stability of Quantum Few-Body Systems, Erice, Sicily, October 2011.
- [Sørensen 2013c] P. K. Sørensen, D. V. Fedorov, A. S. Jensen and N. T. Zinner. *Finite-range effects in energies and recombination rates of three identical bosons*. Journal of Physics B: Atomic, Molecular and Optical Physics, vol. 46, no. 7, [page 075301](#), 2013.
- [Sørensen 2013d] P. K. Sørensen, D. V. Fedorov, A. S. Jensen and N. T. Zinner. *Three-body recombination at finite energy within an optical model*. [arXiv:1307.2854](#), July 2013. *Under review*.



# Chapter 1

## Introduction

### 1.1 Few-body physics and the Efimov effect

The quantum mechanical three-body problem has been investigated heavily since the birth of quantum mechanics. As with the classical counterpart there are no general analytical solutions to the problem. Many features of the system of three interacting bodies are known nonetheless. For instance, given a system of three identical interacting particles where any subsystem of two particles supports a bound state with infinite scattering length, the total system has a spectrum of infinitely many bound states with a characteristic scaling relation between successive states. The size of a state is a factor of 22.7 times larger than the previous state and the energy is a factor  $22.7^2 = 515$  times smaller.

This is known as the Efimov effect which was predicted in 1970 [Efimov 1971] but remained unobserved for many years. The first attempts to discover the effect was in nuclear physics, however, without success [Jensen 2004]. It was in the realm of atomic physics that the first observation was made in 2006 using a gas of cold Cs atoms [Kraemer 2006, Ferlaino 2010].

### 1.2 Cold atoms and recombination

Cold atoms as a research area has exploded in the past two decades. The experimental realization of Bose Einstein Condensates (BEC's), a macroscopic collective of thousands, up to millions [van der Stam 2007] of atoms at  $\mu K$  to nK temperatures, has sparked a revolution in cold gas physics. An essential experimental tool for this progress is that of Feshbach resonances [Chin 2010], without which cold atomic gas experiments would probably be quite different today.

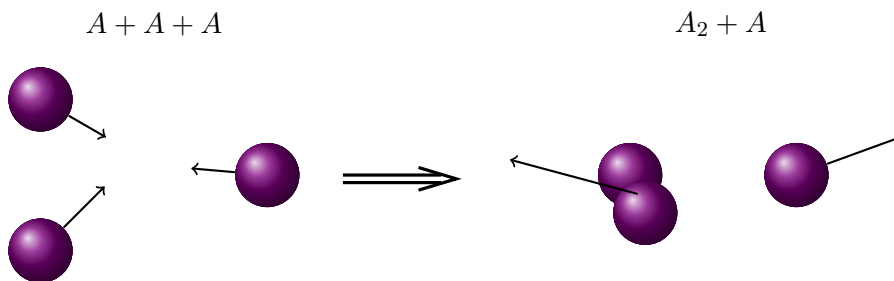


Figure 1.1: It's all about recombination.

Three-body states are an important part of cold gas atomic physics because the gases consist of interacting particles. Collisions can lead to loss of particles via the process known as recombination, illustrated in Figure 1.1. Three particles,  $A + A + A$ , may interact in such a way that two of them form a bound state, known as a dimer,  $A_2$ , while the third atom,  $A$ , carries away excess energy and momentum. The products will have an increased kinetic energy due to the increased binding energy in the dimer. The result is that all three atoms are lost from the trap since it is typically too shallow to withhold the energetic products. Thus particles are lost from the trap leading to a finite lifetime of such experimental set-ups [Esry 1999, Nielsen 1999, Braaten 2001].

### 1.3 The Efimov effect as indirect observation

Recombination leads to a loss rate of the form  $\dot{n} = -\alpha_{\text{rec}}n^3$  where  $n$  is the number density of the particles, the dot denotes the temporal derivative and  $\alpha_{\text{rec}}$  is known as the recombination coefficient. The power 3 is due to the number of triplets in a gas of  $N$  atoms scaling as  $N^3$  for large  $N$ . The Efimov effect is observed as a characteristic series of peaks and troughs in the recombination coefficient as a function of the scattering length, see for instance Figures 3.8 to 3.11 for positive scattering length and Figure 5.3 for negative scattering length. This is caused by the existence of the before mentioned Efimov states.

Similar processes can occur for four, five, six, ... particles. However, such recombination events are progressively less likely to occur since more particles are required to be in the same small volume of space. Correspondingly, a much higher density of particles is expected to be required in order to see these higher order effects, which is not the case for current experiments.

## 1.4 Feshbach resonances

The interaction strength between atoms in cold gases is usually described by the scattering length  $a$ , which is the lowest order measure of the strength of the interaction potential. Using only the scattering length is mostly sufficient when dealing with low-energy  $s$ -wave scattering. For a given atomic system the scattering length is fixed by nature. However, an experimental tool exists that allows experimentalists to tune the scattering length to practically any desired value. This tool is known as a Feshbach resonance. It utilises that the difference in magnetic momenta in two different reaction channels makes it possible to tune the energy difference between these channels by applying an external magnetic field to the system. If the energy of the interacting particles is close to the energy of a bound state in the upper of the interaction channels a resonant behaviour is seen where the scattering length diverges. In principle any desired value of the scattering length can be obtained, both positive and negative, by tuning the magnetic field,

From dimensional analysis one can easily show that the recombination coefficient,  $\alpha_{\text{rec}}$ , goes roughly as  $a^4$ , however, with some modifications depending on the sign of  $a$ . Hence the form  $\alpha_{\text{rec}} = C(a)a^4$  where  $C(a)$  is a log-periodic function of  $a$ . For three identical particles the function  $C(a)$  obeys  $C(22.7a) = C(a)$ . A fundamental conclusion of this thesis is that the factor 22.7 changes when the effective range is included.

The sign of the scattering length  $a$  indicates whether a given two-body system is governed by attractive or repulsive interactions and hence whether the system supports a so-called shallow dimer. A shallow dimer is characterized by the binding energy of the order  $a^{-2}$ . This is the case when  $a$  is positive. As mentioned in the first paragraph, when a two-body subsystem of three particles supports a dimer at zero energy, i.e.  $a = \infty$ , the Efimov effect occurs. This is seen in the recombination coefficient as a characteristic series of troughs in the spectrum at certain values of the scattering length,  $a$ . The ratio of the  $a$ -values of these troughs is precisely the Efimov scaling factor 22.7. The existence of troughs in the spectrum, i.e. a lowering of the recombination rate as a function of the scattering length, is due to the existence of the trimer system and hence a reduced probability to recombine into the dimer plus free particle state.

For negative  $a$ , a similar tendency is observed, however, with peaks instead of troughs in the spectrum. This suggests that the mechanics for recombination is quite different for the case of positive scattering length. Indeed there are no shallow dimers for negative  $a$  so recombination goes into a deeply bound dimer and a free particle. The origin of the peaks is also quite different. In the

interaction potential for three particles with negative scattering length there is a centrifugal barrier that the three-body wave function must tunnel through (there is no such barrier for positive scattering lengths). The barrier height and location depend on the scattering length. When the scattering length is tuned such that the energy of the incoming wave function matches with the energy of a resonance behind the barrier, recombination is strongly increased.

## 1.5 Methods of describing three-body physics

Real inter-atomic potentials are quite complicated if all details are included. Therefore it is desirable to use simplified models that nevertheless carry some of the same properties as the full potential. In low-energy physics the scattering length mentioned above is exactly one such property. Two potentials with the same scattering length would yield the same results, to leading order, for scattering observables, provided that the scattering energy is small (on some appropriate scale). Therefore choosing the simpler potential is beneficial.

The simplest potential possible is, in some sense, the  $\delta$ -function potential, also known as the zero-range or contact potential. The zero-range function potential has the scattering length as the single parameter. It has been proven to be a quite accurate tool for describing low-energy three-body physics. Furthermore, models based on zero-range potentials provide reasonably easy and straightforward numerical calculations without too many complications and with fast computational run-times. They also allow for clear and intuitive understanding of the physical processes.

However, it is desirable to get a feeling for higher order effects, that is, take into account not only the scattering length but higher order parameters as well. The next order succeeding the scattering length is known as the effective range. A physical potential in cold atomic gasses has some length scale outside of which the potential is practically 0, this can be quantified as the range of the potential. While the scattering length generally is not related to the physical range of the potential, but can span many orders of magnitude in both positive and negative directions, the effective range is a much better measure for the physical range of the potential.

Inclusion of the effective range can be done by choosing a finite range potential instead of the above mentioned zero-range potential. However, this adds quite a bit of complexity to the calculations. Retaining the computational simplicity of the zero-range potentials is thus be desirable. This can in fact be done by using the so-called coupled channels approach. By describing the interaction, not with a single zero-range potential, but as a system of two

coupled components with two zero-range potentials, an effective range can be extracted. This still rather simple set-up allows range effects to be investigated while retaining computational simplicity and interpretative elegance.

## 1.6 Three-body parameter

A problem with pure zero-range potentials is that the bound state spectrum does not have a lower bound. The Efimov effect equally well allows downscaling with 22.7, making the bound system smaller while increasing the energy. This can be done indefinitely, yielding tighter and tighter bound systems. This is called the Thomas effect [Thomas 1935] and is caused by a breakdown in the assumption of using contact potentials for the interactions.

A way of avoiding the Thomas effect is to artificially introduce a short range length scale that acts as a regularization and sets a lower bound for the bound state energies [Fedorov 2001b]. This parameter is known as the three-body parameter and was long thought to be related to the short-range details of the atomic potentials and as such expected to differ greatly from one system to another. In recent years it has come to attention that the three-body parameter, when divided by the van der Waals length, a length scale related to the long-range behaviour of neutral atom potentials, has a seemingly universal value of  $\sim 9.8$  for several different atomic species. This curiosity has led to a lot of theoretical activity trying to explain this phenomena [Chin 2011, Naidon 2012a, Wang 2012, Schmidt 2012].

## 1.7 Thesis outline

### *Chapter 1*

This current introductory chapter that you are now reading and have completed by about 79.9%.

### *Chapter 2*

Here most of the theoretical and numerical groundwork is laid out. Low energy scattering theory is shortly revised and the most fundamental quantities for this thesis, the scattering length,  $a$ , and the effective range,  $R$ , are defined. Then the hyper-spherical coordinates are introduced as a scheme for practically and succinctly describing systems of three particles. The zero-range models are then introduced and woven into the hyper-spherical formalism. Methods for calculating recombination rates and bound state energies for three-body systems are then discussed. This involves going into the complex plane and returning on a different level than what you started out on,

having in the meantime passed around a hidden crossing. This does not work for negative scattering lengths, so instead the differential equation is solved directly, however, again with the aid of complex ~~wonders~~ numbers.

#### *Chapter 3*

Here we present some effects of the effective range. In the trimer bound state spectrum it is seen how the three-body parameter depends on the effective range. This holds also for the bound state energies on resonance. Recombination for positive scattering length also shows clear dependency of the effective range. Calculations are compared to the experimental evidence, unfortunately the presently available experimental data exists only for systems of broad resonances where the effective range is small. The range effect are thus not easily observed in these systems. It is shown that the effects of the effective range show up in a non-trivial manner in the recombination coefficient.

#### *Chapter 4*

The apparent universality of the three-body parameter, when given in units of the van der Waals length, is given yet another possible explanation. This is done by the relating three-body quantities, i.e. the three-body parameter as a function of the regularization cut-off, to appropriate two-body equivalents. We then look at how these parameters relate to typical two-body potentials and the number of bound states in these. We find reasonably good agreement between the model and available experimental data.

#### *Chapter 5*

In this chapter we revisit the three-body recombination rate but for negative scattering lengths. The method outlined in chapter 2 is not applicable in this case and instead we turn to the radial differential equation directly. By superposing the potential with an optical potential, i.e. a potential that has a complex value, we obtain a recombination coefficient that models experimental data quite well, given its simplicity. We furthermore include the effects of finite temperature in the experimental system.

#### *Chapter 6*

Here some, as of this writing still unpublished, results for mass-imbalanced systems are presented. Systems of mixed species of atoms may provide a key insight into Efimov physics since the main feature, namely the geometric scaling of states, persists in these systems. We show that the frequency of resonance peaks or troughs is increased. This could allow for better and more accurate determination of the scaling factor and therefore allow for better testing of predictions involving the effective range.

#### *Chapter 7*

Finally we provide a summary and look ahead to possible future projects.

## Chapter 2

# Theory and Methods

*The theoretical groundwork is laid out and the different models and methods that will be used in this thesis are described.*

---

In this chapter the theoretical models and methods that are used in this thesis will be introduced. Initially the basic two-body scattering concepts are described and terminology is defined. Still in the two-body regime the ubiquitous zero-range model is presented along with some extension models known as the two-channel model and the effective range expansion model. The experimentally important tool of Feshbach resonances is introduced and related to these models. Then we go into the three-body sector where the formalism just described for the two-body physics is stated in the three-body formalism. Some important three-body results, like the Efimov effect and three-body recombination rates, are discussed and related to the experimental observables. Finally the numerical methods, implemented on top of these models, are presented.

### 2.1 Two-body physics

#### 2.1.1 Two-body scattering

The problem is to predict the outcome of colliding two particles. Given an initial state of particles, their energy and momentum, the aim is to calculate the energy- and momentum distribution of the products. This is a well-established discipline in both classical and quantum mechanics.

The system of two particles with coordinates  $\mathbf{r}_1$  and  $\mathbf{r}_2$  and masses  $m_1$

and  $m_2$  is described by the Schrödinger equation

$$\left[ \frac{-\hbar^2}{2m_1} \nabla_1^2 + \frac{-\hbar^2}{2m_2} \nabla_2^2 + V(\mathbf{r}_1, \mathbf{r}_2) \right] \Psi(\mathbf{r}_1, \mathbf{r}_2) = E\Psi(\mathbf{r}_1, \mathbf{r}_2), \quad (2.1)$$

where  $V(r_1, r_2)$  is the interparticle interaction. We will assume that no external forces act on the system.

If a potential depends on the distance between particles,  $r = |\mathbf{r}|$ , only, where  $\mathbf{r} = \mathbf{r}_1 - \mathbf{r}_2$ , the center of mass motion is easily separated out by introducing the center-of-mass coordinate  $\mathbf{R} = \frac{m_1\mathbf{r}_1 + m_2\mathbf{r}_2}{m_1 + m_2}$ . For spherical potentials the angular part of the wave function is given by the spherical harmonics  $Y_l^m(\theta, \phi)$  [Griffiths 2005] (the superscript  $m$  is the magnetic quantum number, not to be confused with any mass). This leaves us with the relative radial wave function  $\psi(r)$  described by

$$\left[ \frac{-\hbar^2}{2m} \frac{d^2}{dr^2} + \left( V(r) + \frac{\hbar^2 l(l+1)}{2mr^2} \right) \right] \psi(r) = E\psi(r), \quad (2.2)$$

where  $l$  is the angular momentum eigenvalue from the angular equation that leads to the spherical harmonics and  $m = \frac{m_1 m_2}{m_1 + m_2}$  is the reduced mass. The full radial wave function is  $\psi(r)/r$ .  $E$  is now the energy of the relative motion since the center-of-mass motion has been separated out.

Before we go on to the scattering, some simplifying assumptions are in order. The cold atomic gases, that constitute the physical system under observation, are at very low temperature, and hence the particles have low kinetic energy. This leads to two important simplifications. First, since the centrifugal barrier will suppress contributions from anything higher than  $s$ -waves, only  $s$ -waves need to be considered and we can put  $l = 0$ , simplifying eq. (2.2) quite a bit. Second, and perhaps most important, the use of  $s$ -waves only, allows us to choose the potential  $V(r)$  almost as we wish, provided some simple quantities are retained. Physical inter-particle potentials are quite complicated if all details are included. If we could somehow choose simpler potentials with some of the same merits the analytical and numerical results might be easier to obtain.

A very practical result from elementary scattering theory is the first Born-approximation expression for the scattering amplitude  $f^{(1)}(\theta)$  at low incoming energy [Sakurai 1994]

$$f^{(1)}(\theta) = -\frac{1}{4\pi} \frac{2m}{\hbar^2} \int V(r) d^3\mathbf{x}. \quad (2.3)$$

This is essentially the 3D Fourier transform of the potential in the limit of the energy going to zero, the superscript 1 indicates that this is a first order approximation. The scattering amplitude  $f^{(1)}(\theta)$  is a measure of how much of the incoming wave gets deflected an angle  $\theta$  from the original trajectory through the differential cross section  $d\sigma/d\Omega = |f^{(1)}(\theta)|^2$ . In the present limit of small energies the integral is independent of  $\theta$  and the incoming wave gets scattered equally in all directions. The loss of particles from the initial beam is neatly summarized in the total cross section  $\sigma$  as the integral over the unit sphere of the differential cross section. It is often written as

$$\sigma = \int \frac{d\sigma}{d\Omega} d\Omega = 4\pi a^2, \quad (2.4)$$

where  $a$  is known as the scattering length<sup>1</sup>, in this case we have simply  $a = |f^{(1)}(\theta)|$ . The scattering length is a lowest order measure of the strength of the potential. Two potentials with the same scattering length will scatter an incoming wave equally in the low-energy limit. Thus given a complicated potential (either with a cumbersome analytical expression or perhaps only known phenomenologically) it can be replaced by a simpler potential with the same scattering length if only low energy is considered.

The physical reasoning behind these results is that at low energy the wave length of the wave function is very large, larger even than the spatial extent of the potential. Small details of the potential thus cannot be probed by the wave function and only the overall cumulative effects are measured.

If we can measure the scattering length of a physical potential it will suffice to use a simpler potential with the same scattering length in calculations. Any result must agree, to leading order, with similar but much more complicated calculations using the full potential.

A short geometrical interpretation is in order which will also reveal an important feature of the scattering length. Assume that the potential is zero outside some finite range  $r_0$  and that the energy,  $E$ , is positive such that the wave function for  $r > r_0$  takes the free form

$$\psi(r) = C \sin(kr + \delta(k)), \quad \text{for } r > r_0, \quad (2.5)$$

where  $\delta(k)$  is the energy dependent phase shift and the wave number  $k$  is defined by  $k^2 = 2mE/\hbar^2$ . The phase shift depends on the short-range details of the potential.

---

<sup>1</sup>In the case of distinguishable particles, for identical bosons an additional factor 2 is needed while for identical fermions the total cross section vanished in this limit.

In the limit of very low energy, essentially  $E = 0$ , the solution to eq. (2.2) is a simple linear function which can be obtained from eq. (2.5) by

$$\psi(r) \stackrel{k \rightarrow 0}{\approx} C(\sin \delta + kr \cos \delta) = K \left(1 - \frac{r}{a}\right). \quad (2.6)$$

Here the scattering length enters in the form

$$\lim_{k \rightarrow 0} k \cot \delta(k) = -\frac{1}{a}. \quad (2.7)$$

The low-energy limit of eq. (2.5) is shown in Figure 2.1 for the finite square well, for which an analytical solution is readily available [Thøgersen 2009]. The left potential is deep enough that the zero-energy scattering wave function intersects the positive  $x$ -axis. This is equivalent to the potential being able to support a bound state [Sakurai 1994]. The right potential is too shallow to support a bound state. Correspondingly the zero energy wave function does not intersect the  $x$ -axis at a positive value. The linear extrapolation of the asymptotic wave function, however, intersects the negative  $x$ -axis at the, now negative, scattering length.

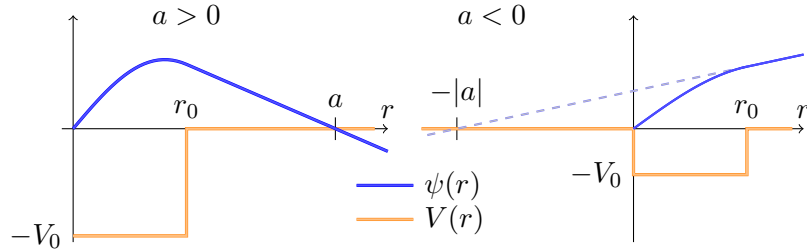


Figure 2.1: The zero energy solution to the Schrödinger equation for the finite square well. The left well is deep enough to support a bound state and has a positive scattering length whereas the right potential is too shallow and has a negative scattering length.

Increasing the potential depth  $V_0$  from the right scenario to the left must yield a critical value for which the scattering length will diverge to  $\pm\infty$ . At precisely this value the potential is deep enough to support yet another bound state with energy zero.

### 2.1.2 Effective range expansion

Equation (2.7) looks quite like a Taylor expansion of  $k \cot \delta(k)$  around  $k = 0$ . Thus it seems natural to include another term in the expansion

$$k \cot \delta(k) = -\frac{1}{a} + \frac{1}{2}Rk^2. \quad (2.8)$$

Here  $R$  is known as the effective range. The value of the effective range is typically of the order of the actual physical range of the potential ( $r_0$  in Figure 2.1). Whereas the scattering length,  $a$ , can vary between  $\pm\infty$ , the effective range,  $R$ , will vary much less.

### 2.1.3 The zero-range model

The derivation of eq. (2.7) from eq. (2.5) can for the zero-range interaction (where essentially  $r_0 = 0$  and eq. (2.5) is valid everywhere) be formulated as [Fedorov 2001b]

$$\frac{1}{\psi} \frac{d\psi}{dr} \Big|_{r=0} = k \cot \delta(k) \stackrel{k \rightarrow 0}{=} -\frac{1}{a}. \quad (2.9)$$

Assume that  $V(r) = 0$  everywhere except the origin. Then the wave function is  $\psi = \sin(kr + \delta(k))$ . Imposing the boundary condition eq. (2.9) yields

$$\frac{1}{\sin(kr + \delta(k))} k \cos(kr + \delta(k)) \Big|_{r=0} = k \cot \delta(k). \quad (2.10)$$

Correspondingly, a bound state is given by  $\psi(r) = \exp(-\kappa r)$  (disregarding normalization) yielding

$$\frac{1}{\exp(-\kappa r)} (-\kappa) \exp(-\kappa r) = -\kappa = -\frac{1}{a}, \quad (2.11)$$

where  $\kappa^2 = -2mE/\hbar^2$ . Only for positive scattering lengths does a bound state exist, since  $\kappa$  is defined to be positive and the wave function has to be normalizable.

### 2.1.4 Feshbach resonances

The important experimental tool of Feshbach resonances lies at the heart of a lot of the cold atomic physics experiments since its discovery and realization in 1998 [Stenger 1998] in a gas of Sodium atoms. Having since been realized in almost all alkali atoms (Na [Stenger 1999], Li [Pollack 2009], K [Zaccanti 2009], Cs [Kraemer 2006]) its usefulness lies in the ability to tune the interaction strength simply by applying an external magnetic field.

Figure 2.2 shows a schematic set-up of a system with a Feshbach resonance. The interaction is described using two channels, the open channel where the potential value at large distances is smaller than the relative kinetic energy and the closed channel where the kinetic energy is lower than the asymptotic value of the potential. Both the open and closed channels may support a number

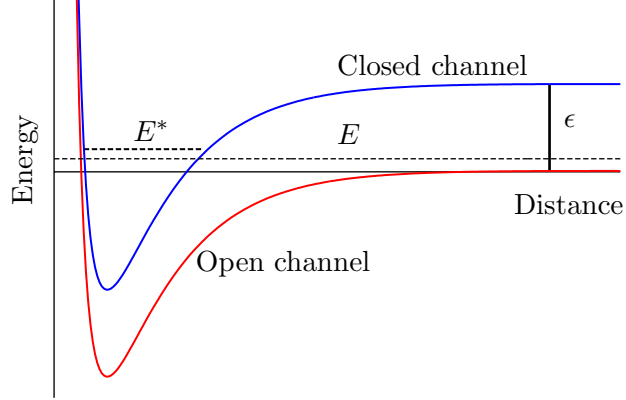


Figure 2.2: A schematic drawing of a system with a Feshbach resonance. The open and closed channels denote two different interaction channels for the system. When the relative kinetic energy,  $E$ , corresponds to the energy of a bound state in the closed channel,  $E^*$ , the scattering length is resonantly enhanced due to the degeneracy of the states. The Feshbach tuning is enabled using the Zeeman effect by changing the value of  $\epsilon$  and thus the value of  $E^*$ .

of bound states. If the closed channel happens to have a bound state at  $E^*$  that corresponds to the value of relative incoming kinetic energy,  $E$ , there is resonant coupling between the channels and the scattering cross section is greatly enhanced.

The bound state at  $E^*$  may not be near  $E$  due to the temperature at which the experiment is carried out. Changing the incoming energy  $E$  by changing the temperature may not be practical/possible. However, changing the energy levels  $E^*$  can be done simply by applying an external magnetic field. Due to the Zeeman effect an external magnetic field will change the energy levels of both the open and the closed channels. If the magnetic momenta in the open and closed channels differ, then the energy levels in the two channels will change relative to each other when the magnetic field strength is changed, thus changing the value of  $\epsilon$  and therefore also of  $E^*$  and finally  $a$ . A phenomenological expression for the scattering length as a function of an externally applied magnetic field of strength  $B$  is [Chin 2010]

$$a(B) = a_{\text{bg}} \left( 1 - \frac{\Delta B}{B - B_0} \right). \quad (2.12)$$

Here  $B_0$  is the field strength at which the scattering length diverges,  $\Delta B$  is

the width of the resonance and  $a_{\text{bg}}$  is the scattering length far from resonance. The effective range near a Feshbach resonance is given by [Thøgersen 2009]

$$R(a) = R_0 \left(1 - \frac{a_{\text{bg}}}{a}\right)^2, \quad (2.13)$$

where  $R_0$ , the effective range on resonance, is given by the width of the resonance [Bruun 2005]

$$R_0 = -\frac{2}{m\delta\mu a_{\text{bg}}\Delta B}, \quad (2.14)$$

where  $\delta\mu$  is the difference in magnetic momenta between the two channels.

### 2.1.5 The two-channel model

The scattering length is the sole parameter of the zero-range model. This section adds to this model and incorporates the effective range using another simple model. We build the model upon the two-channel set-up of Feshbach resonances. The two-component wave function is

$$\psi(r) = \begin{bmatrix} u_{\text{closed}}(r) \\ u_{\text{open}}(r) \end{bmatrix}, \quad (2.15)$$

where  $u_{\text{open}}$  describes the open channel, where both atoms are in their ground state, while the closed channel,  $u_{\text{closed}}$ , has one of the atoms in an excited state.

The Schrödinger equation for this system is

$$-\frac{\hbar^2}{2m}u_{\text{closed}}'' = (E - \epsilon)u_{\text{closed}}, \quad (2.16a)$$

$$-\frac{\hbar^2}{2m}u_{\text{open}}'' = Eu_{\text{open}}, \quad (2.16b)$$

where primes denote differentiation with respect to  $r$ ,  $m$  is the reduced mass of the two atoms,  $E$  is the relative energy and  $\epsilon$  is the excitation energy of the closed channel with respect to the open channel. The coupling between channels is obtained through the boundary condition eq. (2.9), that we generalize to a two-level system in the following way

$$\begin{bmatrix} u'_{\text{closed}} \\ u'_{\text{open}} \end{bmatrix}_{r=0} = \begin{bmatrix} -a_{\text{closed}}^{-1} & \beta \\ \beta & -a_{\text{open}}^{-1} \end{bmatrix} \begin{bmatrix} u_{\text{closed}} \\ u_{\text{open}} \end{bmatrix}_{r=0}, \quad (2.17)$$

where the constant  $\beta$  parametrizes the coupling between the channels, and  $a_{\text{open}}$  and  $a_{\text{closed}}$  are the respective scattering lengths in the two channels.

Assume that the energy is below the threshold for excitation,  $0 < E < \epsilon$ , then the solution to eqs. (2.16) is

$$u_{\text{closed}} = A_{\text{closed}} \exp(-\kappa_{\text{closed}} r) , \quad (2.18a)$$

$$u_{\text{open}} = A_{\text{open}} \sin(k_{\text{open}} r + \delta) , \quad (2.18b)$$

where  $A_{\text{closed}}$  and  $A_{\text{open}}$  are constants,  $k_{\text{open}} = \sqrt{2mE/\hbar^2}$  and  $\kappa_{\text{closed}} = \sqrt{2m(\epsilon - E)/\hbar^2}$ .

Inserting this solution into the boundary condition eq. (2.17) yields a system of linear equations for the constants  $A_{\text{closed}}$  and  $A_{\text{open}}$

$$\begin{bmatrix} -\beta \sin \delta & a_{\text{closed}}^{-1} - \kappa_{\text{closed}} \\ k_{\text{open}} \cos \delta + a_{\text{open}}^{-1} \sin \delta & -\beta \end{bmatrix} \begin{bmatrix} A_{\text{closed}} \\ A_{\text{open}} \end{bmatrix} = 0 . \quad (2.19)$$

This system of equations has a non-trivial solution only if the determinant of the  $2 \times 2$  matrix vanishes, yielding

$$\beta^2 \sin \delta - \left( k_{\text{open}} \cos \delta + \frac{\sin \delta}{a_{\text{open}}} \right) \left( \frac{1}{a_{\text{closed}}} - \kappa_{\text{closed}} \right) = 0 . \quad (2.20)$$

Isolating  $k_{\text{open}} \cot \delta$ , as in eq. (2.7) and eq. (2.8), gives

$$k_{\text{open}} \cot \delta = -\frac{1}{a_{\text{open}}} + \frac{\beta^2}{a_{\text{closed}}^{-1} - \kappa_{\text{closed}}} . \quad (2.21)$$

Taylor expansion of the right hand side around  $k_{\text{open}} = 0$  yields the effective scattering length,  $a$ , and effective range,  $R$ , of this two-level system

$$\frac{1}{a} = \frac{1}{a_{\text{open}}} + \frac{\beta^2}{\kappa - a_{\text{closed}}^{-1}} , \quad (2.22)$$

$$R = -\frac{\beta^2}{\kappa (\kappa - a_{\text{closed}}^{-1})^2} , \quad (2.23)$$

where  $\kappa^2 = 2m\epsilon/\hbar^2$ . The two-channel model can thus emulate a system with finite effective range yet it consists only of contact interactions. Note that the effective range in this model is always negative.

The effective range eq. (2.23) can be written in terms of the scattering length in the clearer way

$$R(a) = R_0 \left( 1 - \frac{a_{\text{open}}}{a} \right)^2 , \quad (2.24)$$

where

$$R_0 = \frac{-1}{\kappa_0 a_{\text{open}}^2 \beta^2}, \quad (2.25)$$

is the effective range on resonance,  $a = \infty$ , and where  $\kappa_0$  is the value of  $\kappa$  in eq. (2.22) that yields  $a = \infty$ . This agrees with eq. (2.13).

This simple two-level system will be used to investigate finite range effects without using finite range potentials, which are quite a bit more cumbersome to work with. The downside to this approach is that only negative effective ranges can be modelled. This, however, is not a problem as we will be looking at Feshbach systems at or near resonance where the effective range is always negative [Chin 2010].

### The two-channel model relation to Feshbach resonances

The effective scattering length of the two-channel model is fixed by the parameters of the two-level system, i.e. the scattering lengths in each sub-system,  $a_{\text{open}}$  and  $a_{\text{closed}}$ , and the coupling between them,  $\beta$ . To be able to tune the scattering length as desired the Zeeman effect is now added. An external magnetic field of strength  $B$  changes the energy splitting  $\epsilon$  of the two-level system by

$$\epsilon \rightarrow \epsilon - \delta\mu B, \quad (2.26)$$

where  $\delta\mu$  is the difference in magnetic moments of the atom in the ground and the excited state. The scattering length from eq. (2.22) is then a function of the magnetic field,

$$a(B) = a_{\text{open}} \frac{\kappa(B) - a_{\text{closed}}^{-1}}{\kappa(B) - a_{\text{closed}}^{-1} + \beta^2 a_{\text{open}}}, \quad (2.27)$$

where  $\kappa(B) = \sqrt{2m(\epsilon - \delta\mu B)/\hbar^2}$ . The scattering length diverges at the critical value of the magnetic field,  $B_0$ , given by

$$\kappa_0 \equiv \kappa(B_0) = \frac{1}{a_{\text{closed}}} - \beta^2 a_{\text{open}}, \quad (2.28)$$

which gives

$$B_0 = \frac{1}{\delta\mu} \left( \epsilon - \frac{\hbar^2 \kappa_0^2}{2m} \right). \quad (2.29)$$

Expanding  $a(B)$  in the vicinity of  $B_0$  gives precisely eq. (2.12) with  $a_{\text{bg}} = a_{\text{open}}$  and

$$\Delta B = \frac{1}{\delta\mu} \frac{\hbar^2 \kappa_0 \beta^2 a_{\text{open}}}{m}. \quad (2.30)$$

On resonance the effective range,  $R$ , is inversely proportional to the width of the resonance,  $\Delta B$ ,

$$R(B_0) = -\frac{1}{\kappa_0 \beta^2 a_{\text{open}}^2} = -\frac{1}{a_{\text{open}}} \frac{\hbar^2}{m \delta \mu \Delta B}, \quad (2.31)$$

as in eq. (2.14).

Given  $\Delta B$ ,  $B_0$  and the background scattering length  $a_{\text{bg}}$  from experiment, eq. (2.22), eq. (2.29) and eq. (2.30) can be solved for the model parameters  $a_{\text{open}}$ ,  $a_{\text{closed}}$  and  $\beta$

$$a_{\text{open}} = a_{\text{bg}}, \quad (2.32a)$$

$$a_{\text{closed}} = \frac{2 \cdot \text{sign}(\Delta B) \sqrt{\tilde{\epsilon}}}{\frac{\delta \mu \Delta B}{E_0} + 2\tilde{\epsilon}} a_{\text{open}}, \quad (2.32b)$$

$$\beta^2 = \frac{1}{2a_{\text{open}}^2} \frac{1}{\sqrt{\tilde{\epsilon}}} \frac{\delta \mu |\Delta B|}{E_0}, \quad (2.32c)$$

where

$$\tilde{\epsilon} = \frac{\epsilon - \delta \mu B_0}{E_0}, \quad E_0 = \frac{\hbar^2}{2m a_{\text{bg}}^2}. \quad (2.33)$$

The value of  $\epsilon$  cannot be determined uniquely from these equations. It can, however, be found by fitting eq. (2.27) to experimental data,  $a(B)$ , as shown in Figure 2.3. However, the value of  $\epsilon$  does not affect the final observables significantly, provided it is greater than  $\delta \mu B_0$  and is of the order the hyperfine splitting.

Figure 2.3 shows experimental data for a Feshbach resonance in  $^{23}\text{Na}$  along with fits from eq. (2.12) and eq. (2.22). The phenomenological expression eq. (2.12) gives  $B_0 = 907.0$  G,  $\Delta B = 0.71$  G, while the two-channel expression eq. (2.22) gives  $B_0 = 907.1$  G,  $\Delta B = 0.69$  G when using eq. (2.29) and eq. (2.30). Choosing  $\epsilon = 23 \mu\text{eV}$  provides a good fit. Varying  $\epsilon$  has relatively little influence on the values of  $B_0$  and  $\Delta B$  provided it is within this order of magnitude.

The phenomenological and the two-channel curves are virtually identical, so from now on the experimental parameters  $a_{\text{bg}}$ ,  $\Delta B$ ,  $B_0$  and  $\delta \mu$  are used to determine the parameters of the two-channel model through eqs. (2.32).

## 2.2 Three-body physics

The previously described models rely on two-body physics alone. Applying them to three-body systems requires a framework that efficiently takes into

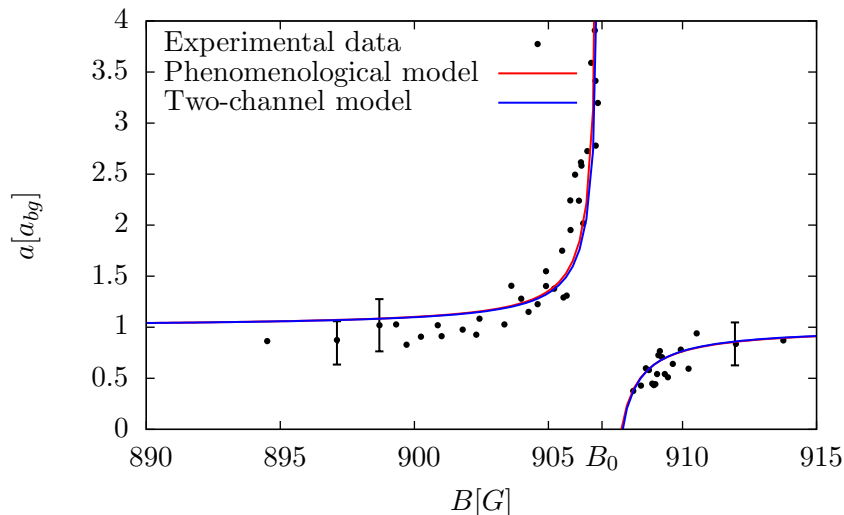


Figure 2.3: The scattering length,  $a$ , between two  $^{23}\text{Na}$  atoms as a function of the external magnetic field,  $B$ , with two-channel eq. (2.22) and empirical eq. (2.12) fits to the experimental data from [Stenger 1999]. The Feshbach resonance location is at  $B_0 = 907$  G with width  $\Delta B = 0.7$  G.

account the extra degrees of freedom without adding too much complexity such that the simple methods using contact interactions can still be applied.

### 2.2.1 Hyper-spherical coordinates

A set of three particles labelled by indices  $\{i, j, k\}$  can be described either by their absolute Cartesian coordinates  $\{\mathbf{r}_i, \mathbf{r}_j, \mathbf{r}_k\}$  or by a linear combination of these. One such combination is the Jacobi coordinates [Nielsen 2001]

$$\mathbf{x}_i = \sqrt{\mu_i}(\mathbf{r}_j - \mathbf{r}_k), \quad \mathbf{y}_i = \sqrt{\mu_{jk}} \left( \mathbf{r}_i - \frac{m_j \mathbf{r}_j + m_k \mathbf{r}_k}{m_j + m_k} \right), \quad (2.34)$$

$$\mu_i = \frac{1}{m} \frac{m_j m_k}{m_j + m_k}, \quad \mu_{jk} = \frac{1}{m} \frac{m_i (m_j + m_k)}{m_i + m_j + m_k}, \quad (2.35)$$

where  $m_{\{i,j,k\}}$  are the masses of particle  $\{i, j, k\}$ . Here  $\{i, j, k\}$  is a cyclic permutations of  $\{1, 2, 3\}$ . The mass scaling parameter  $m$  has no inherent meaning and can be chosen arbitrarily, since it only serves as a scaling of the coordinates, it is not to be confused with the two-body reduced mass of previous sections. For equal mass particles the choice  $m = m_i = m_j = m_k$  is

obvious, such that  $\mu_i = \frac{1}{2}$  and  $\mu_{jk} = \frac{2}{3}$ . For chapter 6, however, the masses will differ when a mixed system will be studied.

The choice of index  $i$  yields a specific coordinate set, as illustrated in Figure 2.4. The vector  $\mathbf{x}_i$  is the relative coordinate between particles  $j$  and  $k$  while the vector  $\mathbf{y}_i$  is the relative coordinate between the center-of-mass of particles  $j$  and  $k$ , and particle  $i$ .

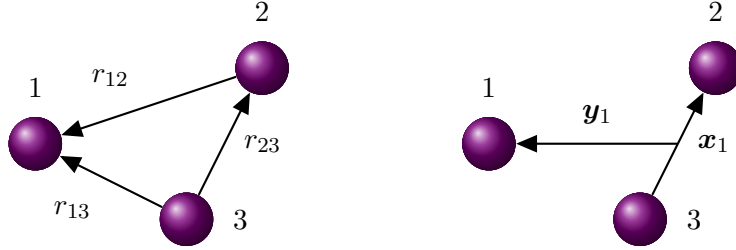


Figure 2.4: To the left, three particles and their relative coordinates. To the right, the same three particles and the Jacobi coordinate set with index  $i = 1$ .

The hyper-radial coordinates  $\rho$  and  $\alpha_i$  are defined from the Jacobi coordinates as

$$\rho^2 = x_i^2 + y_i^2, \quad \rho \sin \alpha_i = x_i, \quad \rho \cos \alpha_i = y_i, \quad (2.36)$$

where  $x_i = |\mathbf{x}_i|$  and likewise for  $y_i$ .  $\rho$  is known as the hyper-radius and  $\alpha_i$  is one of five hyper-angles, the remaining four being comprised of the directions of the vectors  $\mathbf{x}_i$  and  $\mathbf{y}_i$ . All five hyper-angles are collectively denoted as  $\Omega_i$ .

The hyper-radius is a measure of the overall size of the system, it is independent of the choice of Jacobi index. For large  $\rho$  either all three particles are far one another or one particle is far from the other two (i.e. when these form a bound dimer). Conversely, the hyper-radius is small only if all three particles are close to one another.

The hyper-angle,  $\alpha_i$ , is small when particles  $j$  and  $k$  are close together. When the particles are co-linear  $\alpha_i$  attains its maximal value of  $\pi/2$ .

The kinetic energy operator in the hyper-spherical coordinates is given by [Fedorov 2001b]

$$T = T_\rho + \frac{\hbar^2}{2m\rho^2}\Lambda^2, \quad T_\rho = -\frac{\hbar^2}{2m} \left( \rho^{-5/2} \frac{\partial^2}{\partial \rho^2} \rho^{5/2} - \frac{1}{\rho^2} \frac{15}{4} \right), \quad (2.37a)$$

$$\Lambda^2 = -\frac{1}{\sin(2\alpha_i)} \frac{\partial^2}{\partial \alpha_i^2} \sin(2\alpha_i) - 4 + \frac{l_{x_i}^2}{\sin^2 \alpha_i} + \frac{l_{y_i}^2}{\cos^2 \alpha_i}, \quad (2.37b)$$

where  $\Lambda^2$  is the grand angular momentum operator and  $l_{x_i}$  and  $l_{y_i}$  are the conjugate angular momenta to the Jacobi coordinates  $\mathbf{x}_i$  and  $\mathbf{y}_i$ .

For the wave function itself the hyper-radial adiabatic expansion is applied

$$\Psi_i(\rho, \Omega_i) = \rho^{-5/2} \sum_n f_n(\rho) \Phi_n(\rho, \Omega_i), \quad (2.38)$$

where  $f_n(\rho)$  is a radial wave function and  $\Phi_n(\rho, \Omega)$  is an angular wave function. The radial dependence of  $\Phi_n$  is slow when compared to  $f_n$ .

Using the hyper-radial adiabatic expansion, eq. (2.38), along with eqs. (2.37) the Schrödinger equation  $(T + V)\Psi = E\Psi$  yields a hyper-angular equation

$$\left( \Lambda^2 + \frac{2m\rho^2}{\hbar^2} V \right) \Phi_n(\rho, \Omega_i) = \lambda_n(\rho) \Phi_n(\rho, \Omega_i), \quad (2.39)$$

and a set of coupled radial equations

$$\left( -\frac{d^2}{d\rho^2} + \frac{\lambda_n + 15/4}{\rho^2} - Q_{nn}(\rho) - \frac{2mE}{\hbar^2} \right) f_n(\rho) = \sum_{m \neq n} \left( 2P_{nm}(\rho) \frac{d}{d\rho} + Q_{nm}(\rho) \right) f_m(\rho), \quad (2.40)$$

where the terms  $P_{nm}$  and  $Q_{nm}$ , known as adiabatic potentials, are given by

$$P_{nm}(\rho) = \left\langle \Phi_n \left| \frac{\partial}{\partial \rho} \right| \Phi_m \right\rangle_{\Omega_i}, \quad Q_{nm}(\rho) = \left\langle \Phi_n \left| \frac{\partial^2}{\partial \rho^2} \right| \Phi_m \right\rangle_{\Omega_i}, \quad (2.41)$$

where angle brackets indicate integration over hyper-angles  $\Omega_i$  and  $m$  is the mass scaling parameter from eq. (2.35).

The approach to solving this system of equations involves first solving the angular equation (2.39) for fixed  $\rho$  to obtain  $\lambda_n(\rho)$ . Then the radial equations can be solved using  $\lambda_n(\rho)$  as part of the radial potentials. This is similar to the Born-Oppenheimer approximation where the fast-moving dynamics is integrated out yielding an effective potential for the slow-moving part. The radial potential with  $\frac{\lambda_n + 15/4}{\rho^2}$  is in essence a hyper-angular centrifugal barrier similar to the usual centrifugal barrier of eq. (2.2).

In this thesis we never solve the full system (2.40). First, we find numerically that the parameters  $P$  and  $Q$  are very small compared to the effective  $\lambda$ -potential when using the zero-range two-body potentials. This is a great simplification as they are not easily calculated. Second, the expansion in eq. (2.38) is terminated after the first term, i.e. only  $n = 0$  is included in calculations involving the radial equation directly. When dealing with Efimov physics this has been proven to be quite a good approximation [Nielsen 2001]

and leaves for a much easier calculation of the results as well as an easier interpretation of the model. Therefore, the actual equation that will be used is

$$\left( -\frac{d^2}{d\rho^2} + \frac{\lambda_0 + 15/4}{\rho^2} - \frac{2mE}{\hbar^2} \right) f_0(\rho) = 0. \quad (2.42)$$

### 2.2.2 The zero-range model, hyper-spherical edition

In this section the hyper-angular equation (2.39) is solved to obtain the eigenvalue  $\lambda_n$  as function of hyper-radius,  $\rho$ . This is done by applying the zero-range model from section 2.1.1 to three-body systems.

Two-body interactions in a three-body system is most easily dealt with using Faddeev decomposition where the wave function is split into three components, one for each two-body subsystem

$$\Phi(\rho, \Omega) = \sum_{i=1}^3 \frac{\varphi_i(\rho, \alpha_i)}{\sin(2\alpha_i)}, \quad (2.43)$$

where  $\varphi_i(\rho, \alpha_i)$  is the angular wave function for the particle pair  $\{j, k\}$ . The subscript  $n$  from eq. (2.39) has been suppressed. The factor  $\sin(2\alpha_i)$  is for convenience in the final equations. The potential is equally described as a sum of two-body potentials  $V = \sum_i V_i$  where again  $V_i$  is the interaction between particles  $j$  and  $k$ . With these decompositions eq. (2.39) becomes a sum of three identical terms, one for each particle

$$(\Lambda - \lambda(\rho)) \frac{\varphi_i(\rho, \alpha_i)}{\sin(2\alpha_i)} + \frac{2m\rho^2}{\hbar^2} V_i \frac{\varphi_i(\rho, \alpha_i)}{\sin(2\alpha_i)} = 0, \quad i = 1, 2, 3. \quad (2.44)$$

As noted in section 2.1.1 it is not necessary to include all angular momentum states since the energy is very low in our system. In eq. (2.44) we will thus set  $l_{x_i} = l_{y_i} = 0$  and use only  $s$ -wave states, greatly simplifying the grand angular momentum operator  $\Lambda^2$ . For non-zero separation, i.e.  $\alpha_i \neq 0$ , and since zero-range potentials are used, eq. (2.44) simplifies further into

$$\frac{\partial^2}{\partial \alpha_i^2} \varphi_i(\rho, \alpha_i) = -[4 + \lambda(\rho)] \varphi_i(\rho, \alpha_i) = -\nu^2 \varphi_i(\rho, \alpha_i), \quad (2.45)$$

where  $\nu^2 = 4 + \lambda$ . Both  $\nu$  and  $\lambda$  will be referred to as angular eigenvalues and will be used interchangeably depending on context. The solution to eq. (2.45) is

$$\varphi_i = \varphi(\rho, \alpha_i) = N_i(\rho) \sin \left( \nu(\rho) \left[ \alpha_i - \frac{\pi}{2} \right] \right), \quad (2.46)$$

where  $N_i(\rho)$  is a normalization constant. The choice of phase ensures that the total wave function remains finite at  $\alpha_i = \frac{\pi}{2}$ .

The zero-range boundary condition from eq. (2.9) takes the following form [Fedorov 2001b]

$$\left. \frac{\partial \ln(r_{jk}\Phi)}{\partial r_{jk}} \right|_{r_{jk}=0} = -\frac{1}{a_i}, \quad (2.47)$$

where  $r_{jk}$  is the distance between particles  $j$  and  $k$  and  $a_i$  is the corresponding scattering length between them. In the limit  $r_{jk} \rightarrow 0$ , eq. (2.36) gives

$$r_{jk} = \frac{x_i}{\sqrt{\mu_i}} \approx \frac{\rho \alpha_i}{\sqrt{\mu_i}}, \quad (2.48)$$

for small  $\alpha_i$  and fixed  $\rho$ . The boundary condition becomes

$$\left. \frac{\partial(\alpha_i \Phi)}{\partial \alpha_i} \right|_{\alpha_i=0} = -\frac{\rho}{\sqrt{\mu_i}} \frac{1}{a_i} \alpha_i \Phi \Big|_{\alpha_i=0}. \quad (2.49)$$

To apply this boundary condition to all three two-particle wave functions they must all be expressed in the same Jacobi coordinate system, for instance the one in Figure 2.4. This is done using the kinematic rotation operator  $\mathcal{R}$ , that rotates the wave function from system  $k$  to system  $j$  and is defined by [Fedorov 2001b]

$$\mathcal{R}[\varphi_k](\alpha_j) = \frac{1}{\sin(2\phi_{jk})} \int_{|\phi_{jk}-\alpha_j|}^{\frac{\pi}{2}-|\frac{\pi}{2}-\phi_{jk}-\alpha_j|} \varphi_k(\alpha_k) d\alpha_k, \quad (2.50)$$

where

$$\phi_{jk} = \arctan \left( \sqrt{\frac{m_i(m_1 + m_2 + m_3)}{m_j m_k}} \right). \quad (2.51)$$

For three identical particles  $\phi_{jk} = \frac{\pi}{3}$  and the following results hold for equal mass particles only. In the boundary condition (2.49) the Faddeev components are replaced by

$$\varphi_1(\alpha_1) + \varphi_2(\alpha_2) + \varphi_3(\alpha_3) \rightarrow \varphi(\alpha_i) + 2\mathcal{R}[\varphi_k](\alpha_i), \quad (2.52)$$

and finally

$$\left. \frac{\partial(\varphi_i + 2\mathcal{R}[\varphi])}{\partial \alpha_i} \right|_{\alpha_i=0} = -\frac{\rho}{\sqrt{\mu_i}} \frac{1}{a_i} (\varphi_i + 2\mathcal{R}[\varphi]) \Big|_{\alpha_i=0}. \quad (2.53)$$

With eq. (2.46) the rotated wave functions become

$$\mathcal{R}[\varphi_k](\alpha_j) = \frac{4N}{\nu\sqrt{3}} \begin{cases} -\sin\left(\frac{\nu\pi}{6}\right) \sin(\nu\alpha_j) & , 0 \leq \alpha_j \leq \frac{\pi}{3} \\ \sin\left(\frac{\nu\pi}{3}\right) \sin\left(\nu\left[\alpha_j - \frac{\pi}{2}\right]\right) & , \frac{\pi}{3} \leq \alpha_j \leq \frac{\pi}{2} \end{cases} \quad (2.54)$$

and finally the boundary condition becomes

$$\frac{\nu \cos\left(\frac{\nu\pi}{2}\right) - \frac{8}{\sqrt{3}} \sin\left(\frac{\nu\pi}{6}\right)}{\sin\left(\frac{\nu\pi}{2}\right)} = \frac{\rho}{\sqrt{\mu}a}, \quad (2.55)$$

where the index on  $a$  and  $\mu$  has been removed since all particles are equal and their interactions also.

This is the fundamental equation of this thesis, it is the foundation of the two more elaborate models that include the effective range. Any solution  $\nu(\rho)$  to this equation will depend only on the ratio  $\frac{\rho}{\sqrt{\mu}a}$  so it is in principle necessary to solve eq. (2.55) only once. In general it can be solved only numerically, but in order to do this efficiently some analytical properties are important to know.

Some interesting analytical solutions are found in the limit of  $\rho \gg |a|$ . This corresponds to either all three particles far from each other or two of the particles bound in a sub-system and the third particle far away (the latter scenario only for positive  $a$ ).

Figure 2.5 shows the adiabatic potentials for  $n = 0$  and  $n = 1$  for both positive and negative scattering length,  $a$ . The interpretation of a dimer and a free particle is given in the channel marked with  $n = 0$  and three free particles in the channels marked with  $n = 1$ . The asymptotic value of the  $n = 0$  potential is the binding energy of the dimer. The channels will also be called adiabatic channels or adiabatic potentials.

*Adiabatic channel  $n = 0$*

In the asymptotic limit of large  $\rho$  compared to  $a > 0$  an analytical solution is available. The lowest solution, denoted  $n = 0$  in the adiabatic expansion eq. (2.38), is found when the eigenvalue  $\nu_0$  is completely imaginary. Assume in the large  $\rho/a$  limit that  $\nu_0 = ic\rho$  with  $c \in \mathbb{R}$

$$\frac{\rho}{\sqrt{\mu}a} = \frac{ic\rho \cosh\left(c\rho\frac{\pi}{2}\right) - \frac{8}{\sqrt{3}}i \sinh\left(c\rho\frac{\pi}{6}\right)}{i \sinh\left(c\rho\frac{\pi}{2}\right)} \xrightarrow{\rho \rightarrow \infty} |c|\rho, \quad (2.56)$$

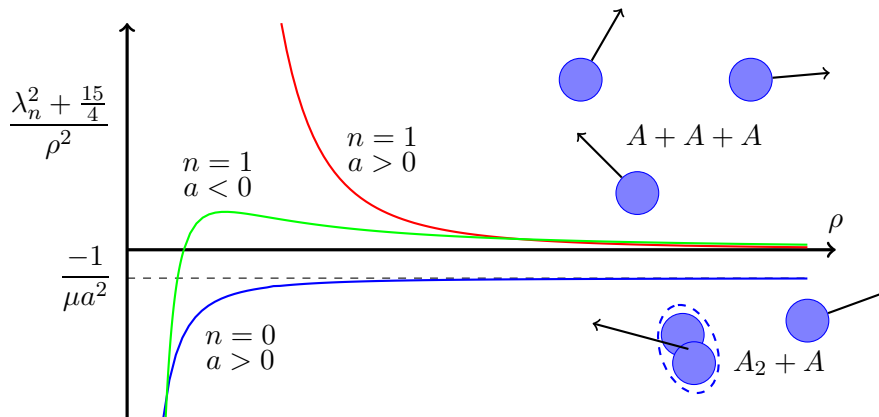


Figure 2.5: The adiabatic potentials for positive (the blue and red lines) and negative (the green line) scattering length  $a$ . The upper channels,  $n = 1$ , correspond, at large  $\rho$ , to three free particles,  $A + A + A$ , far from one another for both positive and negative  $a$ . The lower channel,  $n = 0$ , corresponds, at large  $\rho$ , to one free particles,  $A$ , and one dimer (shallow bound state of two particles),  $A_2$ . The asymptotic value for large  $\rho$  of the  $n = 0$  potential corresponds to the dimer binding energy. For negative  $a$  there is no similar potential.

where now  $i$  is the complex unit. The right hand side is always positive, so a solution is obtained only when the scattering length,  $a$ , is also positive. Thus for large values of  $\rho/a$  when  $a > 0$

$$\nu_0(\rho) \stackrel{\rho \rightarrow \infty}{\approx} \frac{i\rho}{\sqrt{\mu a}}. \quad (2.57)$$

In terms of the radial potential of eq. (2.42) this solution yields the lowest potential with an asymptotic value of (in units of  $\hbar = m = 1$ )

$$\frac{\lambda_0 + \frac{15}{4}}{\rho^2} = \frac{\nu_0^2 - \frac{1}{4}}{\rho^2} \stackrel{\rho \rightarrow \infty}{\approx} \frac{-1}{\mu a^2}. \quad (2.58)$$

This value corresponds to the binding energy of a two-body subsystem in the  $n = 0$  channel.

*Adiabatic channel  $n = 1$*

The next solution is obtained by noting that  $\nu = 2$  yields a left hand side that is infinite and thus also corresponds to the large  $\rho$  limit. Assuming the form

$$\nu_1 = 2 + \frac{c}{x} + \frac{d}{x^2}, \quad (2.59)$$

where  $x = \frac{\rho}{\sqrt{\mu a}}$  and  $c$  and  $d$  are constants. To obtain  $c$  and  $d$  we put eq. (2.59) into eq. (2.55). Taylor-expansion of  $\frac{1}{x}$  around 0 and comparison of terms in like powers of  $x$  yields

$$c = \frac{12}{\pi}, \quad d = \frac{8(3\sqrt{3} + 2\pi)}{\pi^2\sqrt{3}}. \quad (2.60)$$

This expression for  $\nu_1$  is accurate to within 1% for  $x > 5$ . It is furthermore valid for the scattering length,  $a$ , both positive and negative.

A practical application of these asymptotic limits eq. (2.57) and eq. (2.59) is described in appendix A where they are used as initial guesses for the numerical solver routine.

*The  $a = \infty$  limit*

Precisely on resonance the scattering length diverges to either plus or minus infinity. This situation is known as the universal limit and is the origin of one of the most interesting effects in three-body physics, namely the Efimov effect. The eigenvalue equation in this limit is

$$\nu_n \cos\left(\frac{\nu_n \pi}{2}\right) - \frac{8}{\sqrt{3}} \sin\left(\frac{\nu_n \pi}{6}\right) = 0. \quad (2.61)$$

Again the solution for lowest the potential is imaginary  $\nu_0 = is_0$  where  $s_0 = 1.0062378$  whereas the next solution is  $\nu_1 = 4.46529$ .

### 2.2.3 Efimov and Thomas effects

With the basic properties of the angular eigenvalues established we now turn to the radial equation (2.42). Whereas the zero-range approximation yielded some useful analytical results the radial equation is not quite so easy to work with. In the universal limit  $a = \infty$ , or correspondingly  $\rho = 0$ , however, an important analytical result can be derived.

Using the value  $\nu_0 = is_0$  in the radial equation (2.42) we get

$$\left(-\frac{d^2}{d\rho^2} + \frac{-s_0^2 - \frac{1}{4}}{\rho^2} - \frac{2mE}{\hbar^2}\right) f_0(\rho) = 0. \quad (2.62)$$

At very short distances,  $\rho \ll k^{-1}$  where  $k^2 = 2mE/\hbar^2$ , the energy term can be neglected. With an ansatz for the wave function of the form  $f_0 = \rho^n$ , a solution is found for  $n = \frac{1}{2} \pm is_0$  or

$$f_0(\rho) = \rho^{\frac{1}{2} \pm is_0} = \sqrt{\rho} \exp(\pm is_0 \ln \rho). \quad (2.63)$$

When  $\rho \rightarrow 0$  the exponential term will oscillate indefinitely, corresponding to an infinite number of bound states. This is known as the Thomas effect [Thomas 1935] and is caused by a breakdown of the short-range assumption of the contact interaction potential. Physical potentials do obviously not have an infinite attraction at zero extension and do therefore not suffer from this breakdown.

An important implication of this feature is that solving the radial equation (2.42) cannot be done from  $\rho = 0$  without modification. One approach is to simply not include the origin but start at a finite value,  $\rho_{\text{cut}}$ , with the boundary condition  $f(\rho_{\text{cut}}) = 0$ . This is known as a regularization cut-off [Fedorov 2001a] and can be attributed to the fact that three-body physics cannot be determined by two-body physics alone in the zero-range approximation.

The WKB-method can be used to estimate the trimer bound state energies in the universal limit using the quantization condition (with  $m = \hbar = 1$ ) [Griffiths 2005]

$$\int_{\rho_{\text{cut}}}^{\rho_t} d\rho \sqrt{2E_p - \frac{\nu_0(\rho)^2}{\rho^2}} = \pi \left( p - \frac{1}{4} \right), \quad (2.64)$$

where the integer  $p = 1, 2, \dots$  indicates the ground state, first excited,  $\dots$  etc. The regularization cut-off  $\rho_{\text{cut}}$  is used as the inner turning point of the WKB integral and correspondingly  $\rho_t$  is the outer classical turning point, for which  $2E_p = \nu_0(\rho_t)^2/\rho_t^2$ .

Note that in the integrand in eq. (2.64) the so-called Langer correction term has been included. When applying the WKB approximation to radial potentials this has been proven to yield much better results [Langer 1937]. In standard quantum mechanics this is done by replacing  $l(l+1)$  in the centrifugal barrier term by  $(l + \frac{1}{2})^2$  or equivalent adding  $1/4$  in the numerator. This is why the term  $\nu_0^2 - 1/4$  is simply  $\nu_0^2$  in the above.

In the universal limit  $a = \infty$ , where  $\rho_t = s_0/\sqrt{-2E_p}$ , eq. (2.64) can be solved approximately to give the trimer bound state energy

$$E_p \approx -\frac{2s_0^2}{\rho_{\text{cut}}^2} \exp\left(-\frac{2\pi p}{s_0} + \frac{\pi}{2s_0} - 2\right). \quad (2.65)$$

Here we again see the Thomas effect, since the binding energy diverges as  $\rho_{\text{cut}}^2$  when  $\rho_{\text{cut}} \rightarrow 0$ . Since  $\rho_{\text{cut}}$  is the only available length scale in this limit this is the only possible relation between the energy and  $\rho_{\text{cut}}$ .

Another important result from this calculation is the scaling of the energy with state number  $p$ , namely  $E_{p+1} = e^{-2\pi/s_0} E_p \approx E_p/515$ . This is precisely

the Efimov effect: in the universal limit there exists an infinite number of bound states with a geometric scaling law for the binding energies. Note that without the Langer correction term in eq. (2.64) the Efimov scaling in eq. (2.65) would not have been correctly obtained, which justifies its inclusion.

### 2.2.4 The two-channel model, hyper-spherical edition

Here we combine the two-channel model from section 2.1.5 with the hyper-spherical formalism of section 2.2.2 to obtain the two-channel hyper-spherical model. This section follows from [Sørensen 2013a].

The two-component angular wave function is  $\Phi(\rho, \Omega_i) = \begin{bmatrix} \Phi_{\text{closed}}(\rho, \Omega_i) \\ \Phi_{\text{open}}(\rho, \Omega_i) \end{bmatrix}$  with the same 'open' and 'closed' notation as in section 2.1.5. The boundary condition is a mix of eq. (2.17) and eq. (2.49).

$$\frac{\partial}{\partial \alpha_i} \begin{bmatrix} \alpha_i \Phi_{\text{closed}} \\ \alpha_i \Phi_{\text{open}} \end{bmatrix} \Big|_{\alpha_i=0} = \frac{\rho}{\sqrt{\mu_i}} \begin{bmatrix} \frac{-1}{a_{i,\text{open}}} & \beta_i \\ \beta_i & \frac{-1}{a_{i,\text{closed}}} \end{bmatrix} \begin{bmatrix} \alpha_i \Phi_{\text{closed}} \\ \alpha_i \Phi_{\text{open}} \end{bmatrix} \Big|_{\alpha_i=0}, \quad (2.66)$$

where  $\beta_i$  is a coupling parameter and index  $i$  denotes the Jacobi-set. The Jacobi-index is suppressed from here on, since only identical particles are considered. The hyper-angular equation (2.39) becomes

$$\left( \Lambda + \frac{2m\rho^2}{\hbar^2} \left[ V + \begin{bmatrix} \epsilon & 0 \\ 0 & 0 \end{bmatrix} \right] \right) \Phi(\rho, \Omega) = \lambda(\rho) \Phi(\rho, \Omega), \quad (2.67)$$

where the scalar quantities,  $\Lambda$  and  $V$ , are multiplied by the  $2 \times 2$ -identity matrix. The resulting differential equations for the two components are identical except for the replacement  $\tilde{\lambda}(\rho) = \lambda(\rho) - \kappa^2 \rho^2$  with  $\kappa^2 = 2m\epsilon/\hbar^2$  in the equation for  $\Phi_{\text{closed}}$ . The Faddeev components in the two-channel model with zero-range two-body interactions are

$$\varphi_{\text{open}}(\rho, \alpha) = N(\rho) \sin \left[ \nu(\rho) \left( \alpha - \frac{\pi}{2} \right) \right], \quad (2.68a)$$

$$\varphi_{\text{closed}}(\rho, \alpha) = \tilde{N}(\rho) \sin \left[ \tilde{\nu}(\rho) \left( \alpha - \frac{\pi}{2} \right) \right], \quad (2.68b)$$

with  $\tilde{\nu}^2 = 4 + \tilde{\lambda} = \nu^2 - \kappa^2 \rho^2$ .

After rotations into the same Jacobi coordinate set using eq. (2.50) the boundary condition eq. (2.66) becomes the  $2 \times 2$  system of equations

$$\begin{bmatrix} \frac{\rho}{\sqrt{\mu}} \beta \sin \left( \frac{\nu\pi}{2} \right) & f_{\text{closed}}(\tilde{\nu}) \\ f_{\text{open}}(\nu) & \frac{\rho}{\sqrt{\mu}} \beta \sin \left( \frac{\tilde{\nu}\pi}{2} \right) \end{bmatrix} \begin{bmatrix} N \\ \tilde{N} \end{bmatrix} = 0, \quad (2.69)$$

where

$$f_{\text{open/closed}}(x) = x \cos\left(\frac{x\pi}{2}\right) - \frac{8}{\sqrt{3}} \sin\left(\frac{x\pi}{6}\right) - \frac{\rho}{\sqrt{\mu} a_{\text{open/closed}}} \sin\left(\frac{x\pi}{2}\right). \quad (2.70)$$

The two-channel version of eq. (2.20) is

$$\frac{\rho^2 \beta^2}{\mu} \sin\left(\frac{\nu\pi}{2}\right) \sin\left(\frac{\tilde{\nu}\pi}{2}\right) - f_{\text{open}}(\nu) f_{\text{closed}}(\tilde{\nu}) = 0. \quad (2.71)$$

To find the effective scattering length,  $a_{\text{eff}}$ , of this two-level system, we note that the lowest eigenvalue in the single-channel zero-range model,  $\nu_0$ , goes asymptotically as  $\nu_0 \rightarrow i\rho/\sqrt{\mu}a$  for  $\rho \rightarrow \infty$ , see eq. (2.57). Taking the same limit in eq. (2.71) with the  $\nu = \nu_0 = i\rho/\sqrt{\mu}a_{\text{eff}}$  gives this equation for  $a_{\text{eff}}$

$$\beta^2 - \left(\frac{1}{a_{\text{eff}}} - \frac{1}{a_{\text{open}}}\right) \left(\sqrt{\frac{1}{a_{\text{eff}}^2} + \mu\kappa^2} - \frac{1}{a_{\text{closed}}}\right) = 0. \quad (2.72)$$

Given a set of model parameters, the effective scattering length can be found from this equation. The general solution for  $a_{\text{eff}}$  as a function of the parameters  $\beta, \kappa, a_{\text{closed}}, a_{\text{open}}$  and  $\mu$  is not very handy. Near a Feshbach resonance, however, where  $a$  diverges, we have  $a \gg \kappa^{-1}$ , the square root in eq. (2.72) simplifies such that an approximate solution can be obtained

$$\frac{1}{a_{\text{eff}}} \approx \frac{1}{a_{\text{open}}} + \frac{\beta^2}{\sqrt{\mu}\kappa - \frac{1}{a_{\text{closed}}}}. \quad (2.73)$$

In spite of the apparent difference in derivations this looks quite similar to eq. (2.22).

Taking the expression for the effective range eq. (2.23) and making the same replacement that leads to eq. (2.73) from eq. (2.23), i.e.  $\kappa \rightarrow \sqrt{\mu}\kappa$ , gives

$$R = \frac{-\beta^2}{\sqrt{\mu}\kappa \left(\sqrt{\mu}\kappa - \frac{1}{a_{\text{closed}}}\right)^2}. \quad (2.74)$$

Correspondingly eq. (2.25) becomes

$$R_0 = \frac{-1}{\sqrt{\mu}\kappa_0 a_{\text{open}}^2 \beta^2}. \quad (2.75)$$

For  $a_{\text{eff}} = \infty$ , equivalently  $\rho = 0$ , the solutions are the same as for the single-channel zero-range model. This means that since  $\nu_0$  is imaginary, the

Thomas effect persists even when the effective interaction has a non-zero effective range. This can be understood by noticing that the two-channel model consists of two single-channel zero-range models that are coupled together by a coupling potential of zero separation. This means that there is no scale coming from the coupling that can regularize the three-body problem and in turn one still needs to introduce a short-distance cut-off.

### 2.2.5 Effective range expansion, hyper-spherical edition

Here the briefly mentioned effective range expansion of section 2.1.2 is presented in the hyper-spherical formalism. This model has the effective range,  $R$ , as an explicit parameter and is thus simpler than the two-channel model. It is, however, not based on any physical model but serves as a simpler way of including the effective range. The simplicity allows for some analytical results to be derived that are not readily available in the two-channel model but coincide nicely with the corresponding numerical calculations.

The effective range expansion model uses eq. (2.8) as the boundary condition. There,  $R$  is just a parameter, independent off  $a$ . Later, however, the dependency in eq. (2.24) will be adopted for actual calculations. In reality both  $a$  and  $R$  depend on the external magnetic field,  $B$ , but this dependency is implicitly fulfilled with the  $R(a)$  expression.

The boundary condition (2.49) becomes [Fedorov 2001b] (suppressing the index  $i$ )

$$\left. \frac{\partial(\alpha\Phi)}{\partial\alpha} \right|_{\alpha=0} = \frac{\rho}{\sqrt{\mu}} \left[ -\frac{1}{a} + \frac{1}{2} R \frac{\mu\nu^2}{\rho^2} \right] \alpha\Phi \Big|_{\alpha=0}, \quad (2.76)$$

where  $R$  is the effective range between the particles, which are assumed identical, and the momentum in eq. (2.8) is given by  $k = \nu/(\sqrt{2}\rho)$  [Fedorov 2001b]. Again assuming that all particles are identical, the eigenvalue eq. (2.55) becomes

$$\frac{\nu \cos\left(\frac{\nu\pi}{2}\right) - \frac{8}{\sqrt{3}} \sin\left(\frac{\nu\pi}{6}\right)}{\sin\left(\frac{\nu\pi}{2}\right)} = \frac{\rho}{\sqrt{\mu}} \left( \frac{1}{a} - \frac{1}{2} R \frac{\mu\nu^2}{\rho^2} \right). \quad (2.77)$$

As before, the limit  $\rho \rightarrow \infty$  grants a little insight. With  $\nu = i\rho/a_{\text{eff}}$  one obtains for positive  $a$

$$a_{\text{eff}} = \frac{a + \sqrt{a^2 - 2aR}}{2}. \quad (2.78)$$

For  $R = 0$  this appropriately yields  $a_{\text{eff}} = a$ . For  $R \ll a$ , the dimer binding energy is

$$E_D = \frac{1}{a_{\text{eff}}^2} \approx \frac{-1}{a^2} \left( 1 + \frac{R}{a} \right). \quad (2.79)$$

Thus the dimer system can become more bound or less bound depending on the sign of the effective range. In the case of atomic Feshbach resonances the effective range is negative [Chin 2010], which lowers the binding energy of the dimers, i.e. it becomes less negative.

### The short distance limit

The small  $\rho$  limit is distinct in this model. For  $\rho \rightarrow 0$  we write the lowest eigenvalue as  $\nu_0 = \sqrt{b\rho + c\rho^2}$  which yields

$$b = \frac{16\pi - 12\sqrt{3}}{3\sqrt{3}\pi\sqrt{\mu}R}, \quad c = \frac{1458R + (256\pi^2 + 240\sqrt{3}\pi - 972)a}{729a\mu R^2}, \quad (2.80)$$

which is valid for  $\rho \ll |R|$ . Thus  $\nu_0^2 \propto \rho$  in the small  $\rho$  limit. This means that a regularization cut-off is not urgently needed in this model. The calculation leading to eq. (2.63) would have  $s_0 = 0$  and  $f(\rho)$  would not oscillate indefinitely. Also, the integral in eq. (2.64) would be finite for  $\rho_t = 0$  since the divergent integrand would be of the form  $1/\sqrt{\rho}$  which can easily be integrated. Thus the Thomas collapse is avoided. The Efimov effect persists, however. Even though a cut-off is not needed in this model we will still apply one since this allows us to use the cut-off as a fitting parameter when comparing to experimental data.

The limit of  $R \rightarrow 0$  should correspond to the zero-range model. This is indeed still the case despite the apparent divergence of the expressions in eq. (2.80). This is best seen in Figure 3.1 where the eigenvalues are plotted for several different effective ranges. For small  $|R|$  the effective range expansion model eigenvalues stay close to the zero-range model eigenvalues until at  $\rho \sim |R|$  where the eigenvalues tend towards zero with a slope that increases for decreasing  $|R|$  precisely as in eq. (2.80).

### Positive effective range

There is no apparent reason that we cannot choose  $R$  to be positive in this model. However, if  $R$  is chosen too large, for some specific value of  $a$ , the eigenvalue equation (2.77) cannot be solved, neither for real nor complex eigenvalues. We will investigate the effects of the sign of the effective range briefly

in chapter 3. To do so without the here mentioned breakdown an additional term, proportional to  $k^4$ , must be included in the effective range expansion model. The additional parameter,  $P$ , chosen to be dimensionless, is known as the shape parameter [Fedorov 2001b]

$$\lim_{k \rightarrow 0} k \cot \delta(k) = -\frac{1}{a} + \frac{1}{2}Rk^2 + PR^3k^4. \quad (2.81)$$

The equations (2.76) and (2.77) get similar additional terms. The shape parameter can be derived for the two-channel model if the Taylor expansion of eq. (2.21) is carried out to fourth order in  $k$ . For typical values of  $a$  and  $R$  this yields  $P \sim 0.1$ . A similar calculation for the finite box potential also yields similar values of  $P$ . 0.1 will thus be universally applied in this thesis where relevant.

### 2.3 Three-body recombination rate

A very important quantity that will be investigated in great detail in this thesis is the recombination rate which is currently the only experimental way to obtain information about three-body physics.

By recombination in this context is understood the process of three free particles  $A + A + A$  interacting with the result that two of them become bound (they form a dimer) and the third carries away excess energy and momentum. The resulting dimer  $A_2$  and free particle  $A$  have increased kinetic energy due to the overall increased binding energy in the system. The result is a loss of all three particles from the trap generally leading to atom number loss of the form [Zaccanti 2009]

$$\dot{n} = -\alpha_{\text{rec}}n^3, \quad (2.82)$$

where  $n$  is the atom number density,  $\alpha_{\text{rec}}$  is known as the recombination coefficient and the dot indicates derivative with respect to time.

The overall dependency for the recombination coefficient  $\alpha_{\text{rec}}$  can be obtained by simple dimensional analysis. Combining the scattering length (which is the only available length scale in the zero-range model) with the particle mass  $m$  and Planck's constant  $\hbar$  to obtain a unit of  $length^6/time$ , which is the unit of the recombination coefficient, can be done in one way only

$$\alpha_{\text{rec}} = C \frac{\hbar a^4}{m} \quad (2.83)$$

where  $C$  is a dimensionless proportionality factor that cannot be determined by this analysis. It turns out that  $C$  is log-periodic with the property that

$C(a) = C(22.7a)$  (in the case of equal mass particles). Furthermore, the overall  $a^4$  dependency is modulated by a series of characteristic minima in the spectrum for positive  $a$  and a corresponding series of maxima for negative  $a$ . See for instance Figures 3.6 and 5.5.

Two alternative ways of calculating the recombination coefficient will be presented here. Both rely on calculating the transition matrix element from the initial state of three free particles to the final state of a dimer and a free particle. What is meant by a bound dimer is slightly different depending on the sign of the scattering length. As noted earlier in section 2.1.3 there exist bound dimers for positive scattering lengths only. Or rather, only *weakly* bound dimers, with binding energy of the order  $1/a^2$ , exist for positive scattering length. Zero-range potentials can describe only these weakly bound states. For physical potentials the weakly bound dimer is the state just below threshold when the scattering length is large. Imagine tuning the potential strength such that the scattering length diverges, the divergence is a manifestation of the existence of the weakly bound dimer state. Of course in the real potential deeply bound states may also exist with binding energies of the order  $1/r_e^2$  where  $r_e$  is the physical range of the potential, but they do not concern us at this stage.

For negative scattering length,  $a$ , only the deeply bound states exist. These bound states cannot be described by zero-range potentials, neither in the two-channel nor in the effective range expansion model. Here, the effective range modifications apply only to the weakly-bound states.

These two very different meanings of bound dimers might suggest that the processes by which the recombination occurs are very different, depending on the sign of the scattering length. This is also clearly seen in the recombination coefficient, as noted above, with troughs/peaks for positive/negative scattering lengths. Two approaches to the problem will be taken. The methods share some of the same basic ideas but with some clear differences.

### 2.3.1 Hidden crossing theory

As noted in section 2.2.2 the adiabatic potentials for positive scattering length correspond, at large hyper-radius, to either three free particles,  $n = 1$ , or one free particle and the other two bound in a weak dimer,  $n = 0$ . The transition from the former state to the latter is known as recombination. The usual way of attacking this problem consists of solving the coupled set of equations in eq. (2.40) with a high number of adiabatic channels. This involves calculating not only the  $\lambda$ 's but also  $P$ 's and  $Q$ 's before the actual radial equations. This has been done [Wang 2011] and we do not seek to reproduce the results of

this method. Instead a much simpler approach is taken, namely the method of hidden crossings.

Introductory quantum mechanics [Griffiths 2005] presents the simple WKB approximation that has been already used in eq. (2.64) to estimate the bound state energies. A similar estimation can be done for the tunnelling probability through a potential barrier, as illustrated in Figure 2.6. The transmission amplitude,  $T$ , for tunnelling through the barrier given by  $V(x)$  is  $T \approx e^{-2\gamma}$  where

$$\gamma = \frac{1}{\hbar} \int_{x_a}^{x_b} |p(x)| dx = \frac{1}{\hbar} \int_{x_a}^{x_b} \sqrt{2m(E - V(x))} dx, \quad (2.84)$$

where  $x_a$  and  $x_b$  denote the classical turning points that correspond to the energy  $E$  such that  $E = V(x_a) = V(x_b)$ . Figure 2.6 illustrates the set-up, the wave incoming from the left is partially transmitted with the amplitude  $T$  and partially reflected with the amplitude  $R$ .

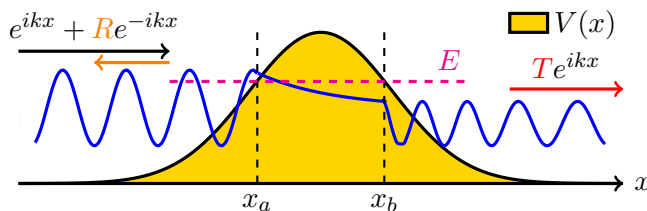


Figure 2.6: Tunnelling through a potential barrier. The points  $x_a$  and  $x_b$  indicate the classical turning points corresponding to the energy  $E$  such that  $V(x_a) = V(x_b) = E$ . To the left of the potential the wave consists of an incoming wave with amplitude 1 and a reflected wave with amplitude  $R$ . To the right of the potential there is only the transmitted wave with amplitude  $T$ .

Now imagine that the wave incoming from the left describes three free particles in the hyper-spherical picture while the transmitted wave describes a dimer and a free particle, i.e. the left wave lies on the adiabatic channel  $n = 1$  in Figure 2.5 and the right wave on channel  $n = 0$ . An integration path from  $n = 1$  to  $n = 0$  does not seem readily available, however, this is only the case on the real line.

Figure 2.7 is an extension of Figure 2.5 into the complex  $\rho$ -plane. For  $\text{Im}(\rho) = 0$  the figure is just Figure 2.5 at a tilted angle. Something interesting happens out in the complex plane. The potential curves do not get extended into separate sheets but are in fact part of the same multi-layered surface. The integration path marked in red is obtained by taking a small continuous step all the way, yet starting from one adiabatic potential,  $n = 1$ , and ending out in another,  $n = 0$ . This is because the shown path encircles the branch point

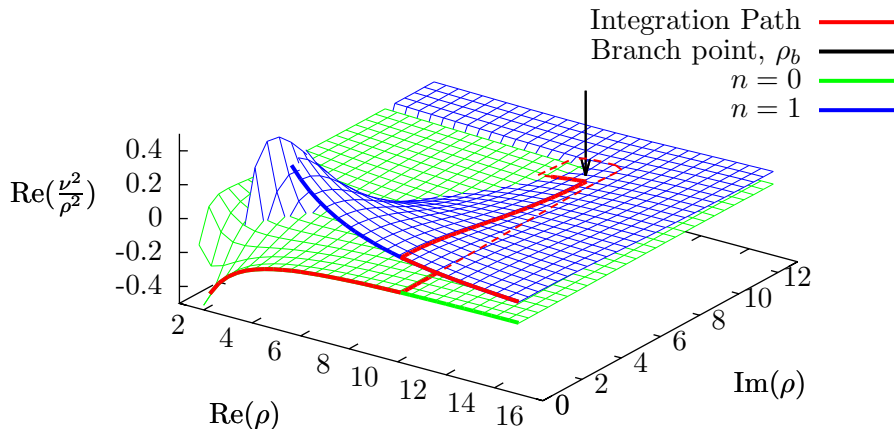


Figure 2.7: A visualization of a hidden crossing in the complex  $\rho$ -plane. The adiabatic radial potentials are extended to complex  $\rho$  which results in a sheet for each channel. The sheets intersect at the branch point,  $\rho_b$ , indicated by the arrow. An integration path (the red line) starting on one branch and encircling the branch point will return to the real axis on another branch.

marked by an arrow. This effect is akin to the square root function of complex numbers which is not defined on the negative real axis. Correspondingly, going around the branch point twice before heading back to the real line would lead back to the initial curve.

Near the branch point the eigenvalue  $\nu(\rho)$  behaves like a square root type function of  $\rho$ . The branch point is found by solving [Nielsen 2001]

$$\left. \frac{d\rho}{d\nu} \right|_{\nu_b} = 0, \quad (2.85)$$

for complex  $\nu_b$  and evaluate  $\rho_b = \rho(\nu_b)$  through eq. (2.55). In the single-channel zero-range model the branch-point is  $\rho_b \approx (2.592 + 2.974i)\sqrt{\mu}a$ . For the two-channel model  $\rho(\nu)$  is given only implicitly and eq. (2.85) must be solved numerically for each set of two-channel parameters. The above value for  $\rho_b$  is, however, still approximately correct. Likewise for the effective range expansion model.

The WKB integration starts at the outermost classical turning point in the adiabatic channel  $n = 1$ , goes towards the origin but stops at  $\rho_b$ , then goes out into the complex plane, around  $\rho_b$  and back to the real axis, now on

channel  $n = 0$  and down to the innermost turning point. As noted in section 2.2.3 the lower adiabatic channel diverges as  $\rho^{-2}$  for small  $\rho$ . Here enters the regularization cut-off, which puts the lower turning point at an infinite potential barrier at short distance. The integral takes the form

$$\Delta + iS = \int_{\text{path}} d\rho \sqrt{k^2 - \frac{\nu(\rho)^2}{\rho^2}}, \quad (2.86)$$

where 'path' is the integration path just described and  $\Delta + iS$  is a generalization of  $\gamma$  in eq. (2.84) with  $\Delta$  and  $S$  purely real. Note that again the Langer correction is applied as in eq. (2.64). The transition probability is given by

$$P(k) = 4e^{-2S} \sin^2 \Delta, \quad (2.87)$$

from which the recombination coefficient is found as [Nielsen 1999]

$$\alpha_{\text{rec}} = 8(2\pi)^2 3\sqrt{3} \frac{\hbar}{m} \lim_{k \rightarrow 0} \frac{P(k)}{k^4}, \quad (2.88)$$

with the wave number  $k$  defined by  $E = \hbar^2 k^2 / 2m$ .

The described integration path is actually the effective sum of two separate paths. One starts on the branch  $n = 1$  at large  $\rho$ , goes around the branch point and ends up on  $n = 0$ , goes in towards the innermost turning point and then out to large  $\rho$  on the  $n = 0$  branch with opposite sign in the integrand. The second path starts also on the branch  $n = 1$ , goes in to the classical turning point *on the  $n = 1$  branch*, then heads towards  $\rho_b$  and goes around it, back to the real axis on branch  $n = 0$  and then again out to large  $\rho$ . The coherent sum of the results of these two integration paths is exactly the same as for the 'path' described above [Nielsen 2001].

The more familiar form  $\alpha_{\text{rec}} = C(a)\hbar a^4/m$  (as for instance found in [Braaten 2006] or from the dimensional analysis argument above) can be found from the above equations in the universal limit,  $a = \infty$ , using the single-channel zero-range model where  $\nu_0(\rho) = is_0$ . Split the integral into two parts: one from the cut-off,  $\rho_{\text{cut}}$ , to the real part of the branch point,  $\rho_b$ , and another for the rest. Denote the first part by  $\Delta_1 + iS_1$ , then the result is  $\Delta_1 = s_0 \log\left(\frac{\text{Re}(\rho_b)}{\rho_{\text{cut}}}\right)$  and  $S_1 = 0$  since the potential is negative in the lower branch and  $k^2$  is positive and thus the integrand is purely real. From eq. (2.85) we have  $\text{Re}(\rho_b) \propto a$ . When plugging this into eq. (2.87) the log-periodic dependence is established. The rest of the integration path only leads to a constant phase shift  $\Delta_2$  independent of  $a$  since  $\nu(\rho)$  only depends on the ratio  $\rho/a$ .

That the limit for  $k \rightarrow 0$  exists can be seen from the integration on the upper branch. Here  $\nu_1 = 2$  asymptotically and the outer turning point is given by  $\rho_t = 2/k$ . On this branch the energy is lower than the potential and a purely imaginary contribution is found with the value  $S_2 = 2 \ln \frac{\rho_t}{\text{Re}(\rho_b)}$  where the factor of 2 is due to the value of  $\nu$ . Exponentiation leads to  $P(k) \propto \left(\frac{\text{Re}(\rho_b)}{\rho_t}\right)^2 \propto k^4 a^4$  since again  $\text{Re}(\rho_b) \propto a$  and  $\rho_t = 2/k$ . The Langer correction was again essential to obtain the correct behaviour.

The method for calculating the recombination coefficient when  $a$  is negative will be described in chapter 5.



## Chapter 3

# Finite range effects

*Effects of the finite effective range in the two-channel and effective range expansion models are investigated by comparing their predictions for the trimer bound state spectrum and recombination rates with the predictions from the single-channel zero-range model. A comparison to experimental data is also performed.*

---

In this chapter the effects of the effective range are investigated by comparing results for the single-channel zero-range model of section 2.2.2 to the two-channel model from section 2.2.4 and the effective range expansion model of section 2.2.5. The main effect is that the characteristic Efimov scaling factor, which equals 22.7 for identical particles when the effects of finite effective range are not included, depends on both the value and sign of the effective range. As noted previously in section 2.1.5 the two-channel model has negative effective range, so only the effective range expansion model is applied when investigating dependency on the sign of the effective range. The results are based on work from [Sørensen 2013c].

The comparison between the models is done first by plotting the adiabatic potentials for the different models and noting the differences. These simple plots provide good explanations for the effects observed in the calculated observables.

The dependency of the Efimov scaling factor on the effective range is found first by calculating the recombination coefficient for positive scattering lengths using the method of hidden crossing described in section 2.3.1. The effect is observed as a reduction of the distance between consecutive minima in the recombination spectrum.

On the negative  $a$  side this method cannot be used, instead the trimer

bound state spectrum is investigated. Specifically we look at a certain threshold value of  $a$  where the lowest Efimov trimer state appears from the three-body continuum. This threshold value of  $a$ , denoted as  $a^{(-)}$  in most papers, is known as the three-body parameter, which in recent studies [Berninger 2011, Naidon 2012b, Chin 2011, Wang 2012, Schmidt 2012] has an apparent universal relation to the van der Waals length of the inter-atomic two-particle potential. This effect is investigated further in the next chapter.

### 3.1 Model Comparison

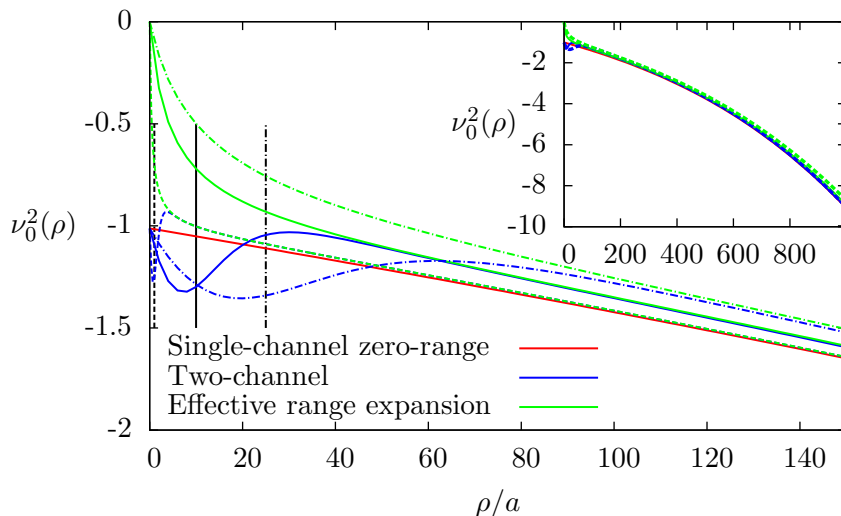


Figure 3.1: Small and large  $\rho$  behaviour of the hyper-angular eigenvalues for  $n = 0$ , for the three models with  $a = 500a_0$ ,  $R_0 = -a_0$  (short dash),  $R_0 = -10a_0$  (solid lines) and  $R_0 = -25a_0$  (dash dot) where  $a_0$  is the Bohr radius. The vertical black lines indicate  $|R_0|$  at these respective values. Notice how the eigenvalues for the effective range expansion model tend to 0 for  $\rho \rightarrow 0$ . As the discussion around eq. (2.80) suggests, this means that the model does not require a cut-off.

Before considering the recombination rates and the binding energies in the different models, we first make a comparison of the models in terms of the adiabatic eigenvalues  $\nu_0(\rho)$  that provide the effective potential for the three-body system in the hyper-radial equation (2.42). The models are compared in Figure 3.1 by explicitly plotting their associated eigenvalues. At large  $\rho$  all models have the same asymptotic value  $\nu^2 = -2\rho^2/a^2$  as noted in eq. (2.57)

(note that  $\mu = \frac{1}{2}$  in this chapter). This is more clearly illustrated in the inset of Figure 3.1, where the horizontal axis extends up to  $\rho/a = 1000$ . For intermediate distances  $\rho \gtrsim 2|R_0|$ , where  $R_0$  is the effective range at  $a = \infty$  from eq. (2.14), the finite-range models show surprisingly similar forms given their quite different formalism. The two-channel model has both a barrier with respect to the single-channel zero-range model as well as an inner pocket region. This feature is key to understanding some results of the full calculations in the later sections. The effective range expansion model only has a barrier with respect to (i.e. it is strictly larger than) the single-channel zero-range model.

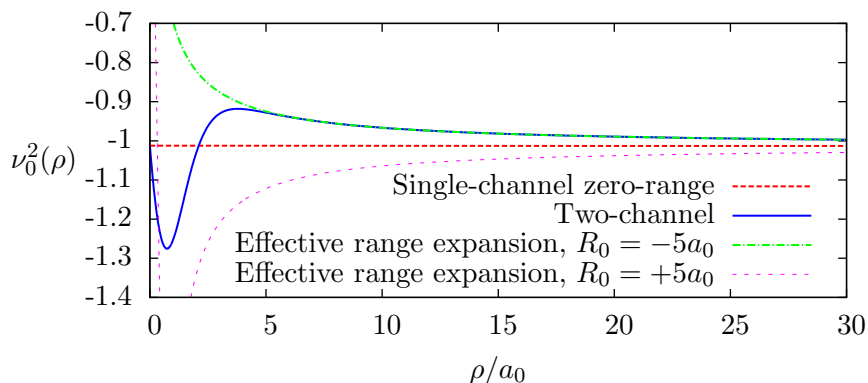


Figure 3.2: The same eigenvalues as in Figure 3.1 for  $a = \infty$ . Positive effective range is included for the effective range expansion model. The single channel solution has the constant value  $-s_0^2 \approx -1.012$ .

Figure 3.2 is similar, but plotted for  $a = \infty$ , where the same features are seen. Additionally the eigenvalue solution for the effective range expansion model is also plotted for positive effective range with the shape parameter from eq. (2.81)  $P = 0.1$ . It appears to have almost mirror symmetry around the single-channel zero-range solution, except for very short distances where both the positive and negative effective range solutions go to zero. For positive effective range only a pocket region is observed. The eigenvalues for  $n = 1$  would show very similar tendencies if they were plotted as in Figure 3.1 and Figure 3.2.

### 3.2 Bound trimers

Effects of the effective range are now considered by studying the trimer bound state spectrum for the different models. When the scattering length,  $a$ , is large, the WKB expression (2.64) yields the same trimer binding energy,  $E_T(a)$ , as the radial equation (2.42). However, for small  $a$  or energies close to 0, the radial equation provides the best results. The boundary conditions for the radial solutions are  $f(\rho_{\text{cut}}) = 0$ , following the regularization procedure, and  $f(\rho_{\text{max}}) = 0$  for some large  $\rho_{\text{max}}$ , chosen such that the bound state energy has converged to the desired degree of accuracy. Notice that we also regularize the effective range expansion model so that we can move the trimer bound state energies while keeping the effective range fixed.

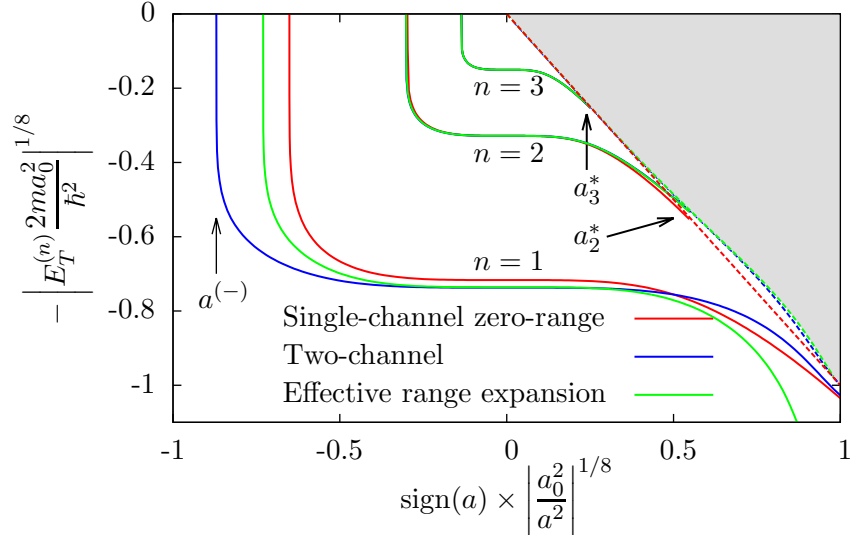


Figure 3.3: The trimer bound state energy,  $E_T^{(n)}$ , versus inverse scattering length,  $a$ , squared for  $R_0 = -5a_0$  where  $a_0$  is the Bohr radius. The superscript  $n = 1, 2, 3$  indicates the lowest, first excited and second excited trimer states, respectively. Both axes are scaled to the power 1/8 to reasonably fit the entire spectrum in the plot. Dashed lines indicate the atom-dimer threshold for positive scattering lengths. The annotated points  $a_i^*$  indicate where the trimer bound states disappear into the atom-dimer continuum, shown as the light grey area above the dashed lines. Likewise  $a^{(-)}$  indicates the threshold for the lowest trimer disappearing into the three-body continuum for negative  $a$ .

Figure 3.3 shows the three lowest trimer bound state energies,  $E_T^{(n)}$ , where  $n$  indicates the level of excitation, as function of the scattering length for each

of the three models. For positive  $a$  the dashed lines indicate the atom-dimer threshold which is given by the dimer binding energy  $-1/a^2$  for the single-channel zero-range model and by eq. (2.79) for the effective range expansion model. For the two-channel model this can be calculated only numerically, yet it agrees surprisingly well with the analytical formula for the effective range expansion model. It can be hard to discern in the figure, but the green and blue dashed curved are practically identical. The regularization cut-offs were chosen such that the excited trimer energies,  $n = 2$ , coincide with each other for all the models at  $|a| = \infty$ . The three spectra for  $n = 3$  are virtually identical. This is reasonable since the binding energy is very small for the  $n = 3$  states and hence the wave function lives at very large hyper-radius and is almost completely insensitive to short-range effects. However, for the lowest state,  $n = 1$ , a clear distinction between the models appears. At  $|a| = \infty$  the finite-range models give practically the same trimer energy, a factor of  $\sim 25.3^2$  times larger than the  $n = 2$  state (for this particular choice of effective range). In comparison the single-channel zero-range model trimer energy is only a factor of  $22.7^2$  times larger, which is the usual Efimov scaling factor.

### 3.2.1 Threshold for trimer creation

For negative scattering length,  $a$ , the value of  $a^{(-)}$  indicates the threshold scattering length for creation of the lowest Efimov trimer. When given in units of the van der Waals length,  $r_{\text{vdW}}$ , this quantity is the subject of much recent discussion since it seems to have the universal value of  $a^{(-)} \sim -9.8r_{\text{vdW}}$  for different cold atomic systems [Berninger 2011]. The relation between  $a^{(-)}$  and  $r_{\text{vdW}}$  is discussed in the next chapter. In this section we focus on finite range effects in  $a^{(-)}$  for the two models. Some other works that address finite range effects on the threshold value  $a^{(-)}$  can be found in [Thøgersen 2008] and [Naidon 2012b].

The results within the different models for  $a^{(-)}$  as a function of  $R_0$  are shown in Figure 3.4. Most noticeable is the decrease in  $a^{(-)}$  for the finite-range models compared to the single-channel zero-range model for negative  $R_0$ . This is partly due to the lower binding energy  $E_T^{(1*)} \equiv E_T^{(1)}|_{|a|=\infty}$ . The product  $\kappa^* a^{(-)}$  (where  $(\kappa^*)^2 = -2mE_T^{(1*)}/\hbar^2$ ) is universal in the single-channel zero-range model [Gogolin 2008]. Thus increasing  $|E_T^{(1*)}|$  will reduce  $|a^{(-)}|$ . However, this effect is not enough to account for the deviation from the single-channel zero-range result. The product  $|\kappa^* a^{(-)}|$  is further reduced for decreasing  $R_0$ , indicating a lower value of  $a^{(-)}$ .

Both finite-range models show the same trend for negative  $R_0$ . However,

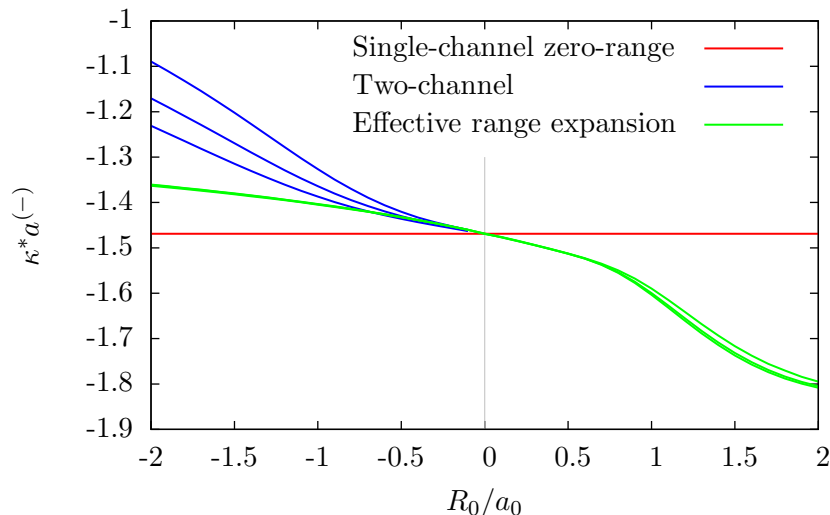


Figure 3.4: The product  $\kappa^* a^{(-)}$  as a function of effective range,  $R_0$ , where  $(\kappa^*)^2 = -2mE_T^{(1*)}/\hbar^2$  with  $E_T^{(1*)}$  being the binding energy of the lowest trimer at  $|a| = \infty$  and  $a^{(-)}$  is the threshold scattering length for trimer creation as indicated in Figure 3.3. The universal value  $\kappa^* a^{(-)} = -1.5076$  [Gogolin 2008] for the single-channel zero-range model is not correct for the lowest trimer, we find the value  $-1.469$  instead, independent of cut-off. The two-channel model curves are for different value coordinate-space cut-offs on the hyper-radial potential. The cut-off is 0.5, 0.6 and 0.7 in units of  $a_{\text{bg}}$  for the top, middle and bottom blue curves. For the effective range expansion model the dependency on the cut-off is insignificant. Note that the two-channel model only allows  $R_0 < 0$ . Here  $a_0$  is the Bohr radius and  $R_0$  is the effective range on resonance from eq. (2.14).

the value of the change is different for the two models when  $|R_0|$  gets sufficiently large. The plot also shows that for the two-channel model the effect depends on the cut-off. The cut-off, chosen for the purpose of illustration, but with reasonable values, is  $0.5a_{\text{bg}}$ ,  $0.6a_{\text{bg}}$  and  $0.7a_{\text{bg}}$  for the top, middle and bottom blue curves in Figure 3.4, where  $a_{\text{bg}}$  is the background scattering length far from resonance. The effective range expansion model shows only a very small dependency on the cut-off (the three green curves are almost identical).

A similar calculation of  $\kappa^* a^{(-)}$  was done in reference [Schmidt 2012]. However, they find that the trimer binding energies for  $|a| = \infty$  get smaller compared to the single-channel zero-range value and the value of  $|a^{(-)}|$  gets larger for larger effective range. As this is exactly the opposite of the present cal-

ulation they must be using a finite range potential with a positive effective range. To obtain results for positive effective range the boundary condition with the shape parameter eq. (2.81) in the effective range expansion model is used. Indeed the opposite behaviour is obtained as seen in Figure 3.4.

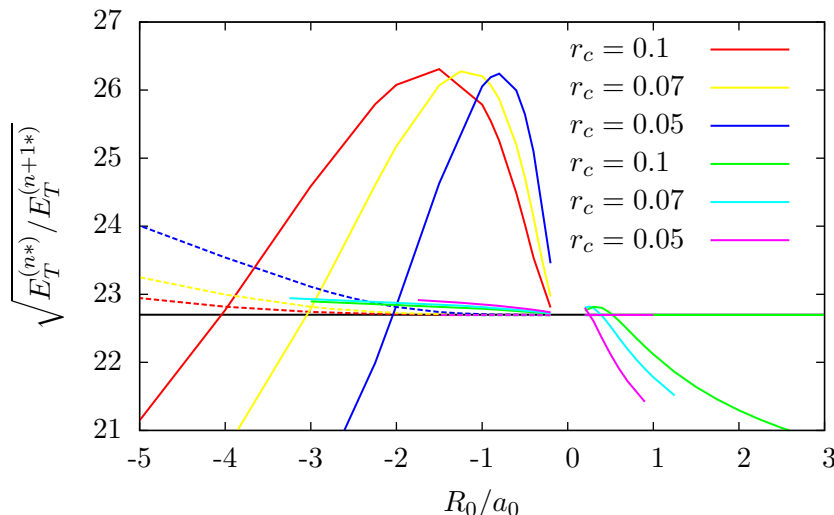


Figure 3.5: The ratio of the trimer bound state energies on resonance,  $E_T^{(n^*)}$ , as a function of the effective range for several different cut-offs. The solid lines show the ratio of energies for the first and second state, the dashed lines for the second and third state. Red, yellow and blue curves (top three in legend) are for the two-channel model while green, cyan and magenta curves (bottom three in legend) are for the effective range expansion model. The reference value is the horizontal black line which lies at 22.7, the value for the single-channel zero-range model.

In order to better understand the behaviour of the trimer energies  $E_T$  and  $a^{(-)}$ , Figure 3.5 shows the ratio of the trimer bound state energies on resonance for the two-channel and the effective range expansion models for three different cut-offs, chosen for the purpose of illustration. The most noticeable feature is the change of the Efimov scaling ratio  $E_T^{(1^*)}/E_T^{(2^*)}$  (which equals  $22.7^2 \approx 515$  in the single-channel zero-range model) between the two lowest trimer states in the two-channel model. This non-monotonous behaviour can be understood if one assumes a three-body wave function that lives at large hyper-radii,  $\rho$ . When the effective range is decreased from zero ( $|R_0|$  increases) the barrier in Figure 3.1 initially decreases the binding energy with respect to the pure single-channel zero-range model. As the effective range increases, the wave function will leak into the attractive pocket at small  $\rho$ , which will again

increase the binding energy compared to the single-channel zero-range result. This effect is strong for the ratio of the two lowest trimers but becomes weaker for the ratio of the two highest trimers. This is understandable since the least bound trimers reside at very large hyper-radii and are largely insensitive to the short-range changes in the hyper-radial potential. The effect is seen for all cut-offs, however with different absolute values.

### 3.3 Finite-range effects in the recombination rate

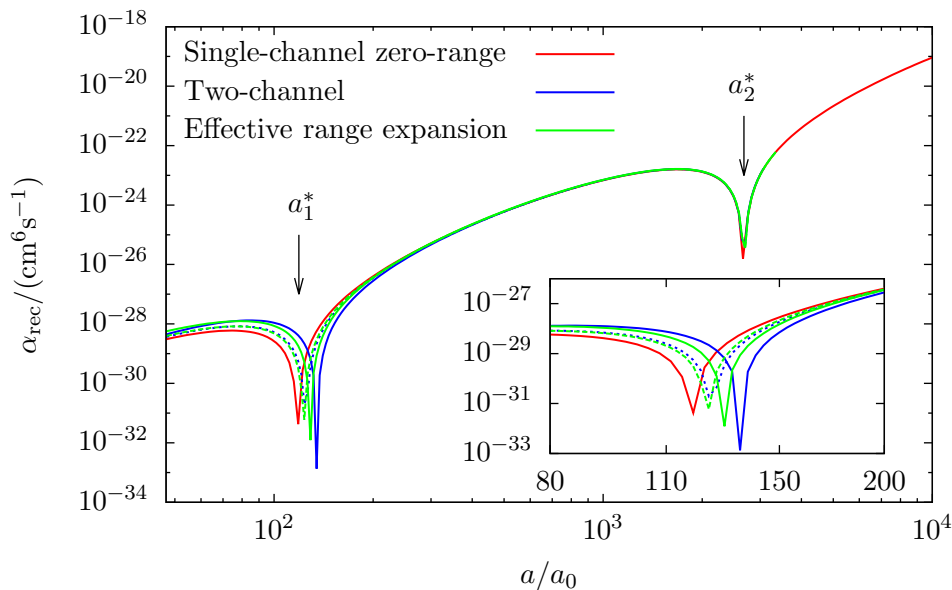


Figure 3.6: The recombination coefficient  $\alpha_{\text{rec}}$  from eq. (2.88) for the single-channel zero-range model, the effective range expansion model and the two-channel model with  $R_0 = -3a_0$  (dotted) and  $R_0 = -10a_0$  (solid). The inset shows a closer look at the minimum near  $a_1^*$ . Note that the cut-off is such that all models reproduce the minimum at  $a_2^*$ . This allows us to study the effects of the effective range at the other minimum.

We now proceed to consider three-body recombination on the positive  $a$  side of the Feshbach resonance. On this side of the resonance the recombination takes place by transition of the three particles into the channel with a bound two-body dimer with the universal binding energy proportional to  $-1/a^2$ . On the  $a < 0$  side there is no bound dimer and the decay goes directly into some strongly bound two-body state of the atom-atom potential that de-

depends on the short-range details. This latter case is investigated in chapter 5 where recombination into deep dimers is modelled using optical potentials.

The recombination coefficients into shallow dimers for different values of the effective ranges and different models are shown in Figure 3.6. The scattering length values  $a_1^*$  and  $a_2^*$  indicate locations of minima in the recombination rate. The minima are caused by the vanishing of bound trimers into the atom-dimer continuum as shown in Figure 3.3. The difference in the Efimov scale factor as compared to the single-channel zero-range model is directly related to the difference in the location where the trimer bound states vanish into this continuum. The cut-offs were chosen such that the minimum at  $a_2^*$  is the same for all models and the comparison can then be made by looking at the minimum at  $a_1^*$ . For the single-channel zero-range model, the ratio of  $a_2^*$  to  $a_1^*$  is 22.7, showing that this calculation scheme agrees with the universal result. For the other models this ratio is reduced, the minimum at  $a_1^*$  moves towards higher  $a$ . In order to make this more clear the ratio of the minima as a function of the effective range on resonance,  $R_0$ , is plotted in Figure 3.7. The two-channel and effective range expansion models give similar qualitative predictions but there are small quantitative differences. The curves cannot be extended all the way to  $R_0 = 0$  due to numerical issues, but the trends should be clear. The scale factor reduces quite drastically at large negative  $R_0$  for both models. This corresponds to narrow Feshbach resonances, where there are currently not enough experimental data to make a proper comparison.

### 3.4 Comparison to experiment

In this section a brief comparison to some of the available experimental data is presented. Generally the models fit quite well to the available data. However, the available data consists only of systems with large resonance widths and thus small effective ranges. This makes it difficult to observe range effects. Furthermore, some datasets have only a single recombination minimum wherefore no comparison with model predictions can be made.

The two-channel models are compared to the experimental data for the cold atomic gases listed in Table 3.1. The effective ranges are calculated using the formula (2.14).

In Figure 3.8 the result from the two-channel model is shown together with the experimental data for  $^{23}\text{Na}$ . The cut-off is fixed by the experimental minimum at  $a_1^* = 62a_0$ . The rather large effective range could make the finite range effect, i.e. the reduction of the scaling factor down to 15.7, clearly noticeable. However, at least one additional minimum is needed to make a

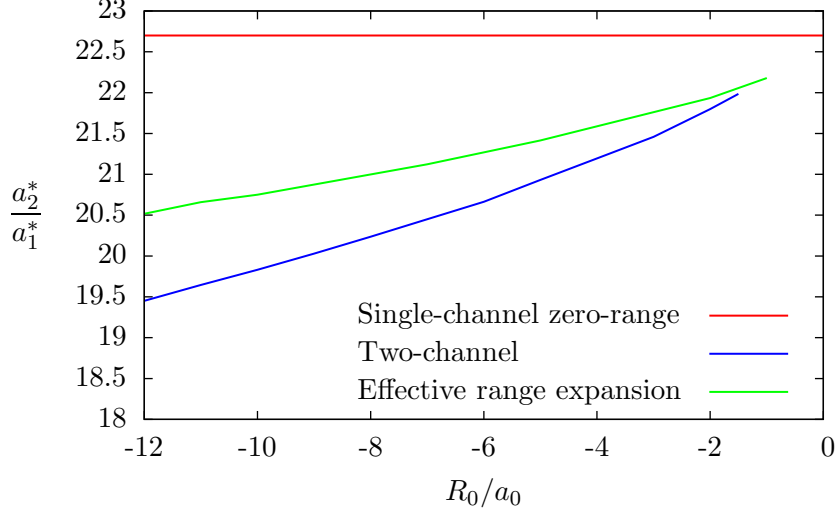


Figure 3.7: The ratio  $a_2^*/a_1^*$  for the single-channel zero-range model, the effective range expansion model and the two-channel model as a function of effective range  $R_0$ . For the single-channel zero-range model the ratio is 22.7. The scale factor is reduced when the effective range is increased, in absolute value, to become more negative.

		$B_0$ [G]	$\Delta B$ [G]	$\delta\mu$ [ $\mu_B$ ]	$a_{bg}$ [ $a_0$ ]	$R_{\text{eff}}$ [ $ a_{bg} $ ]
$^{23}\text{Na}$	[Stenger 1999]	907	0.70	3.8	63	-21
$^{133}\text{Cs}$	[Kraemer 2006]	-11.7	28.7	2.3	1720	$-1.99 \times 10^{-4}$
$^{39}\text{K}$	[Zaccanti 2009]	402.4	-52	1.5	-29	-2.02
$^7\text{Li}$	[Pollack 2009]	736.8	-192.3	1.93	-25	-3.17

Table 3.1: Experimental data for Feshbach resonances for four atomic gases.  $\mu_B$  is the Bohr magneton and  $a_0$  the Bohr radius.

proper comparison. Experimental data is not yet available in this range.

In Figure 3.9 the result from the two-channel model is shown together with the experimental data for  $^{133}\text{Cs}$ . The cut-off is fixed by the experimental minimum at  $a_1^* \approx 210a_0$ . The effective range is very small indeed and the results from the two-channel model are virtually indistinguishable from the single-channel zero-range model with the scaling factor of 22.7. The next minimum should be found at  $a_2^* \approx 4770a_0$ .

Figure 3.10 shows the recombination coefficient for  $^{39}\text{K}$ . The cut-off pa-

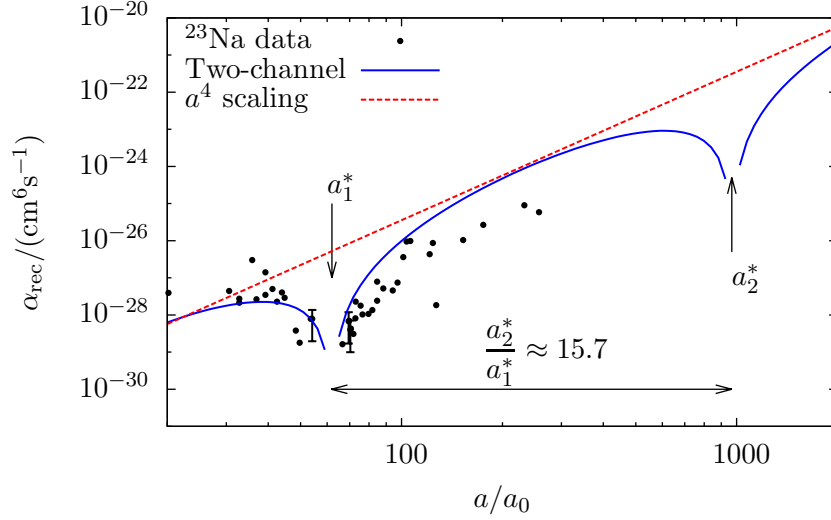


Figure 3.8: The recombination coefficient  $\alpha_{\text{rec}}$ , eq. (2.88), from the two-channel model for  $^{23}\text{Na}$  as a function of scattering length  $a$  compared with the experimental data from [Stenger 1999]. The theory predicts the next minimum to be around  $a_2^* \approx 1000a_0$ .

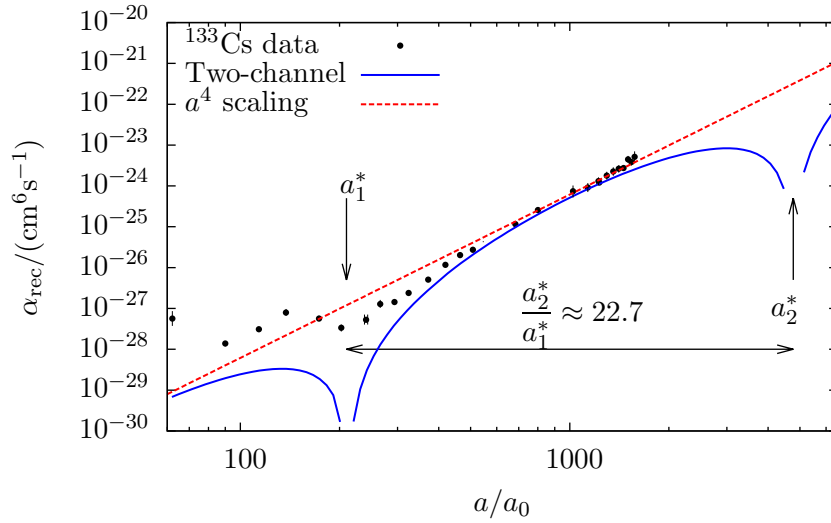


Figure 3.9: The recombination coefficient  $\alpha$ , eq. (2.88), from the two-channel model for  $^{133}\text{Cs}$  as a function of the scattering length  $a$  compared with the experimental data from [Kraemer 2006]. The theory predicts the next minimum to be around  $a_2^* \approx 4770a_0$ .

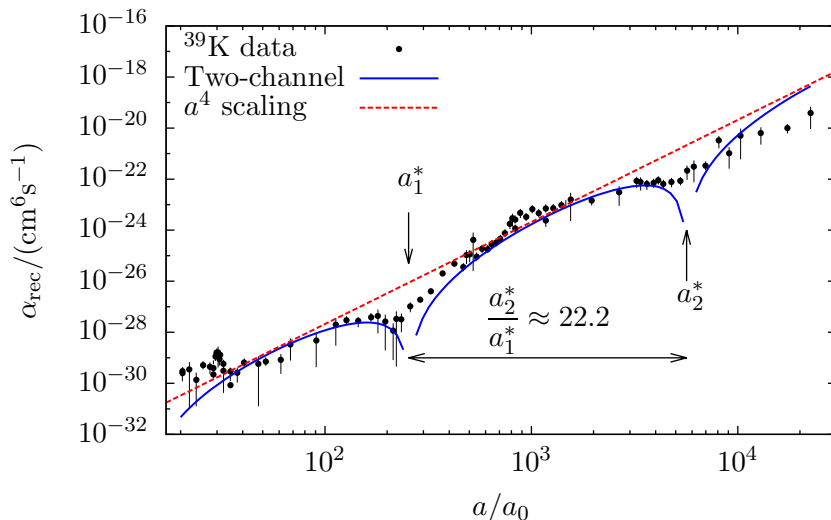


Figure 3.10: The recombination coefficient  $\alpha$ , eq. (2.88), from the two-channel model for  $^{39}\text{K}$  as a function of the scattering length  $a$  compared with the experimental data from [Zaccanti 2009]. The location of the minima are reasonably well described by the two-channel model.

parameter is chosen to fit the recombination minimum  $a_2^* = 5650 \pm 900$ . The two-channel model gives  $a_1^* = 254a_0$ , with the experimental value of  $a_1^* = (224 \pm 7)a_0$ . Overall, the two-channel model fits the data quite well. Notably the scaling is correct compared to experiment. The ratio of minima from the two-channel model is 22.2, whereas the experimental value is  $25.2 \pm 4.1$ . The result lies within the experimental uncertainty.

The recombination coefficient for  $^7\text{Li}$  is shown in Figure 3.11. The two minima are at  $a_1^* = (119 \pm 11)a_0$  and  $a_2^* = (2676 \pm 195)a_0$ . The cut-off is fixed by  $a_2^*$ , giving the two-channel prediction  $a_1^* = 125a_0$ . Again the theory describes the experimental data very well. The two-channel model ratio of minima is 21.4 while the experimental value is  $22.5 \pm 2.6$  and again the result lies within the experimental uncertainty.

### 3.5 Conclusions

In this chapter we investigate finite range effects in three-body recombination rates in cold atomic gases near Feshbach resonances as well as finite range effects in the trimer bound state energy spectrum. We use two models which in-

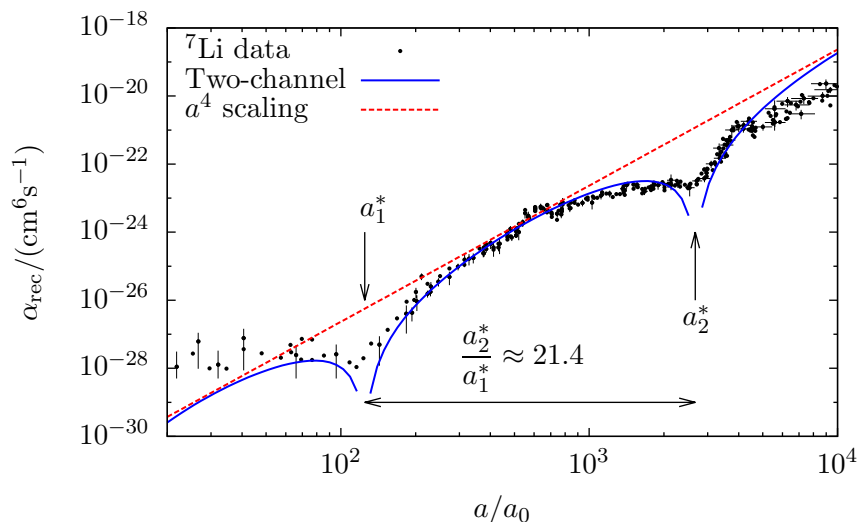


Figure 3.11: The recombination coefficient,  $\alpha$ , eq. (2.86), from the two-channel model for  ${}^7\text{Li}$  as a function of the scattering length,  $a$ , compared with the experimental data from [Pollack 2009]. Theory and experiment agree very well.

clude the finite range effects and compare their results with the single-channel zero-range model. The first model is the effective range expansion model which is a straightforward extension of the single-channel zero-range model. Here the effective range is included directly in the boundary condition on the three-body wave function following the effective range expansion of standard scattering theory. Variation of the scattering length through the Feshbach resonance is done phenomenologically as in the single-channel zero-range model. This model can also be used for positive effective range calculations. The second model is a two-channel contact interaction model which naturally includes both the finite effective range and the variation of the scattering length through the Feshbach resonance.

We show that with these well-tested two-body interaction models the three-body physics can display complicated non-monotonic behaviour as the effective range is varied. In particular, we find that the geometric scaling factor of 22.7 for equal mass particles changes when including effective range corrections, and that it can become both larger and smaller than this value depending on the magnitude and sign of the effective range.

In the current set-up this can be understood based on the functional form of the effective hyper-radial potential. On resonance where the scattering

length diverges, the lowest trimer bound state has the strongest dependency on the effective range since it lives at small hyper-radius, whereas the excited states live at much larger hyper-radii and the effective range contribution is much less profound. The adiabatic potential of the effective range expansion model is raised and lowered relative to the single-channel zero-range model potentials when the effective range is negative and positive respectively. This leads to bound states being less bound or more bound respectively. For the two-channel model the effective range is always negative which can only be achieved by using two-body potentials with an outer barrier. The hyper-radial potential reflects this fact and develops a pocket at small hyper-radii that the lowest states will eventually leak into. This feature is similar to the effective range expansion model for the case of positive effective range.

Our results demonstrate that effective range corrections within the framework of single-channel zero-range model potentials can lead to non-trivial behaviour of the trimer energies, thresholds and interference features in recombination rates. Effective range corrections are expected to be important for the case of narrow Feshbach resonances [Chin 2011]. The experimental data on Efimov states for narrow resonance systems is sparse and more measurements are needed in order to fully discriminate between different models that include finite range corrections. However, what we can conclude is that care must be taken when a particular two-body scattering model is used for the trimer states that have the largest binding energies in a universal set-up, i.e. for the lowest states that have binding energies related to the background short-range length scales. For higher lying trimers it is less important since the states are largely insensitive to the short-distance behaviour of the effective three-body potential.

## Chapter 4

# Universal Three-Body Parameter

*This chapter investigates the universal relation between the three-body parameter,  $a^{(-)}$ , and the van der Waals length,  $r_{\text{vdW}}$ . A simple two-body interaction model is used to relate the number of bound states in the two-body potential to the three-body parameter.*

---

When using zero-range potentials as described in the previous chapters, two-body variables like the scattering length and effective range are not enough to predict three-body observables without additional parameters. The additional parameter needed is known as the three-body parameter, or 3BP. In the previous chapter it manifested itself in terms of a short-range regularization cut-off,  $\rho_{\text{cut}}$ . The 3BP is more commonly given by the threshold for creation of the lowest three-body bound state on the negative  $a$  side, denoted as  $a^{(-)}$  in Figure 3.3. In the single-channel zero-range model  $\rho_{\text{cut}}$  and  $a^{(-)}$  are directly related by a simple expression. A surprising result that has turned up in later years is the fact the  $a^{(-)}$  is apparently related to the two-body van der Waals length in alkali atoms with  $|a^{(-)}|/r_{\text{vdW}} \sim 9.8$ , thus relating the 3BP to two-body physics [Berninger 2011].

In this chapter the relation between the two-body van der Waals length and the three-body parameter  $a^{(-)}$  is investigated using a simple model of the two-body potential, namely a pure van der Waals  $1/r^6$  attraction with a hard-core cut-off. The number of bound states in such a potential is easily derived which is used to relate the 3BP to the number of bound states in the two-body potential. Reasonable agreement with experimental data is found. Other two-body potentials like the Lennard-Jones and Morse potentials give similar

predictions and thus the exact form of the two-body potential is not of any qualitative importance. Furthermore we investigate how the effective range affects the value 9.8. Results of this chapter are also found in [Sørensen 2012].

This chapter will utilize the so-called resonance strength  $s_{\text{res}}$  given by [Chin 2010]

$$s_{\text{res}} \equiv \frac{r_{\text{vdW}}}{|R_0|}, \quad (4.1)$$

where  $r_{\text{vdW}}$  is the van der Waals length which is introduced in the next section. Unfortunately all experimental data lie in the regime of broad resonances,  $s_{\text{res}} \gg 1$ , and corresponding short effective ranges, and range effects are thus hard to see in these systems.

## 4.1 Trimer threshold value revisited

In Figure 3.3 of the previous chapter the threshold value  $a^{(-)}$  for appearance of the lowest Efimov trimer bound state for negative scattering lengths is shown for the zero-range model and the two effective range models. In this section the dependency of  $a^{(-)}$  on the cut-off and effective range is investigated. The deviation between the single-channel zero-range and the two-channel curve<sup>1</sup> can be split into two parts. First, the trimer bound state energy  $E_T$  on resonance is lower for the two effective range models compared to the single-channel zero-range value given that the states with  $n = 2$  have been fixed to the same energy for all models. Reducing the cut-off in the single-channel zero-range model increases the binding energy on resonance as per eq. (2.65) and Ref. [Efimov 1971], resulting in a decreased value of  $|a^{(-)}|$  according to Figure 3.3. This relation between  $\rho_{\text{cut}}$  and  $a^{(-)}$  is linear and we find it numerically to be

$$a^{(-)} = -\delta\rho_{\text{cut}}, \quad \delta \approx 31.756, \quad (4.2)$$

for the single-channel zero-range model. A linear relation is the only possibility since  $\rho_{\text{cut}}$  is the sole input length scale.

For the two-channel model  $|a^{(-)}|$  is further reduced when the effective range is increased, i.e.  $|R|$  increases. A simple linear relation as the one above is, however, not obtainable as the dependency is more intricate.

A systematic study of the influence of both  $\rho_{\text{cut}}$  and  $R_0$  (in terms of  $s_{\text{res}}$ ) is shown in Figure 4.1. The values of  $\rho_{\text{cut}}/r_{\text{vdW}}$  from top to bottom are 1.20, 0.82, 0.66, 0.58, 0.51, 0.47, 0.42, 0.40, and 0.38. They correspond to  $n = 0$  to

---

<sup>1</sup>The effective range expansion model is not considered in this discussion, but similar conclusions would follow if it had been.

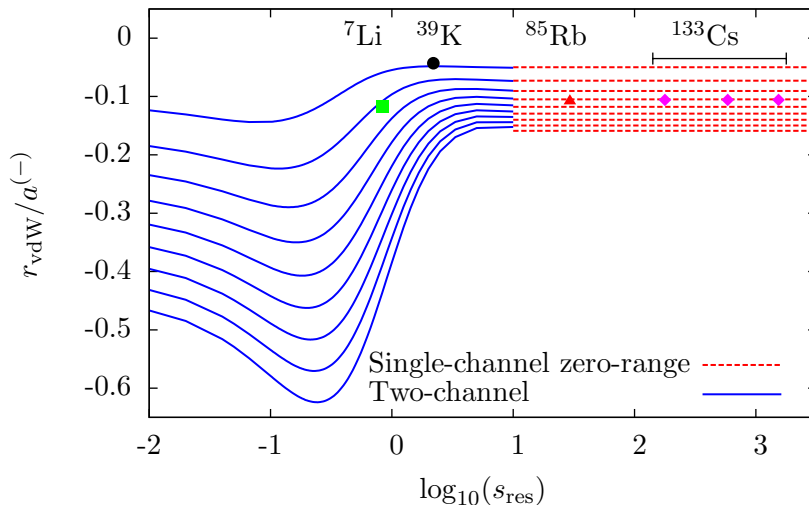


Figure 4.1: The threshold scattering length,  $a^{(-)}$ , at which the lowest universal Efimov trimer merges with the three-atom continuum, for negative  $a$ , plotted against the strength,  $s_{\text{res}}$ , of the Feshbach resonance. The right-hand side corresponds to broad resonances. The different curves show results with different three-body parameters,  $\rho_{\text{cut}}$ , in units of the atomic van der Waals length,  $r_{\text{vdW}}$ . The values of  $\rho_{\text{cut}}$  decrease from top to bottom from 1.20 down to 0.38 with the best fit value for broad resonances being 0.58. Experimental values are for  ${}^{133}\text{Cs}$  [Kraemer 2006, Berninger 2011],  ${}^7\text{Li}$  [Pollack 2009],  ${}^{39}\text{K}$  [Zaccanti 2009] and  ${}^{85}\text{Rb}$  [Wild 2012].

8 in eq. (4.6) below. Both models agree for  $s_{\text{res}} \gg 1$ . The two-channel model results are shown only in the region where they deviate from the single-channel zero-range results. To reproduce the experimental data for  $s_{\text{res}} \gg 1$ , the cut-off value of  $\rho_{\text{cut}}/r_{\text{vdW}} = 0.58$  provides the best fit. However, for small  $s_{\text{res}}$ , the same cut-off does not reproduce the used data point coming from  ${}^7\text{Li}$  [Pollack 2009] (other measurements have slightly smaller  $|a^{(-)}|$  [Gross 2009, Gross 2010], which increases the ratio  $|r_{\text{vdW}}/a^{(-)}|$  by about 5%). The increase toward the  ${}^{39}\text{K}$  data point at small  $s_{\text{res}}$  cannot be accommodated for the same  $\rho_{\text{cut}}$ .

The non-monotonic behaviour observed is exactly the same as for the trimer bound state energies as discussed near Figure 3.4 and Figure 3.5. When the effective range becomes more negative the trimer binding energy decreases (becomes less negative) with a corresponding increase in  $|a^{(-)}|$ . Further increasing the effective range eventually increases the binding energy and  $|a^{(-)}|$  decreases yet again.

The opposite behaviour was found in [Schmidt 2012]. However, their approach seems to rely on finite range potentials with a positive effective range, thus the opposite direction of change is no surprise. Feshbach resonances usually have negative effective ranges [Chin 2010], so the here presented method is preferable.

## 4.2 Two-body potentials

The zero-range models do not carry any inherent information about the van der Waals length. However, the three-body parameter or cut-off,  $\rho_{\text{cut}}$ , has a physical meaning as it provides a hard-core repulsion in the hyper-spherical three-body coordinates. To connect the formalism to the experimental data, it is therefore necessary to find a relation between the two-body atomic physics and,  $\rho_{\text{cut}}$ . In this section a relation between the two-body cut-off,  $r_c$ , and the van der Waals length  $r_{\text{vdW}}$  is obtained using a simple two-body van der Waals potential. In the next sections the two and three-body cut-offs are related and finally the van der Waals length is related to  $a^{(-)}$ .

	Unit	${}^7\text{Li}$	${}^{39}\text{K}$	${}^{85}\text{Rb}$	${}^{133}\text{Cs}$
$C_6$	$a_0^6 E_h$	1393	3897	4691	6851
$r_{\text{vdW}}$	$a_0$	65	129	164	202

Table 4.1: The Van der Waals coefficient,  $C_6$ , and length,  $r_{\text{vdW}}$ , for some alkali atoms.  $a_0$  is the Bohr radius and  $E_h \approx 27.2$  eV is the Hartree unit of energy.

Interactions between neutral atoms are often described using a potential with a long-range tail of the form  $C_6/r^6$  where the coefficient  $C_6$  is known as the van der Waals coefficient [Pethick 2002]. This long range behaviour originates from small fluctuations in the electron clouds causing mutual polarization of the atoms. The resulting effect is known as van der Waals forces<sup>2</sup>. From the  $C_6$  coefficient the van der Waals length can be constructed

$$r_{\text{vdW}} = \left( \frac{mC_6}{\hbar^2} \right)^{1/4}, \quad (4.3)$$

where  $m$  is the mass of the atoms. The coefficient  $C_6$  can be found by chemical calculations [Pethick 2002]. A list of alkali atoms and their corresponding van der Waals coefficients are given in Table 4.1.

<sup>2</sup>Which quite ingeniously the gecko has utilized in its ability to climb glass surfaces.

Since the  $1/r^6$  behaviour cannot continue to  $r = 0$ , a cut-off is applied at some small distance  $r_c$ . This acts like a strong short-range repulsion which is also seen in physical potentials. The potential is

$$V(r) = \begin{cases} \infty & \text{for } r < r_c, \\ -\frac{C_6}{r^6} = -\epsilon_0 \left(\frac{r_c}{r}\right)^6 & \text{for } r \geq r_c, \end{cases} \quad (4.4)$$

where  $\epsilon_0 = C_6/r_c^6$  is the minimal value of the potential. For graphical illustration this potential, along with the Morse and Lennard-Jones potentials discussed later, is plotted in Figure 4.2 such that the minimal value  $\epsilon_0$  and minimum location  $r_{\min}$  coincide for all models. For eq. (4.4) we have of course  $r_{\min} = r_c$ .

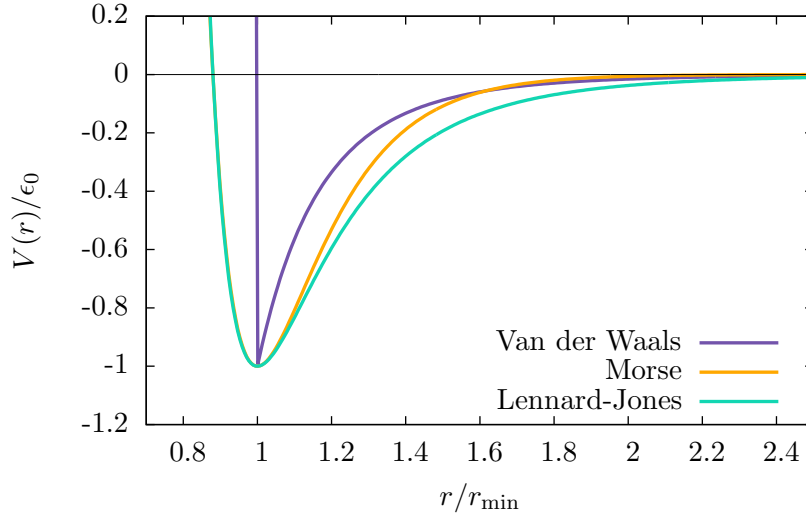


Figure 4.2: A small assortment of two-body neutral atom potentials from eq. (4.4), eq. (4.10) and eq. (4.11).  $\epsilon_0$  indicates the minimal value of the potential and  $r_{\min}$  is the location of the minimum. For the van der Waals potential in eq. (4.4)  $r_{\min} = r_c$ .

The scattering length of the potential in eq. (4.4) can be found analytically by rewriting the corresponding Schrödinger equation to the Bessel equation of order  $1/4$ . Details can be found in [Pethick 2002] and will not be reproduced here. The result for the scattering length is (see also [Gribakin 1993, Gribakin 1999])

$$a = r_{\text{vdW}} \frac{2\pi}{\Gamma(\frac{1}{4})^2} [1 - \tan(\Phi - 3\pi/8)] \approx 0.478 r_{\text{vdW}} [1 - \tan(\Phi - 3\pi/8)], \quad (4.5)$$

where  $\Phi = r_{\text{vdW}}^2/2r_c^2$ . Whenever the scattering length diverges the potential is able to support yet another bound state. Thus counting the number of divergences in  $a$  as a function of  $\Phi$  yields the number of bound states. The scattering length  $a$  diverges when  $\Phi - \frac{3\pi}{8} = (n + \frac{1}{2})\pi$  for integer  $n$ , thus the number of  $s$ -wave bound states in the potential is

$$n = \left[ \frac{1}{2\pi} \left( \frac{r_{\text{vdW}}}{r_c} \right)^2 - \frac{7}{8} \right], \quad (4.6)$$

where the "bracket" indicates round off to highest nearby integer.  $s$ -wave states are all we are interested in as discussed in chapter 2.

#### 4.2.1 Relating two- and three-body cut-offs

To relate the van der Waals length, which is a two-body parameter, to the 3BP,  $a^{(-)}$ , a simple link between the two- and three-body cut-offs has to be established. We do this by presenting this a simple geometric interpretation.

The atom-atom two-body potential has a steep repulsive inner core which is here modelled by a hard inner wall, as in eq. (4.4). In this case the boundary condition is simply that the two-body wave function must be zero at  $r_c$  and below. This must then be translated into the three-body problem where it implies that the total wave function must be zero whenever any of the relative distances between two of the three atoms is less than or equal to  $r_c$ . Any penetration of the wave function into the wall would cost an infinite amount of energy and is thus forbidden.

A neat and elegant way to obtain a cut-off condition on  $\rho$  is the following. For three equal mass particles the hyper-radius from eq. (2.36) can be written as

$$\rho^2 = \frac{1}{3} \sum_{i < k} (\mathbf{r}_i - \mathbf{r}_k)^2 = \frac{1}{2} \mathbf{r}_{12}^2 + \frac{2}{3} \mathbf{r}_{12,3}^2 = \mathbf{x}^2 + \mathbf{y}^2, \quad (4.7)$$

where  $\mathbf{r}_{12} = \mathbf{r}_1 - \mathbf{r}_2 = \sqrt{2}\mathbf{x}$  and  $\mathbf{r}_{12,3} = \mathbf{r}_3 - (\mathbf{r}_1 + \mathbf{r}_2)/2 = \sqrt{\frac{3}{2}}\mathbf{y}$  are respectively the relative vector from particles 2 to 1 and the relative vector from the center of mass of particle 1 and particle 2 to particle 3.

For the close packed triangular configuration in Figure 4.3a, eq. (4.7) yields  $\rho = r_c$ . A linear configuration (as in Figure 4.3b but not exactly the one shown), can however, have  $\mathbf{y} = 0$  and  $|\mathbf{x}| = r_c$  wherefore  $|\mathbf{r}_{12}| = \sqrt{2}r_c$ , which is allowed. However, particle 3 lies in between particles 1 and 2, overlapping with the hardcore cut-off, which is not allowed.

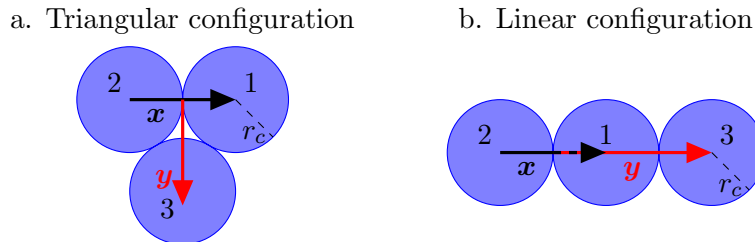


Figure 4.3: Schematic drawing of the triangular, a, and linear, b, configurations for an equal mass three-body system.  $\mathbf{x}$  and  $\mathbf{y}$  indicate the Jacobi coordinates.

Consider instead the linear configuration with  $r_{12} = r_c$  and impose the requirement  $r_{23} \geq r_c$ , where  $\mathbf{r}_{23} = \mathbf{r}_2 - \mathbf{r}_3$ . Since  $\mathbf{r}_{12,3} = \mathbf{r}_{23} + \mathbf{r}_{12}/2$  we get

$$\rho^2 \geq r_c^2 \left( \frac{1}{2} + \frac{2}{3} \left[ 1 + \frac{1}{2} \right]^2 \right) = 2r_c^2. \quad (4.8)$$

The condition  $\rho > \sqrt{2}r_c$  ensures that both the triangular and the linear configurations are outside of the hard-core regions. Since these configurations are extremal, the condition implies that no regions with infinite potential are reached by the hyper-radial three-body wave function.

The rigorous formal argument for the validity of the relation  $\rho_{\text{cut}} = \sqrt{2}r_c$  using the hyper-spherical approach can be found in Ref. [Jensen 1997], where the relation is derived using a square well potential. The asymptotic region is precisely  $\rho > \sqrt{2}r_c$  as found above. Here a hard-core potential was assumed for simplicity which gives the factor of  $\sqrt{2}$ . For a real atom-atom potential, the hard-core is slightly softer (typically of the  $1/r^{10}$  as in eq. (4.10) below) which may lead to a minor change in the factor  $\sqrt{2}$ .

#### 4.2.2 Relating $a^{(-)}$ to $r_{\text{vdW}}$

Combining the results of the previous sections, namely eq. (4.2), eq. (4.6) and eq. (4.8) is a trivial matter but nevertheless yields a very important result

$$\frac{a^{(-)}}{r_{\text{vdW}}} = - \frac{2\delta}{\sqrt{\left(n + \frac{7}{8}\right) \pi}}, \quad (4.9)$$

where  $n$  is the number of bound states. This semi-analytical expression for the threshold in terms of the number of bound states very elegantly relates the two-body van der Waals length,  $r_{\text{vdW}}$ , with the three-body parameter,  $a^{(-)}$ .

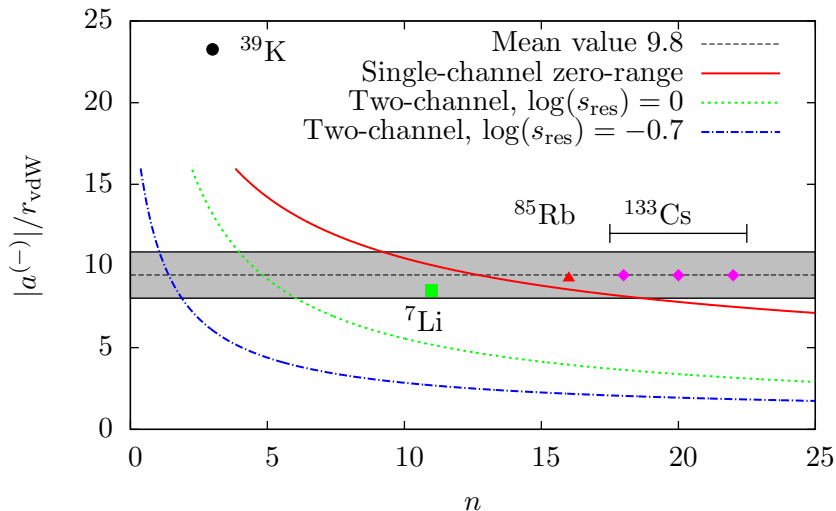


Figure 4.4: Semi-analytic results for the three-body parameter  $a^{(-)}$  plotted against the number of bound states in the two-body van der Waals plus hard-core potential, eq. (4.4). The horizontal position of the experimental data is arbitrary. The grey band indicates a 15% margin around the value  $\sim 9.8$ .

The relation in eq. (4.9) is plotted in Figure 4.4 along with the experimental data and the numerical results obtained from the two-channel model for different values of  $s_{\text{res}}$ . For the two-channel model  $\delta$  varies with effective range. The single-channel zero-range model is consistent with the data for  $n \sim 10 - 20$  and reproduces the universal ratio of Ref. [Chin 2011] for  $n = 13$ . This is also consistent with the findings of Ref. [Wang 2012], although their results only goes to  $n = 10$ . The  $n^{-1/2}$  behaviour seems to also appear in Ref. [Wang 2012], where an extension to higher  $n$  could confirm this prediction.

The results from the two-channel model with small  $s_{\text{res}}$ , i.e. narrow resonances and large effective ranges, indicate that  $|a^{(-)}|$  drops faster with  $n$  (blue curve in Figure 4.4) than for  $s_{\text{res}} \gg 1$  (red curve in Figure 4.4). This is seen in the experimental data for  ${}^7\text{Li}$  which is slightly below the  ${}^{85}\text{Rb}$  and  ${}^{133}\text{Cs}$  points, but the model overestimates this trend. More results on narrow resonance systems are required to address the question of effective range corrections.

### 4.3 Number of dimer bound states

The other potentials in Figure 4.2 are the more realistic Lennard-Jones (LJ) potential

$$V_{\text{LJ}}(r) = \frac{C_{10}}{r^{10}} - \frac{C_6}{r^6} = \epsilon_0 \left[ \frac{3}{2} \left( \frac{r_{\text{min}}}{r} \right)^{10} - \frac{5}{2} \left( \frac{r_{\text{min}}}{r} \right)^6 \right], \quad (4.10)$$

(sometimes also written with the power 12 in the first term, in which case the rightmost expression would of course also have to be changed) and the Morse (M) potential, given by

$$V_{\text{M}}(r) = \epsilon_0 \left[ e^{-2\alpha(r-r_{\text{min}})} - 2e^{-\alpha(r-r_{\text{min}})} \right], \quad (4.11)$$

where  $r_{\text{min}}$  is the location of the potential minimum. They have a smoother behaviour at the inner barriers. This implies only minor quantitative corrections. More importantly the number of bound states in the two-body alkali dimer potential need to be addressed.

The number of  $s$ -wave bound states in the Lennard-Jones and Morse potentials can be estimated analytically and yields [Mahan 1969]

$$n_{\text{LJ}} = \left\lceil 0.361\sqrt{\beta} - \frac{5}{8} \right\rceil, \quad (4.12)$$

and

$$n_{\text{M}} = \left\lceil 0.245\sqrt{\beta} - \frac{1}{2} \right\rceil, \quad (4.13)$$

where  $\beta = \frac{mr_{\text{min}}^2\epsilon_0}{2\hbar^2}$  with  $r_{\text{min}}$  the radius at which the potential takes its minimal value,  $\epsilon_0$ . For comparison, the expression in eq. (4.6) can be written  $n = 0.225\sqrt{\beta} - \frac{7}{8}$ , with  $r_{\text{min}} \leftrightarrow r_c$  such that  $\beta = \frac{r_{\text{vdW}}^4}{2r_c^4}$ . The similarity of these expressions makes it clear that the behaviour seen in Figure 4.4 is generic and does not depend on the choice of two-body potential. The difference in constant in front of  $\sqrt{\beta}$  provides only a minor quantitative change in the numbers.

An important question, however, remains about the number of bound states,  $n$ , in a real alkali dimer system. This is estimated using the bond lengths  $r_{\text{min}}$  and dissociation energies  $\epsilon_0$  of Ref. [Igel-Mann 1986] listed in Table 4.2 where also the estimates for  $n$  are listed. The estimated number of bound states is outside the axis in Figure 4.4 and also much beyond the results shown in Ref. [Wang 2012]. The agreement with theory at a rather limited number of bound states ( $n \sim 10 - 20$ ) is then quite surprising.

	Unit	Li	K	Rb	Cs
$r_{\min}$	Å	2.67	3.92	4.18	4.65
$\epsilon_0$	eV	1.06	0.52	0.49	0.45
$n_{\text{vdW}}$		18	43	67	88
$n_{\text{LJ}}$		29	70	108	142
$n_{\text{M}}$		20	47	73	96

Table 4.2: The two-body inter-atomic potential parameters for some alkali atoms. The first two rows tabulate bond lengths and strengths [Igel-Mann 1986]. The last three rows tabulate the number of bound  $s$ -wave states in the van der Waals plus cut-off, Lennard-Jones and Morse potentials using the respective bond lengths and strengths.

A number of important observations can be made. First, the decrease of  $|a^{(-)}|$  with  $n$  is weak, and a shift of the length scale in Figure 4.4 would therefore place the single-channel zero-range model within the experimental range for larger  $n$  and it would stay within the 15% deviation from the mean for a larger interval (since the slope at larger  $n$  decreases even faster). Second, the experimental data might indicate that only a certain number of bound states play an active role. Equivalently, even if the two-body potential is very deep, only the upper part of the two-body potential and the bound states closest to threshold set the scale of the three-body problem. This appears to be very reasonable since we are considering universal Efimov trimers here and not strongly bound three-body states. Third, the case of small  $s_{\text{res}}$  has  $|a^{(-)}| \propto n^{-r}$  with  $r > 1/2$  as seen in Figure 4.4. This implies that narrow resonance systems should be even less sensitive to  $n$  beyond a certain lower limit.

A quantitative argument for the lack of sensitivity to the many deep bound states in the van der Waals potential is as follows: The number of bound states in the potential  $V(r)$  with energies larger than  $E$ , can be estimated using the WKB approximation

$$\int_{r_i}^{r_o} \sqrt{E - V(r)} dr = \pi \hbar \left( n(E) - \frac{1}{4} \right), \quad (4.14)$$

where  $r_i$  and  $r_o$  are the inner and outer classical turning points such that  $E = V(r_i) = V(r_o)$ . For  $E = 0$  this yields the total number of bound states  $n_{\text{total}}$  (given by  $n$  in Table 4.2), essentially by counting the total number of oscillations of the zero-energy wave function. For finite energy,  $E < 0$ , the integral is not analytically solvable when  $V(r)$  is the van der Waals po-

tential from eq. (4.4) (in which case the inner turning point is the cut-off  $r_c$ ). However, we find numerically that the number of bound states with the energy in the interval  $[E, 0]$ , to a good approximation, is given by  $n(E) = n_{\text{total}}(|E|/E_{\text{vdW}})^{1/3}$  for  $-E_{\text{vdW}} < E < 0$ , where  $E_{\text{vdW}} = \hbar^2/mr_{\text{vdW}}^2$  and the energy,  $E$ , is now measured from 0 downwards. For the  $s_{\text{res}} \gg 1$  cases ( $^{85}\text{Rb}$  and  $^{133}\text{Cs}$ ),  $n(E)/n_{\text{total}} \sim 0.10 - 0.20$  which implies  $|E|/E_{\text{vdW}} \sim 0.001 - 0.01$ . Numerically we find a three-body energy on resonance  $E_T = 0.006E_{\text{vdW}}$  (using  $\rho_{\text{cut}} = 0.58r_{\text{vdW}}$ ). However, universality relates  $E_T = \hbar^2\kappa^2/m$  and  $a^{(-)}\kappa \sim -1.51$  [Efimov 1971, Braaten 2006, Gogolin 2008] as noted in the previous chapter. The energy scale at the continuum threshold is given by  $a^{(-)}$  through  $|E| \sim \hbar^2/m(a^{(-)})^2 = 0.003E_{\text{vdW}}$ , in agreement with the interval above. In the case of  $^7\text{Li}$ ,  $E_T$  is similar but this is compensated by a smaller  $n_{\text{total}}$  so this case can also be explained. For the heavier alkali atoms at a narrow resonance, our two-channel results predict a smaller  $|a^{(-)}|/r_{\text{vdW}}$  than 9.8, which is a good experimental test of our theory.

## 4.4 Conclusions

In this chapter the three-body cut-off was expressed as the three-body parameter  $a^{(-)}$  in the single-channel zero-range model via a simple linear relation. Using this relation the number of bound states in a semi-realistic van der Waals potential was related to the ratio of the three-body parameter and the van der Waals length. This ratio has the universal value of  $\sim 9.8$  across several different atomic species. A comparison between the experimental data and the here presented model yielded reasonable agreement. The case of narrow Feshbach resonances, corresponding to small strengths  $s_{\text{res}}$  and large effective ranges, was investigated using the two-channel model. Our model predicts that the universal ratio 9.8 should decrease when the effective range increases (becomes more negative).



## Chapter 5

# Recombination for negative scattering lengths

*This chapter investigates recombination for negative scattering lengths using optical potentials to emulate the presence of deep dimers in the two-body potentials. Additionally, the effects of finite temperature are included.*

---

In this chapter the recombination rate is investigated for negative scattering lengths,  $a$ , as presented in [Sørensen 2013d]. The physical method by which particles recombine is different than for positive scattering lengths as there are no weakly bound states for negative  $a$ . The particles must recombine into deeply bound states in the two-body potentials. This regime is not immediately available using zero-range models. We will therefore emulate the existence of deeply bound states by letting the three-body potential have a complex value in a restricted region of hyper-space when all three particles are close to one another. The imaginary value of the potential acts as a probability sink that particles can disappear into. The method reproduces experimental data quite well. Additionally, we investigate the effects of finite temperature in the systems which follows naturally from the method used to describe the recombination. Universal scaling of the form  $\alpha_{\text{rec}} = C(a)a^4$  (which is still valid for negative  $a$ , but with a different form for the  $C(a)$  coefficient) is obtained only for sufficiently low temperatures. This is known as the unitarity limit [D’Incao 2004].

## 5.1 The optical model

The hidden crossing method of calculating the recombination coefficient for positive scattering lengths relies on going from one adiabatic channel to another via a path in the complex  $\rho$ -plane. Therefore, it cannot be used for negative  $a$  since recombination must go into deeply bound dimers, which are not in scope of the zero-range models.

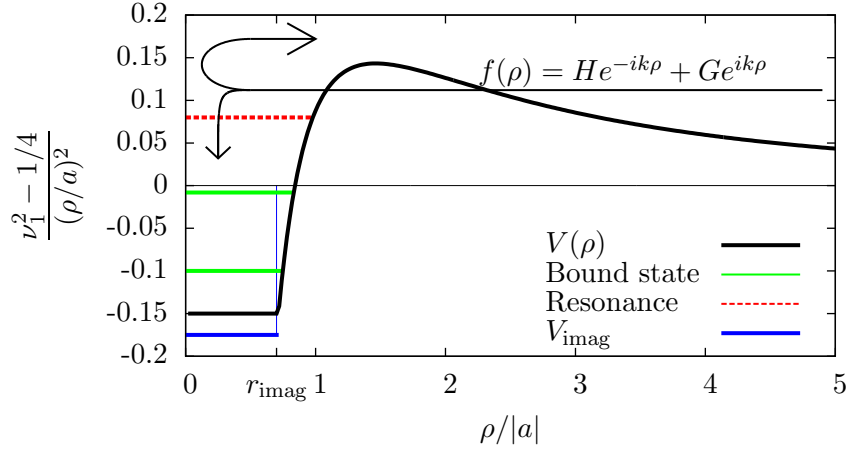


Figure 5.1: The three-body radial potential for negative scattering length,  $a$ , as a function of the hyper-radius,  $\rho$ . The  $r_{\text{imag}}$  used in calculations is much smaller than illustrated. The potential drops as  $1/\rho^2$  at large distances, diverges as  $-1/\rho^2$  for small distances (for  $\rho > r_{\text{imag}}$ ) and has a constant (complex) value  $V_{\text{imag}}$  for  $\rho < r_{\text{imag}}$ . The split arrow indicates that the wave function,  $f(\rho)$ , is both reflected and absorbed through the barrier and via the complex potential. The green full lines illustrate bound states in the potential while the red dotted line indicates a resonance.

Instead we solve the differential equation eq. (2.42). The transition amplitude is estimated using only the lowest adiabatic channel,  $n = 1$ , schematically shown in Figure 5.1. The potential has a barrier that the wave function must tunnel through. The barrier maximum is at  $\rho \approx 1.46|a|$  with a maximum value of  $0.143\hbar^2/ma^2$ . The potential furthermore crosses 0 at  $\rho \approx 0.84|a|$  which is found by setting  $\nu = 1/2$  in eq. (2.55).

At large hyper-radii we decompose the wave function into an incoming and an outgoing free wave  $f(\rho) = He^{-ik\rho} + Ge^{ik\rho}$  where  $k^2 = 2mE/\hbar^2$  and  $H$  and  $G$  are parameters that depend on energy. The transition amplitude of inelastic scattering is the ratio of amplitudes for the outgoing,  $G$ , to incoming,  $H$ , components, thus the probability of recombination is  $P(k) = 1 - |G/H|^2$ .

For a one-dimensional purely real potential this would yield  $P = 0$  identically due to conservation of probability. Therefore, a constant imaginary value, of magnitude  $|V_{\text{imag}}|$ , is added to the potential for distances smaller than the value  $r_{\text{imag}}$ . In this region the real part of the potential is also held constant at  $V(\rho < r_{\text{imag}}) = V(r_{\text{imag}})$ . The boundary condition is correspondingly  $f(0) = 0$ . This is in stark contrast to the previous regularization cut-off method where the potential is set to infinity for small  $\rho$ -values.

The parameters  $r_{\text{imag}}$  and  $V_{\text{imag}}$  are chosen to fit the experimental data by using the resonance location to determine  $r_{\text{imag}}$  and the resonance shape (or rather width) to determine  $V_{\text{imag}}$ . Both parameters are short range parameters reflecting that recombination requires all three particles to be close to one another for the recombination to occur. These parameters describe the short-range physics and are a way of including the deeply bound states, that are otherwise unreachable using zero-range models.

## 5.2 The recombination coefficient

The loss of probability due to the complex potential is quantified using a complex phase shift,  $\theta + i\gamma$ , between the incoming and outgoing waves

$$G = e^{2i(\theta+i\gamma)} H . \quad (5.1)$$

The recombination probability is then  $P(k) = 1 - e^{-4\gamma}$  where  $\gamma$ , which depends on energy, parametrizes the recombination. The recombination coefficient,  $\alpha_{\text{rec}}$ , is obtained using eq. (2.88)

$$\alpha_{\text{rec}}(a, E) = 4(2\pi)^2 3\sqrt{3} \frac{\hbar^5}{m^3} \frac{1 - e^{-4\gamma}}{E^2} , \quad (5.2)$$

where the wave number,  $k$ , has been replaced by the energy,  $E$ , for convenience in the following discussion. At energies well below the barrier height the complex phase shift,  $\gamma$ , is proportional to  $E^2$  and the limit  $E \rightarrow 0$  can be safely taken (see appendix B for details).

When the energy,  $E$ , of the incoming wave corresponds to the energy,  $E_0$ , of a resonance state behind the barrier, the tunnelling rate is greatly enhanced due to constructive interference [Sakurai 1994]. This means that there is an increased probability to reach the imaginary potential where absorption occurs, correspondingly the recombination rate has a resonant peak. At such a resonance the real part of the phase shift,  $\theta$ , has an abrupt change in  $\pi$ , indicating the presence of a resonance [Sakurai 1994]. When the energy of the incoming wave is fixed the only way to obtain resonant absorption is by

changing the resonant state energy  $E_0$ , which is done by changing the scattering length  $a$ . For certain values of  $a$ , dubbed  $a_i^{(-)}$ , the resonance energy  $E_0$  lies at 0. This corresponds exactly to the threshold value for creating a bound trimer as discussed in the previous chapter. When the energy,  $E$ , is very low it is at  $a^{(-)}$  that the recombination rate spectrum has resonant peaks.

This picture of resonances leads us to an expression for the recombination coefficient for finite energy parametrized by the Breit-Wigner distribution

$$\alpha_{\text{rec}}(a, E) = 4(2\pi)^2 3\sqrt{3} \frac{\hbar^5}{m^3} \frac{K}{[E - E_0(a)]^2 + \frac{1}{4}\Gamma^2(a)}, \quad (5.3)$$

where the numerical factor is chosen for easy comparison to eq. (5.2). This expression exhibits the physical interpretation of tunnelling through the barrier and subsequently subject to absorption and reflection at short distance. The dimensionless constant  $K$  depends only on the imaginary potential. It is worth noting that the width  $\Gamma$  cannot solely be related to the lifetime of the resonance due to the barrier but also has a contribution from decay due to the complex potential. When the barrier height is negligible compared to the energy,  $E \gg E_0, E \gg \Gamma$ , all resonance features are lost. In the opposite limit of small energy an upper limit for the recombination coefficient is obtained. This is known as the unitarity limit [D’Incao 2004].

The next step in the parametrization is to find  $K$ ,  $E_0$ , and  $\Gamma$ . The choice of the numerical factor in eq. (5.3) immediately gives the high-energy limit,  $K \rightarrow 1 - \exp(-4\gamma)$ , where  $E$  has to be large compared to the other terms in the denominator of eq. (5.3). Numerically we find that the peaks,  $a_i^{(-)}$ , in the recombination coefficient follow nicely the Efimov scaling relations and that the overall  $a^4$  tendency is obeyed. This leads to the parametrization of  $\Gamma$  and  $E_0$  as

$$\Gamma^2(a) \frac{m^2 a^4}{\hbar^4} = A \sin^2 \left[ s_0 \ln \left( \frac{a}{a^{(-)}} \right) \right] + \delta, \quad (5.4)$$

$$E_0(a) \frac{m a^2}{\hbar^2} = B \sin \left[ s_0 \ln \left( \frac{a}{a^{(-)}} \right) \right] + \beta, \quad (5.5)$$

where  $A, B, \beta$  and  $\delta$  are constants that depend weakly on the imaginary potential. This form ensures that both the  $a^4$ -rule and the Efimov scaling are obeyed with periodic 22.7 peak-recurrence in  $\alpha_{\text{rec}}$ . The parameters, that are obtained by fitting eq. (5.3), eq. (5.4) and eq. (5.5) to the results from eq. (5.2) at some finite energy, are plotted in Figure 5.2 as functions of the imaginary strength,  $|V_{\text{imag}}| m r_{\text{imag}}^2 / \hbar^2$ . The coefficient  $B$  is much smaller than  $A$  meaning that  $E_0$  is of little significance compared to  $\Gamma$ . The variables  $\beta$  and  $\delta$  are

also insignificant, since they are at least a factor of 10 smaller than  $A$  and  $B$ . The low-energy dependence of  $\alpha_{\text{rec}}$  on energy is thus primarily determined by  $K/\Gamma^2$ . The variations of the imaginary strength between 10 and 120 amount to only about 10 – 20 %, except for  $K$  which decreases by about a factor of 2. As will be seen below, the experiments constrain the imaginary strength variation interval to  $\sim 10 - 70$ .

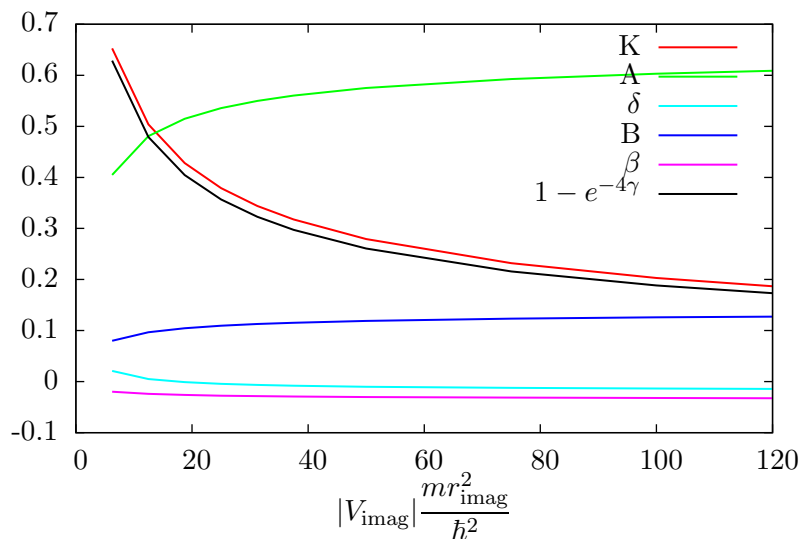


Figure 5.2: The parameters of eq. (5.4) and eq. (5.5) as functions of the strength of the imaginary square-well potential. All the plotted quantities are dimensionless.

### 5.2.1 Temperature effects

Since experiments are performed with fixed temperature, as opposed to fixed energy, we average the finite energy calculations using the normalized Boltzmann distribution for three particles, that is

$$\langle \alpha_{\text{rec}}(a) \rangle_T = \frac{1}{2(k_B T)^3} \int E^2 e^{-E/k_B T} \alpha_{\text{rec}}(a, E) dE, \quad (5.6)$$

where the factor  $E^2$  arises due to the phase-space for three particles. The effect of temperature has been considered in other works such as [D’Incao 2004] and [Braaten 2008]. The integration can readily be achieved with the parametrized expression in eq. (5.3).

When the value of  $|a|$  is increased the barrier location moves to large  $\rho$  while the barrier height is reduced. This means that the high-energy limit

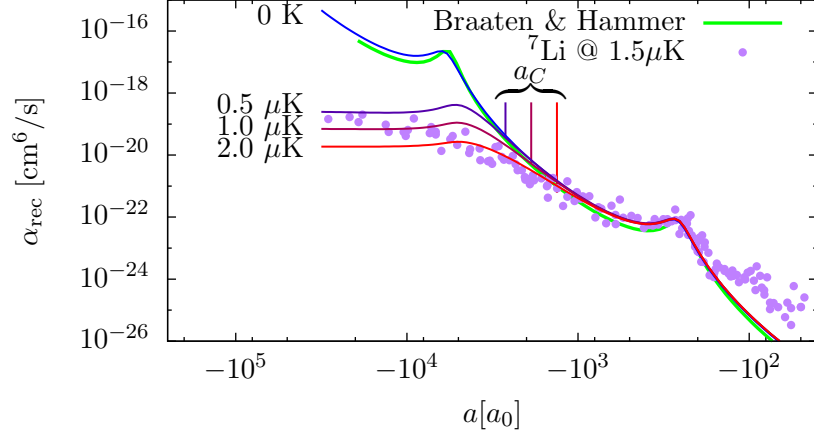


Figure 5.3: The recombination coefficient,  $\alpha_{\text{rec}}$ , at zero and finite temperature for  ${}^7\text{Li}$  with the experimental data at a temperature of  $1.5\mu\text{K}$  [Dyke 2013]. The scattering length,  $a$ , is in units of the Bohr radius,  $a_0$ . The parameter  $a_C$  indicates the critical scattering length where the height of the barrier equals the mean energy of the atoms. At this value the spectrum starts to deviate from the  $a^4$  behaviour, which corresponds quite nicely to the behaviour of the experimental data.

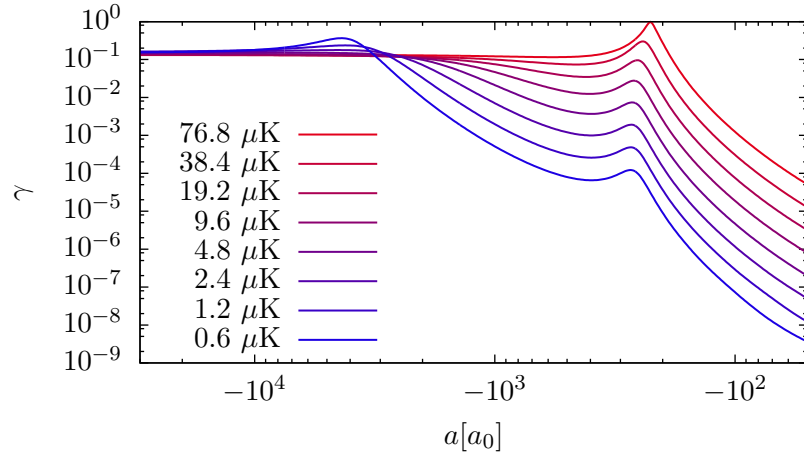


Figure 5.4: The decay parameter  $\gamma$  for the  ${}^7\text{Li}$  system as a function of scattering length,  $a$ , for finite energies in temperature units. At large  $|a|$  all curves have about the same value  $\sim 0.14$ , independent of energy.

is approached and an  $a$ -independent recombination rate is obtained. The energy dependence in this limit is  $1/E^2$  and the value of  $K$  determines the limiting value of  $\alpha_{\text{rec}}$ . We show in Figure 5.4 the calculated values of  $\gamma$  as a function of  $a$  for several finite energies (displayed in temperature units, however, a temperature averaging of the form eq. (5.6) has not been performed here). For small  $|a|$  all  $\gamma$ -values are lowered when the energy is increased, for large  $|a|$  the energy and scattering length independent constant of about 0.14 is reached. This value depends on the strength of the imaginary potential  $m|V_{\text{imag}}|r_{\text{imag}}^2/\hbar^2$ , which controls the height and shape of the absorption peaks as functions of both  $E$  and  $a$ . This numerical value is deceptively similar to the  $\eta^-$  of [Dyke 2013] used to fit the peak in Figure 5.3. Formally there is also a connection although  $\eta^-$  is more complicated and derived through multiple scattering theory for zero energy [Braaten 2006]. The physical meaning is different from our  $\gamma$  and the expressions are not one-to-one related.

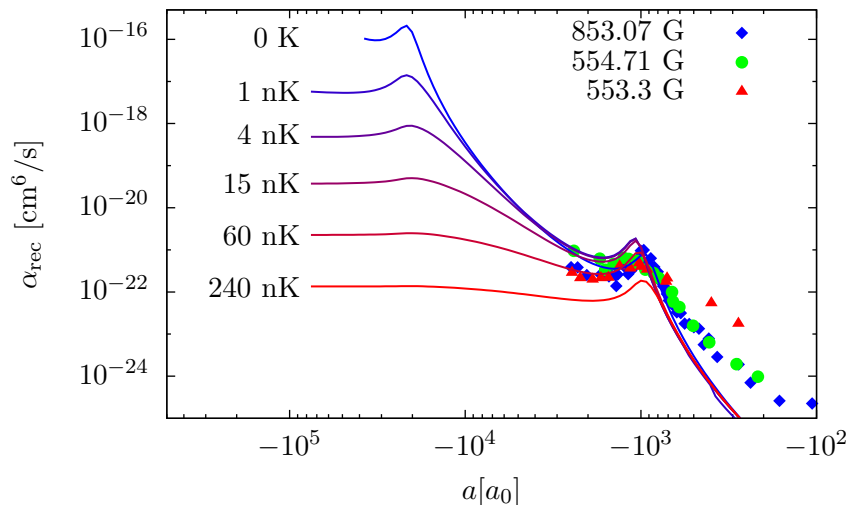


Figure 5.5: The recombination coefficient  $\alpha_{\text{rec}}$  at zero and finite temperatures for  $^{133}\text{Cs}$  with the experimental data taken at a temperature of about 15 nK [Berninger 2011].

### 5.3 Comparison to experimental data

We now compare the available experimental data with numerical calculations from the optical potential model. The numerical results and the parametriza-

tion from eq. (5.3) are virtually indistinguishable. The experimental recombination data for  ${}^7\text{Li}$  [Dyke 2013] along with the calculations from our model at zero and finite temperatures are shown in Figure 5.3. The only pronounced measured peak at  $a \approx -280a_0$  (where  $a_0$  is the Bohr radius) is well described by our model. The peak position is fitted with  $r_{\text{imag}} = 0.41a_0$  and the overall shape of the peak is fitted with  $V_{\text{imag}} = -68\hbar^2/ma_0^2$ . For zero temperature we find, for all  $a$ , almost precisely the same as the zero-energy formula of Ref. [Braaten 2006] where  $\eta^- = 0.12$  and  $a^{(-)} = -241a_0$  [Dyke 2013]. At finite temperatures, we find the observed lowering of recombination rates for large negative  $a$ . This flattening of  $\alpha_{\text{rec}}$  appears for temperatures exceeding the barrier height, in other words for  $a^2 > a_C^2 \equiv 0.143\hbar^2 a_0^2 / (mTk_B)$  as shown in Figure 5.3 for the indicated temperatures.

Recombination rates are also measured for  ${}^{133}\text{Cs}$  at  $T \sim 15$  nK for three different Feshbach resonances [Berninger 2011] which show very similar behaviour. These are shown in Figure 5.5 along with our calculations for different temperatures using  $r_{\text{imag}} = 1.58a_0$  and  $V_{\text{imag}} = -10\hbar^2/ma_0^2$ . Our model reproduces the data for all three resonances with the same model parameters. No data exists at  $a \sim -2 \times 10^4 a_0$  where we predict another peak. From Figure 5.5 we conclude that a temperature below  $\sim 2$  nK seems to be required to observe this peak clearly.

## 5.4 Conclusions

We present a simple and physically transparent model of three-body recombination for negative scattering lengths that does not require a short-range three-body cut-off. Instead it includes an imaginary potential at short distance that takes decay into deeply bound dimers into account. Full numerical solutions of the three-body equations were used to obtain the recombination rate and subsequently a parametrization in terms of the Breit-Wigner resonance formula was presented and shown to display the expected scaling behaviour. Finally, it was shown how this new model reproduces the experimental data on  ${}^7\text{Li}$  and  ${}^{133}\text{Cs}$ . If we express the radius of the imaginary potential in units of the van der Waals length we find  $r_{\text{imag}}/r_{\text{vdW}} = 0.0063$  and  $r_{\text{imag}}/r_{\text{vdW}} = 0.0078$  respectively, while the strength is  $|V_{\text{imag}}|/V_{\text{vdW}} = 2.87 \cdot 10^5$  and  $|V_{\text{imag}}|/V_{\text{vdW}} = 4.08 \cdot 10^5$  where  $V_{\text{vdW}} = \hbar^2/mr_{\text{vdW}}^2$ . The similarity of  $r_{\text{imag}}$  and  $V_{\text{imag}}$  in van der Waals units indicates that there could be universality hidden in these parameter. The differences that we find is most likely related to the difference in deeply bound states of the two-body potentials of  ${}^7\text{Li}$  and  ${}^{133}\text{Cs}$ .

## Chapter 6

# Mass-imbalanced systems

*This chapter considers recombination in systems of mixed species of atoms for negative scattering lengths. The eigenvalue equation is generalized to non-equal mass systems and the method of optical potentials is applied.*

---

Systems of mixed species atoms like K-Rb [Klempt 2007] and Cs-Li [Repp 2013] have gotten quite a bit on interest lately as they provide yet another window into the realm of few-body physics. Furthermore, they possess some quite interesting features worthy of investigation. Most notably, the Efimov scaling effect persists in these systems, however, the scaling parameter is reduced from the value 22.7 for the three equal mass case. We show in the case of the Cs-Li system that the scale factor is only 4.85, practically doubling the frequency of peaks in the recombination coefficient as a function of the scattering length,  $a$ . Being able to observe more than a single resonance peak is essential to efficiently study the effects of the effective range as discussed hitherto. Results in this chapter are, as of this writing, still in the initial investigation phase.

### 6.1 The mass-imbalanced eigenvalue equation

The derivation of eq. (2.55) relied on the assumption that all three particles were identical, with the implication that the rotation angle from eq. (2.51) was equal to  $\frac{\pi}{3}$ . Here we relax that assumption and instead assume that the system consists of two kinds of particles, one light particle and two heavy particles as shown in Figure 6.1. For this system of particles the Jacobi-coordinates are still given by eq. (2.34) but with, say,  $m_2 = m_3$ . The arbitrary scaling mass,  $m$ , is chosen to be the mass of the lighter of the atoms, that is  $m = m_1$ .

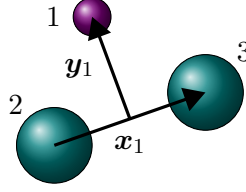


Figure 6.1: The system of one light (small sphere) and two heavy (large spheres) atoms along with the Jacobi coordinates  $\mathbf{x}_1$  and  $\mathbf{y}_1$ .

The generalization of eq. (2.55) to mass-imbalanced systems is given by setting the determinant of the matrix  $M$  equal to zero where the elements of  $M$  are given by [Fedorov 2001b]

$$M_{ii} = \nu \cos\left(\frac{\nu\pi}{2}\right) + \frac{\rho}{\sqrt{\mu_i}a_i} \sin\left(\frac{\nu\pi}{2}\right), \quad (6.1a)$$

$$M_{ij} = \frac{2 \sin\left[\nu\left(\phi_{ij} - \frac{\pi}{2}\right)\right]}{\sin(2\phi_{ij})}, \quad i \neq j, \quad (6.1b)$$

where  $\phi_{ij}$  is given by eq. (2.51) and  $a_i$  is the scattering length between particles  $j$  and  $k$ . The radial equation remains unchanged. We will treat specifically the mixed system of one  ${}^6\text{Li}$  atom and two  ${}^{133}\text{Cs}$  atoms. This implies  $a_2 = a_3$  following Figure 6.1. In this case the matrix  $M$  reduces to a  $2 \times 2$ -matrix. Furthermore, near the Feshbach resonance of the Cs-Li system at  $\sim 850$  G [Repp 2013] the interaction between the Cs atoms is comparatively negligible and we set  $a_1 = 0$  for simplicity and the resulting eigenvalue equation becomes

$$\frac{\nu \cos\left(\frac{\nu\pi}{2}\right)}{\sin\left(\frac{\nu\pi}{2}\right)} + \frac{2 \sin\left[\nu\left(\phi - \frac{\pi}{2}\right)\right]}{\sin(2\phi) \sin\left(\frac{\nu\pi}{2}\right)} = \frac{\rho}{\sqrt{\mu}a}, \quad (6.2)$$

where now  $a = a_2$  is the scattering length between the sub-system of one light and one heavy atom,  $\mu = \frac{1}{m_1} \frac{m_1 m_2}{m_1 + m_2}$  is the reduced mass of this subsystem and  $\phi = \phi_{12}$  from eq. (2.51).

### 6.1.1 Properties of the mass-imbalanced potentials

To investigate the effect of changing the masses we look at the location of the zero-crossing of the radial potential  $\frac{\nu_1^2 - 1/4}{\rho^2}$ ; the location and height of the potential; the tail-behaviour of the potential and of course the geometric scaling factor. We only consider negative scattering lengths in this chapter. For positive scattering lengths there is, of course, no barrier.

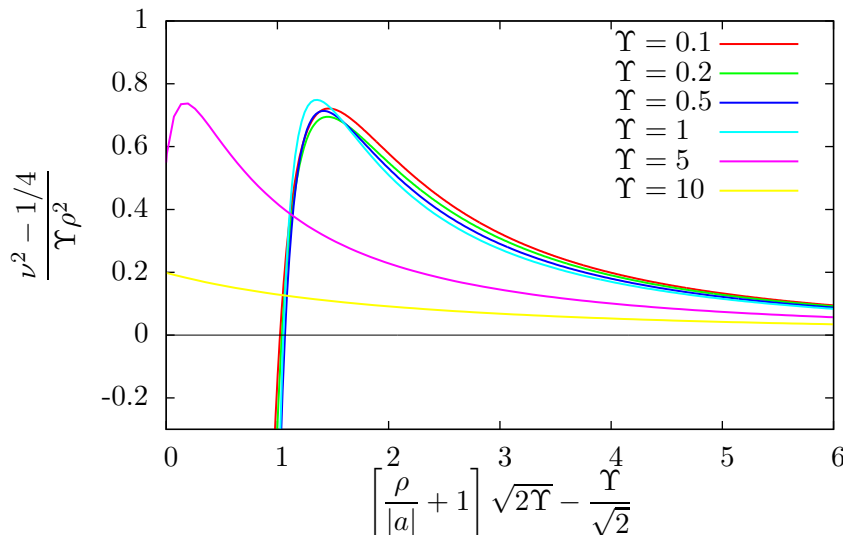


Figure 6.2: The hyper-radial adiabatic potentials for several mass ratios,  $\Upsilon = m_1/m_2$ . The somewhat unusual scaling of the abscissa comes from eq. (6.4) and ensures that the zero-crossing of the potentials are independent of mass ratios for  $\Upsilon \leq 1$ . However, the denominator  $\sqrt{2}$  in the final term does not come from eq. (6.4) but is included as it provides a better overall independence of  $\Upsilon$  all the way up to 1. For  $\Upsilon > 1$  the scaling is clearly not good, nor should it be expected to be so. Notice also how the height of the potentials scale quite well with  $\Upsilon$ .

The zero-crossing,  $\rho_0$  for which  $V(\rho_0) = 0$ , of the potential can be found by inserting  $\nu = \frac{1}{2}$  into eq. (6.2) with the result

$$\frac{\rho_0}{\sqrt{\mu}a} = \frac{1}{2} + \frac{2\sqrt{2}}{\sin(2\phi)} \sin\left(\frac{\phi}{2} - \frac{\pi}{4}\right). \quad (6.3)$$

We define the ratio of masses to be  $\Upsilon = m_1/m_2$ . In the limit  $\Upsilon \ll 1$ , i.e. the mass of the light atom much smaller than the masses of the two heavy atoms, the location of the zero-crossing is given approximately as

$$\frac{\rho_0}{|a|} \approx \frac{1}{\sqrt{2\Upsilon}} - 1 + \sqrt{\frac{\Upsilon}{2}}, \quad (6.4)$$

where  $\mu = 1/(1 + \Upsilon)$  has been used. In Figure 6.2 the adiabatic potentials are plotted for several different mass ratios. The abscissa has been transformed according to eq. (6.4) in such a way that all potentials with small  $\Upsilon$  cross zero at an  $x$ -value of about 1. The expression 6.4 is accurate for  $\Upsilon$  values up

to unity. It must be noted, however, that the mass ratio of 1 in this context does not correspond to a system of three identical particles as described in the previous chapters, since the interaction between two of the particles has been specifically put to zero in this chapter.

The corresponding limit for large  $\Upsilon$  is

$$\frac{\rho_0}{|a|} = \frac{\sqrt{2}-1}{2\sqrt{\Upsilon}} \left( 1 - \frac{1}{\sqrt{2\Upsilon}} \right), \quad (6.5)$$

but we do not consider these systems presently. One reason why these systems are not as attractive is the fact that the Efimov scaling factor actually increases, making it even more difficult to observe more than a single recombination peak.

As seen in Figure 6.2, transforming the hyper-radial coordinate,  $\rho$ , according to eq. (6.4) and simultaneously scaling the height of the potential with the mass ratio  $\Upsilon$  yields an almost mass-independent curve for  $\Upsilon \leq 1$ . This enables us to make some general observations with regards to how the recombination coefficient must behave when the mass ratio is changed.

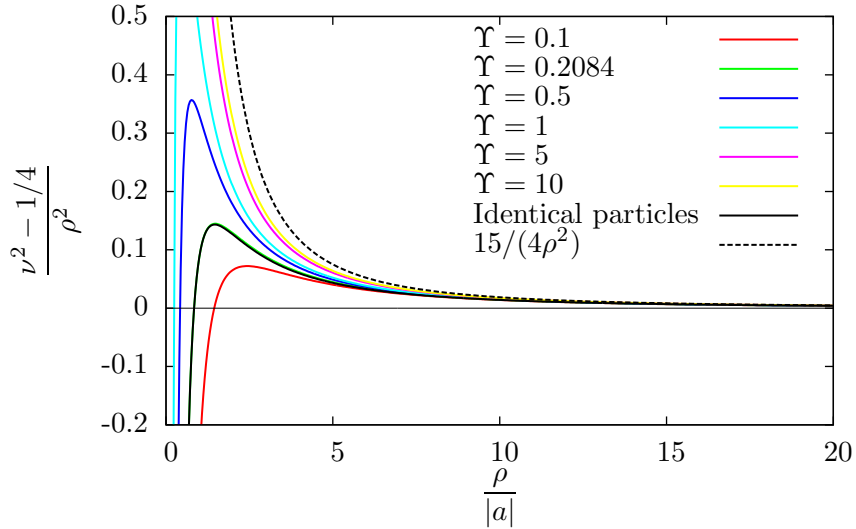


Figure 6.3: The tail of the adiabatic potentials. Notice how all tails have the same asymptotic behaviour  $V(\rho) = \frac{15}{4\rho^2}$ . The curve for identical particles including the interaction between particles 2 and 3 in Figure 6.1, apparently corresponds quite well to the mass ratio  $\Upsilon = 0.2084$  in a system where the heavy particles do not interact.

Figure 6.3 shows the tail behaviour of the adiabatic potentials. We find that the long-range tail still has the form  $V(\rho) = \frac{15}{4\rho^2}$ . Corrections due to the mass ratio show up only in terms of order  $1/\rho^3$  and higher. This means that for instance the probability for tunnelling through the barrier in Figure 6.2 still goes as  $E^2$  for small energies.

The last step in our initial analysis of the mass-scaling properties of the system in Figure 6.1, is to find the Efimov scaling factor, which is found by solving eq. (6.2) for  $\rho/a = 0$  with  $\nu = is_0$  where  $s_0$  is real

$$\cosh\left(\frac{\pi s_0}{2}\right) s_0 \sin(2\phi) = 2 \sinh\left[s_0\left(\frac{\pi}{2} - \phi\right)\right]. \quad (6.6)$$

The scale factor between consecutive minima then is  $F = e^{\pi/s_0}$  as stated in section 2.2.3. In the case of the Cs-Li system this yields  $F = 4.85$ . For systems of three identical particles the factor is  $F = 22.7$ , however, this value is not obtained from eq. (6.6) as this equation assumes no interaction between the two heavy particles. If all three particles are assumed to interact, the first 2 in the right hand side should be a 4 instead. Since  $4.85^2 = 23.5 \sim 22.7$  there should be about twice as many resonance peaks in the recombination coefficient for a given scattering length range for the mixed Cs-Li system compared to a system of identical particles.

## 6.2 Results

The overall  $a^4$  scaling can easily be attributed, using a WKB calculation, to the inner turning point given by eq. (6.3). This is seen by the following: assume for simplicity that the potential has the form  $V(\rho) = \nu_1^2/\rho^2$  for  $\rho_0 \leq \rho < \infty$  (the Langer correction has been included) with  $\nu_1 = 2$ . This simple form is quite reasonable as the potentials, as seen in Figure 6.2, drop quite rapidly once the potential has reached its maximum value. The probability of tunnelling through this barrier can be estimated using eq. (2.84). In the limit of  $E \rightarrow 0$  the integral takes the form (with  $m = \hbar = 1$ )

$$\gamma = \int_{\rho_0}^{\rho_t} \sqrt{\frac{\nu_1^2}{\rho^2}} d\rho = \nu_1 \ln\left(\frac{\rho_t}{\rho_0}\right), \quad (6.7)$$

where the outer classical turning point is  $\rho_t = \nu_1/\sqrt{2E}$ . The tunnelling probability then reads

$$P = \exp(-2\gamma) = \left(\frac{\rho_0}{\rho_t}\right)^2 \propto E^2 \rho_0^4. \quad (6.8)$$

Since  $\rho_0$  is proportional to the scattering length,  $a$ , this establishes the  $a^4$  relation. This also shows that the  $a^4$  dependency does not change for the mass-imbalanced systems. Moreover, the overall rate of recombination is expected to increase for smaller mass ratios,  $\Upsilon$ . For instance, for  $\Upsilon = 0.1$ , eq. (6.4) yields  $\rho_0 \approx 1.46|a|$  and  $1.46^4 = 4.5$ , i.e a 4.5-fold increase in the rate of recombination for any given scattering length.

This is, of course, a very simple analysis and more factors have to be taken into account to obtain accurate results. For instance, the numerical factor in eq. (5.2) might not be valid for the mass-imbalanced systems. This is yet to be determined.

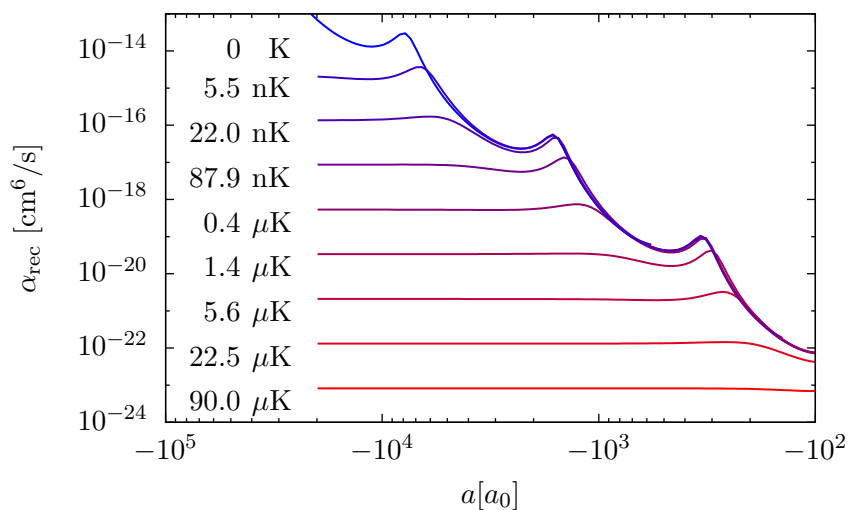


Figure 6.4: The recombination coefficient,  $\alpha_{\text{rec}}$ , in a system of  $^{133}\text{Cs}$  and  $^6\text{Li}$  for negative scattering lengths,  $a$ , using eq. (5.2) and eq. (5.6) at zero and finite temperatures.

Figure 6.4 shows an exploratory calculation of the recombination coefficient for the Cs-Li system using the optical potential model from the previous chapter as well as the energy averaging from eq. (5.6) for several finite temperatures. The values of the depth,  $V_{\text{imag}}$ , and width,  $r_{\text{imag}}$ , of the imaginary potential have been reused from Figure 5.3.

### 6.3 Conclusions

In this chapter we investigated the recombination coefficient for mass-imbalanced systems. The hyper-radial adiabatic potential was generalized to systems with

two heavy, non-interacting atoms and one light atom. Simple properties of these potentials led us to the prediction that the overall magnitude of the rate of recombination should increase for decreasing mass ratios  $\Upsilon = m_1/m_2$ . Of greater interest is the fact that the Efimov scaling factor is reduced down from 22.7 to a mere 4.85 in the case of the Cs-Li system. This makes the effective range dependency on the scale factor a lot easier to verify experimentally as more resonance peaks can be seen in a given range of scattering lengths as compared to systems of three identical particles.

Additional study is required in this field, especially since experimental work is progressing strongly in this direction in these years.



## Chapter 7

# Summary and Outlook

---

This thesis has investigated effective range effects in three-body recombination, bound state spectra and the three-body parameter. The effective range is a correction to the well-known scattering length approximation that is often used in cold gas physics. In this thesis the effective range was implemented using a two-channel model with zero-range interactions. This model was built on the physics of Feshbach resonances and among other things described the relation between the scattering length,  $a$ , and applied magnetic field strength,  $B$ . The effective range of a system of interacting particles is inversely proportional to the width of the Feshbach resonance that is used to tune the interaction strength in the system. For broad resonances the effective range is rather small with corresponding small modifications to the universal single-channel zero-range predictions. Feshbach resonances with narrow widths are therefore required to be studied in order to accurately confirm (or refute) the predictions of the effective range models in this thesis.

The effective range takes into account the physical range of the interaction instead of merely approximating it with a zero-range potential. Investigating such effects will become more important in the coming years as more and more experimental data with ever increasing accuracy will become available. Thus deviations from the universal zero-range theories are expected to become observable.

Specifically, as we found in chapter 3, the two models that include the effective range, namely the two-channel model and the effective range expansion model, predict that for the recombination coefficient  $\alpha_{\text{rec}}$  for positive scatter-

ing lengths the ratio of scattering length values of consecutive minima is less than the universal value which equals 22.7 for identical particles. We found the origin of this effect to be a change in the atom-dimer threshold when the effective range was included. The threshold obtains effective range corrections that modify the values of the scattering length,  $a^*$ , where the trimer and dimer energies coincide.

The method applied to calculate the recombination coefficient, namely the hidden crossing method, has, to our knowledge, not been compared to the experimental data before. Our comparison with available experimental data proved that the method is quite good at providing reasonably accurate predictions, in spite of the simplicity. Unfortunately the available data is for systems of wide resonances and correspondingly short effective ranges, wherefore the effects of the effective range are too small to see. More data for narrow Feshbach resonance systems are required.

Chapter 4 was dedicated to the three-body parameter  $a^{(-)}$ . For zero-range interactions an additional length scale is required to prevent the system from becoming infinitely bound. This length scale is known as the three-body parameter and has been thought to depend on short-range details of the physical potential. Quite surprisingly a universal relation between the three-body parameter,  $a^{(-)}$ , and the two-body van der Waals length,  $r_{\text{vdW}}$ , appears to exist across several different atomic species. This relation was investigated using the single-channel zero-range model and our two-channel model to include the effective range. We found that the available experimental data is modelled well by our calculations. We also found that for large effective ranges the ratio  $a^{(-)}/r_{\text{vdW}}$  is expected to be lower than the universal value of  $\sim 9.8$ . Again more study in narrow resonance systems is required to confirm this prediction.

In chapter 5 we investigated the recombination coefficient for negative scattering lengths,  $a$ . The hidden crossing method does not work for  $a < 0$  since weakly bound dimers do not exist for negative  $a$ . Instead we employed an optical potential model where the adiabatic potential, which is used in the radial differential equation, gets a complex value  $V_{\text{imag}}$  for small  $\rho < r_{\text{imag}}$ . This trick effectively emulates recombination into deep dimers and provides a quite accurate reproduction of the experimental data. The model furthermore included finite temperature effects which we showed did also correspond nicely to trends in the experimental data. To be able to see a second peak in the data for  ${}^7\text{Li}$  we predict that a temperature in the sub  $\mu\text{K}$  regime is required.

The basic parameters of our optical model were the imaginary potential

strength,  $V_{\text{imag}}$ , and range,  $r_{\text{imag}}$ . The parameters obtained from fitting to the data revealed the quite surprising results  $r_{\text{imag}}/r_{\text{vdW}} = 0.0063$  for  ${}^7\text{Li}$  and  $r_{\text{imag}}/r_{\text{vdW}} = 0.0078$  for  ${}^{133}\text{Cs}$ , the similarity in these numbers could indicate some universal feature in the recombination process. Likewise for the strengths we obtained  $|V_{\text{imag}}|/V_{\text{vdW}} = 2.87 \cdot 10^5$  for  ${}^7\text{Li}$  and  $|V_{\text{imag}}|/V_{\text{vdW}} = 4.08 \cdot 10^5$  for  ${}^{133}\text{Cs}$ , where  $V_{\text{vdW}} = \hbar^2/mr_{\text{vdW}}^2$ .

This chapter did not include effective range effects but it is reasonable to assume that the conclusions from chapter 3 still hold true.

Finally, chapter 6 treated our most recent results obtained for a system of non-identical particles. Specifically, systems of one light atom and two heavy atoms, where the interaction between the heavy atoms is negligible compared to the light-heavy interaction, as is the case for  ${}^6\text{Li}$  and  ${}^{133}\text{Cs}$ , was treated. There are no experimental data for recombination in such systems yet, but many groups are reporting observations of Feshbach resonances in several mixed atom systems [Klempt 2007, Repp 2013]. It is therefore only a matter of time before the first experimental evidence of recombination is obtained. We show that the most interesting feature in these systems is that the geometric scaling factor, which equals 22.7 for identical particle systems, is greatly reduced. For the Cs-Li system the factor is only 4.85, which would allow twice as many trimer states in a given range of scattering lengths as compared to systems of identical particles. Thus more peaks/troughs in the recombination coefficient, are expected to be present in a given range of scattering lengths. This is a great boon as the scaling factor 22.7 is far too large to experimentally observe enough resonances within currently attainable scattering length ranges.

The future clearly lies with the mass-imbalanced systems. The basics outlined in chapter 6 provide a stepping stone for future works in this field. Combining the outlined method of optical potentials with the two-channel and effective range expansion models should be relatively straight forward such that the effective range effects can be probed in the mixed species systems. Another thing to take properly into account is the interactions between the heavy atoms, which has been explicitly neglected for simplicity in the initial calculations.



## Appendix A

# Efficiently solving the eigenvalue equations

The eigenvalue equations eq. (2.55), eq. (2.71) and eq. (2.77) yield two equations in two unknowns when treating the eigenvalue as a complex quantity,  $\nu = \nu_{\text{re}} + i\nu_{\text{im}}$ . The equations need to be solved for  $\rho$ -values ranging from very large down to zero and even for complex values when using the hidden crossing method of section 2.3.1.

### Quadratic extrapolation

Efficiently solving these equations require good initial guesses for the solver routine. Solving for  $\nu(\rho)$  should always start at large  $\rho$  and work towards smaller  $\rho$  since the asymptotic expressions eq. (2.57) and eq. (2.59) are very accurate at large  $\rho$ . Once a few points have been found, say  $\nu_1, \nu_2$  and  $\nu_3$  at  $\rho_1, \rho_2$  and  $\rho_3$ , respectively, a quadratic extrapolation scheme can be used to guess the value of  $\nu_4$ .

Assume the following quadratic form

$$\nu_{\text{quad}}^2(\rho) = a\rho^2 + b\rho + c. \quad (\text{A.1})$$

Since  $\nu^2$  is a real value (except when also  $\rho$  is complex) it is better to extrapolate the square of  $\nu$  than  $\nu$  itself. This is straightforward to solve for  $a, b$  and  $c$  in terms of  $\nu_1, \nu_2$  and  $\nu_3$  and hence to obtain  $\nu_4$ . This method yields a much better initial guess for the next step than simply using the previous value ( $\nu_3$  in this case) and lowers the number of iterations required by a factor of  $\sim 1.5$  with an overall speed increase of  $\sim 25\%$ . Another benefit is that the change in  $\nu$  from purely real to purely imaginary, i.e.  $\lambda(\rho)$  changes from positive to

negative or vice versa (only possible when  $a < 0$ ) is handled gracefully by the numerical solver.

In the case of fixed step size, the quadratic extrapolation simply yields

$$\nu_4^2 = \nu_1^2 + 3(\nu_3^2 - \nu_2^2), \quad (\text{A.2})$$

which is easily calculated at a low extra cost in computation.

### Adaptive step size

To further speed up the calculation an adaptive step size can be implemented. In case of the effective range expansion and two-channel models, the eigenvalue solutions show a sharp curvature feature when  $\rho \lesssim |R|$  as seen in Figure 3.1. To resolve this region without manually having to specify an appropriate density of points an adaptive step size controller is used.

The local error estimate is taken to be the absolute of the difference between the actual solution  $\nu(\rho)$  and the guess provided by eq. (A.1). Note that errors will not accumulate, the solution is as good at any one point than it is at any other since the guess is only used as an initial value.

Given the local error,  $\epsilon = |\nu_i - \nu_{i,\text{guess}}|$ , and tolerance,  $\tau$ , (typically  $10^{-4}$  give good results) the size of the next step,  $h_{\text{new}}$ , given the current step size,  $h_{\text{old}}$ , is

$$h_{\text{new}} = \begin{cases} \min [2h_{\text{old}}, h_{\text{max}}] & \epsilon < \tau \\ \max \left[ 0.95h_{\text{old}} \left( \frac{\tau}{\epsilon} \right)^{1/4}, h_{\text{min}} \right] & \epsilon > \tau \end{cases} \quad (\text{A.3})$$

where  $h_{\text{min}}$  and  $h_{\text{max}}$  are chosen to avoid inappropriately large or small step sizes.

The greatest benefit of these method is not so much an increase in speed but instead an increase in the number of points where the solution varies rapidly, resulting in smoother curves to be used for further numerical work.

## Appendix B

# Low-energy limit of recombination probability

In section 5.2 we took the limit  $k \rightarrow 0$  to obtain the recombination rate at zero energy using numerical calculations for finite energies. This limit was of the form

$$\alpha_{\text{rec}} \propto \lim_{k \rightarrow 0} \frac{1 - e^{-4\gamma}}{k^4} . \quad (\text{B.1})$$

For this limit to be finite we must have  $1 - e^{-4\gamma} \propto k^4$ , or equivalently  $\gamma \propto k^4$ , for small  $k$ . In this appendix it is proven that this limit exists by considering a simpler version of the potential with the same qualitative properties.

The adiabatic potential in the  $n = 1$  channel is  $V(\rho) = \frac{15}{4\rho^2}$  for large  $\rho$  since  $\nu \rightarrow 2$  in this limit, according to eq. (2.59). Consider the potential

$$V(\rho) = \begin{cases} V_0 & \text{for } \rho < r_0 \\ \frac{\nu^2 - 1/4}{2\rho^2} & \text{for } \rho > r_0 \end{cases} , \quad (\text{B.2})$$

where  $\nu = 2$  in the present problem and  $V_0$  is a complex constant. The units are  $\hbar = m = 1$ . This is a simplified version of Figure 5.1 where the  $1/\rho^2$  behaviour has been extended down to  $r_0$  (which plays the role of  $r_{\text{imag}}$  in the figure). For  $\rho < r_0$  the solution with the boundary condition  $f(0) = 0$  is

$$f_{<}(\rho) = \sin(\kappa\rho) , \quad \kappa = \sqrt{2(E - V_0)} . \quad (\text{B.3})$$

For  $\rho > r_0$  the general solution is ([Abramowitz 1972] 9.1.49)

$$f_{>}(\rho) = \sqrt{\rho} \left( AH_{\nu}^{(2)}(k\rho) + BH_{\nu}^{(1)}(k\rho) \right) , \quad (\text{B.4})$$

where  $H_\nu^{(1)}$  and  $H_\nu^{(2)}$  are Hankel functions of the first and second kind and  $k = \sqrt{2E}$ . In the limit of large  $\rho$ ,  $\sqrt{\rho}H_\nu^{(1)}$  behaves like an outgoing wave  $\propto e^{ik\rho}$  while  $\sqrt{\rho}H_\nu^{(2)}$  behaves like an incoming wave  $\propto e^{-ik\rho}$ .

In the limit of small  $z$  the Hankel functions behave like

$$H_\nu^{(1,2)}(z) \approx \frac{1}{\Gamma(\nu+1)} \left(\frac{z}{2}\right)^\nu \pm \frac{\Gamma(\nu)}{\pi i} \left(\frac{2}{z}\right)^\nu. \quad (\text{B.5})$$

To stitch together the solutions from eq. (B.3) and eq. (B.4) at the boundary  $\rho = r_0$  we need the derivative of the Hankel functions (from [Abramowitz 1972] 9.1.30)

$$\frac{d\mathcal{H}_\nu(z)}{dz} = \mathcal{H}_{\nu-1}(z) - \frac{\nu}{z}\mathcal{H}_\nu(z), \quad (\text{B.6})$$

where  $\mathcal{H}$  is any of the Hankel functions (incidentally the expression is valid for Bessel and Neumann functions as well).

By the requirements that the wave function and its derivative must be continuous at the boundary  $\rho = r_0$  we get the coefficients  $A$  and  $B$  as

$$A = -\sqrt{r_0} \left[ H_\nu^{(1)}(f_0 - 2f'r_0) + f_0 \left( H_{\nu-1}^{(1)} - H_{\nu+1}^{(1)} \right) r_0 k \right] D^{-1}, \quad (\text{B.7})$$

$$B = \sqrt{r_0} \left[ H_\nu^{(2)}(f_0 - 2f'r_0) + f_0 \left( H_{\nu-1}^{(2)} - H_{\nu+1}^{(2)} \right) r_0 k \right] D^{-1}, \quad (\text{B.8})$$

with

$$D = \left[ H_\nu^{(1)} \left( H_{\nu-1}^{(2)} - H_{\nu+1}^{(2)} \right) + \left( H_{\nu+1}^{(1)} - H_{\nu-1}^{(1)} \right) H_\nu^{(2)} \right] k, \quad (\text{B.9})$$

where  $f_0 = f_<(r_0)$  and  $f'_0 = \left. \frac{df_<}{d\rho} \right|_{r_0}$ . The denominator  $D$  is not really needed to obtain the ratio of  $B$  to  $A$  but included nevertheless for the sake of completeness.

All this was for a general  $\nu$ . Now we use the specific value  $\nu = 2$  appropriate for our problem. With eq. (B.5) to get the low-energy limit the probability of recombination is

$$1 - e^{-4\gamma} = 1 - \left| \frac{B}{A} \right|^2 = 2\pi(r_0k)^4 \text{Im} \left( \frac{5f_0 - 2f'_0r_0}{48f_0 + 32f'_0r_0} \right). \quad (\text{B.10})$$

At low energy the probability for recombination is proportional to  $k^4$  and the limit (B.1) can be safely taken. It is the asymptotic form of the potential  $V(\rho) = 15/4\rho^2$  that gives this result, and the conclusion is therefore also valid for the actual adiabatic potential, not just for the toy model in eq. (B.2).

Incidentally the power of 4 is due to  $\nu = 2$ , the general form is  $\alpha_{\text{rec}} \propto k^{2\nu}$ . We note also from eq. (B.10) that only if the ratio  $f'_0/f_0$  is complex will the

probability be non-zero. This can only happen if the parameter  $V_0$  is itself complex.

Slightly less obvious is that for the probability for recombination to be positive we need the imaginary part of  $V_0$  to be negative. This can most easily be seen by plotting the expression eq. (B.10) as function of the imaginary depth. A positive value of the imaginary part of  $V_0$  would yield a negative probability, which in this case should be interpreted as particles being created at short distance, i.e. the reverse process of what we want to study. Therefore, we let  $V_0$  have a negative imaginary part.



# Bibliography

- [Abramowitz 1972] M. Abramowitz and I. A. Stegun. Handbook of mathematical functions. Dover Publications, 1972.
- [Berninger 2011] M. Berninger, A. Zenesini, B. Huang, W. Harm, H.-C. Nägerl, F. Ferlaino, R. Grimm, P. S. Julienne and J. M. Hutson. *Universality of the Three-Body Parameter for Efimov States in Ultracold Cesium*. Phys. Rev. Lett., vol. 107, [page 120401](#), Sep 2011.
- [Braaten 2001] E. Braaten and H.-W. Hammer. *Three-Body Recombination into Deep Bound States in a Bose Gas with Large Scattering Length*. Phys. Rev. Lett., vol. 87, [page 160407](#), Oct 2001.
- [Braaten 2006] E. Braaten and H.-W. Hammer. *Universality in few-body systems with large scattering length*. Physics Reports, vol. 428, no. 5–6, [pages 259 – 390](#), 2006.
- [Braaten 2008] E. Braaten, H.-W. Hammer, D. Kang and L. Platter. *Three-body recombination of identical bosons with a large positive scattering length at nonzero temperature*. Phys. Rev. A, vol. 78, [page 043605](#), Oct 2008.
- [Bruun 2005] G. M. Bruun, A. D. Jackson and E. E. Kolomeitsev. *Multichannel scattering and Feshbach resonances: Effective theory, phenomenology, and many-body effects*. Phys. Rev. A, vol. 71, [page 052713](#), May 2005.
- [Chin 2010] C. Chin, R. Grimm, P. S. Julienne and E. Tiesinga. *Feshbach resonances in ultracold gases*. Rev. Mod. Phys., vol. 82, [pages 1225–1286](#), April 2010.
- [Chin 2011] C. Chin. *Universal scaling of Efimov resonance positions in cold atom systems*. [arXiv:1111.1484v2](#), Nov 2011.

- [D’Incao 2004] J. P. D’Incao, H. Suno and B. D. Esry. *Limits on Universality in Ultracold Three-Boson Recombination*. Phys. Rev. Lett., vol. 93, **page 123201**, Sep 2004.
- [Dyke 2013] P. Dyke, S. E. Pollack and R. G. Hulet. *Finite range corrections near a Feshbach resonance and their role in the Efimov effect*. [arXiv:1302.0281](https://arxiv.org/abs/1302.0281), Feb 2013.
- [Efimov 1971] V. N. Efimov. *Measurements of Tan’s Contact in an Atomic Bose-Einstein Condensate*. Sov. J. Nucl. Phys., vol. 12, pages **589–595**, Nov 1971.
- [Esry 1999] B. D. Esry, C. H. Greene and J. P. Burke. *Recombination of Three Atoms in the Ultracold Limit*. Phys. Rev. Lett., vol. 83, **pages 1751–1754**, Aug 1999.
- [Fedorov 2001a] D. V. Fedorov and A. S. Jensen. *Correlation-induced collapse of many-body systems with zero-range potentials*. Phys. Rev. A, vol. 63, **page 063608**, May 2001.
- [Fedorov 2001b] D. V. Fedorov and A. S. Jensen. *Regularization of a three-body problem with zero-range potentials*. Journal of Physics A: Mathematical and General, vol. 34, no. 30, **page 6003**, 2001.
- [Ferlaino 2010] F. Ferlaino and R. Grimm. *Forty years of Efimov physics: How a bizarre prediction turned into a hot topic*. Physics, vol. 3, **page 9**, Jan 2010.
- [Gogolin 2008] A. O. Gogolin, C. Mora and R. Egger. *Analytical Solution of the Bosonic Three-Body Problem*. Phys. Rev. Lett., vol. 100, **page 140404**, Apr 2008.
- [Gribakin 1993] G. F. Gribakin and V. V. Flambaum. *Calculation of the scattering length in atomic collisions using the semiclassical approximation*. Phys. Rev. A, vol. 48, **pages 546–553**, Jul 1993.
- [Gribakin 1999] G. F. Gribakin, V. V. Flambaum and C. Harabati. *Analytical calculation of cold-atom scattering*. Phys. Rev. A, vol. 59, **pages 1998–2005**, Mar 1999.
- [Griffiths 2005] D. J. Griffiths. Introduction to quantum mechanics, second edition. Pearson Prentice Hall, 2005.

- [Gross 2009] N. Gross, Z. Shotan, S. Kokkelmans and L. Khaykovich. *Observation of Universality in Ultracold  $^7\text{Li}$  Three-Body Recombination*. Phys. Rev. Lett., vol. 103, [page 163202](#), Oct 2009.
- [Gross 2010] N. Gross, Z. Shotan, S. Kokkelmans and L. Khaykovich. *Nuclear-Spin-Independent Short-Range Three-Body Physics in Ultracold Atoms*. Phys. Rev. Lett., vol. 105, [page 103203](#), Sep 2010.
- [Igel-Mann 1986] G. Igel-Mann, U. Wedig, P. Fuentealba and H. Stoll. *Ground-state properties of alkali dimers  $XY$  ( $X, Y = \text{Li to Cs}$ )*. The Journal of Chemical Physics, vol. 84, no. 9, [pages 5007–5012](#), 1986.
- [Jensen 1997] A. S. Jensen, E. Garrido and D. V. Fedorov. *Three-Body Systems with Square-Well Potentials in  $L = 0$  States*. Few-Body Systems, vol. 22, no. 4, [pages 193–237](#), 1997.
- [Jensen 2004] A. S. Jensen, K. Riisager, D. V. Fedorov and E. Garrido. *Structure and reactions of quantum halos*. Rev. Mod. Phys., vol. 76, [pages 215–261](#), Feb 2004.
- [Klempt 2007] C. Klempt, T. Henninger, O. Topic, J. Will, W. Ertmer, E. Tiemann and J. Arlt.  $^{40}\text{K}$ - $^{87}\text{Rb}$  *Feshbach resonances: Modeling the interatomic potential*. Phys. Rev. A, vol. 76, [page 020701](#), Aug 2007.
- [Kraemer 2006] T. Kraemer, M. Mark, P. Waldburger, J. G. Danzl, C. Chin, B. Engeser, A. D. Lange, K. Pilch, A. Jaakkola, H.-C. Nägerl and R. Grimm. *Evidence for Efimov quantum states in an ultracold gas of caesium atoms*. Nature, vol. 440, [pages 315–318](#), 2006.
- [Langer 1937] R. E. Langer. *On the Connection Formulas and the Solutions of the Wave Equation*. Phys. Rev., vol. 51, [pages 669–676](#), Apr 1937.
- [Mahan 1969] G. D. Mahan and M. Lapp. *Bound States of Alkali and Noble-Gas Atoms*. Phys. Rev., vol. 179, [pages 19–27](#), Mar 1969.
- [Naidon 2012a] P. Naidon, S. Endo and M. Ueda. *Physical Origin of the Universal Three-body Parameter in Atomic Efimov Physics*. [arXiv:1208.3912](#), Aug 2012.
- [Naidon 2012b] P. Naidon, E. Hiyama and M. Ueda. *Universality and the three-body parameter of  $^4\text{He}$  trimers*. Phys. Rev. A, vol. 86, [page 012502](#), Jul 2012.

- [Nielsen 1999] E. Nielsen and J. H. Macek. *Low-Energy Recombination of Identical Bosons by Three-Body Collisions*. Phys. Rev. Lett., vol. 83, **pages 1566–1569**, Aug 1999.
- [Nielsen 2001] E. Nielsen, D. V. Fedorov, A. S. Jensen and E. Garrido. *The three-body problem with short-range interactions*. Physics Reports, vol. 347, no. 5, **pages 373 – 459**, 2001.
- [Pethick 2002] C. J. Pethick and H. Smith. *Bose-einstein condensation in dilute gases*. Cambridge, 2002.
- [Pollack 2009] S. E. Pollack, D. Dries and R. G. Hulet. *Universality in Three- and Four-Body Bound States of Ultracold Atoms*. Science, vol. 326, no. 5960, **pages 1683–1685**, 2009.
- [Repp 2013] M. Repp, R. Pires, J. Ulmanis, R. Heck, E. D. Kuhnle, M. Weidemüller and E. Tiemann. *Observation of interspecies  ${}^6\text{Li}$ - ${}^{133}\text{Cs}$  Feshbach resonances*. Phys. Rev. A, vol. 87, **page 010701**, Jan 2013.
- [Sakurai 1994] J. J. Sakurai. *Modern quantum mechanics*, revised edition. Addison-Wesley, 1994.
- [Schmidt 2012] R. Schmidt, S.P. Rath and W. Zwerger. *Efimov physics beyond universality*. The European Physical Journal B, vol. 85, no. 11, **pages 1–6**, 2012.
- [Stenger 1998] J. Stenger, S. Inouye, M. R. Andrews, H.-J. Miesner, D. M. Stamper-Kurn and W. Ketterle. *Observation of Feshbach resonances in a Bose-Einstein condensate*. Nature, vol. 392, **pages 151–154**, Mar 1998.
- [Stenger 1999] J. Stenger, S. Inouye, M. R. Andrews, H.-J. Miesner, D. M. Stamper-Kurn and W. Ketterle. *Strongly Enhanced Inelastic Collisions in a Bose-Einstein Condensate near Feshbach Resonances*. Phys. Rev. Lett., vol. 82, **pages 2422–2425**, Mar 1999.
- [Thøgersen 2008] M. Thøgersen, D. V. Fedorov and A. S. Jensen. *Universal properties of Efimov physics beyond the scattering length approximation*. Phys. Rev. A, vol. 78, **page 020501**, Aug 2008.
- [Thøgersen 2009] M. Thøgersen. *Universality in Ultra-Cold Few- and Many-Boson Systems*. PhD thesis, Aarhus University, 2009.

- [Thomas 1935] L. H. Thomas. *The Interaction Between a Neutron and a Proton and the Structure of  $H^3$* . Phys. Rev., vol. 47, [pages 903–909](#), June 1935.
- [van der Stam 2007] K. M. R. van der Stam, E. D. van Ooijen, R. Meppelink, J. M. Vogels and P. van der Straten. *Large atom number Bose-einstein condensate of sodium*. Rev. Sci. Instrum., vol. 78, [page 013102](#), Jan 2007.
- [Wang 2011] Y. Wang, J. P. D’Incao and B. D. Esry. *Ultracold three-body collisions near narrow Feshbach resonances*. Phys. Rev. A, vol. 83, [page 042710](#), Apr 2011.
- [Wang 2012] J. Wang, J. P. D’Incao, B. D. Esry and C. H. Greene. *Origin of the Three-Body Parameter Universality in Efimov Physics*. Phys. Rev. Lett., vol. 108, [page 263001](#), Jun 2012.
- [Wild 2012] R. J. Wild, P. Makotyn, J. M. Pino, E. A. Cornell and D. S. Jin. *Measurements of Tan’s Contact in an Atomic Bose-Einstein Condensate*. Phys. Rev. Lett., vol. 108, [page 145305](#), Apr 2012.
- [Zaccanti 2009] M. Zaccanti, B. Deissler, C. D’Errico, M. Fattori, M. Jonas-Lasinio, S. Muller, G. Roati, M. Inguscio and G. Modugno. *Observation of an Efimov spectrum in an atomic system*. Nat. Phys., vol. 5, [pages 586–591](#), July 2009.